Effects of X-ray Radiation on Structure and Dynamics of Egg White Protein Gels

DISSERTATION
zur Erlangung des Grades eines Doktors
der Naturwissenschaften

vorgelegt von
M.Sc. Sonja Timmermann

eingereicht bei der Naturwissenschaftlich-Technischen Fakultät
der Universität Siegen
Siegen 2023

Betreuer und erster Gutachter
Prof. Dr. Christian Gutt
Universität Siegen

Zweiter Gutachter
Prof. Dr. Foivos Perakis
Stockholm University

Tag der mündlichen Prüfung
19. Januar 2024

Abstract

The investigation of proteins is highly relevant due to their various functions in living organisms and their importance in nutrition. A technique that can access the collective dynamics of proteins in solution is X-ray photon correlation spectroscopy (XPCS). Using the high coherent fluxes provided by modern X-ray facilities, XPCS can resolve dynamics down to the molecular length scale. However, the proteins' sensitivity to X-ray radiation poses a serious challenge.

This thesis uses XPCS at a synchrotron source to systematically investigate the effects of the X-ray dose and the X-ray dose rate on structure and dynamics of protein gels. The protein gels are hen egg whites cooked at thirteen temperatures between 50 and 85 °C. At these temperatures, the egg white proteins unfold and interconnect, leading to the formation of a gel network at temperatures $\geq 60\,^{\circ}\mathrm{C}$. Among these egg white gel networks, we observe differences in the susceptibility to radiation damage. The gels prepared between 63 °C and 70 °C are more sensitive to radiation effects, and the gel structure is broken up by X-ray doses of 2 kGy to 8 kGy causing an acceleration of the sample dynamics. The egg white gel networks prepared above 73 °C are strengthened by the denaturated ovalbumin, which increases the dose thresholds for structure and dynamics by one order of magnitude.

Like other gels, the cooked egg white gels display ballistic motion where single relaxation events in the network cause directional shifts in the surrounding sites. From the XPCS results, we derive the velocity of this ballistic motion as a function of ten different fluences, revealing a linear dependency of this velocity on the fluence. From this we calculate fluence thresholds above which radiation-induced effects dominate the observed dynamics and find $\Phi^* = (3\pm2)\times10^{-3}\mathrm{phs}^{-1}\,\mathrm{nm}^{-2}$ for the radiation-sensitive gels prepared at $\leq 70\,^{\circ}\mathrm{C}$ and $\Phi^* = (0.9 \pm 0.3)\,\mathrm{ph\,s^{-1}\,nm^{-2}}$ for those prepared above 70 °C. A comparison to other sample systems suggests a connection between the samples' viscoelasticity and their sensitivity to X-ray radiation effects.

This thesis demonstrates how to determine a window of opportunity in terms of dose and dose rate where intrinsic dynamical and structural properties can be measured with XPCS. These insights can be used to evaluate new measurement schemes and make use of the improved coherent flux at the next generation of X-ray facilities, which will perspectively also enable XPCS

measurements on medically highly relevant protein systems.

Zusammenfassung

Die Untersuchung von Proteinen ist von großer Bedeutung aufgrund ihrer vielfältigen Funktionen in lebenden Organismen und ihrer Rolle in der Ernährung. Eine Technik, die die kollektive Dynamik von Proteinen in Lösung untersucht, ist Röntgenphotonenkorrelationsspektroskopie (engl. *X-ray photon correlation spectroscopy*, XPCS). Mithilfe der hohen kohärenten Röntgenflüsse an modernen Synchrotronanlagen kann XPCS die Dynamik bis hinunter zur molekularen Längenskala auflösen. Allerdings stellt die Empfindlichkeit der Proteine gegenüber Röntgenstrahlung eine große Herausforderung dar.

In dieser Arbeit werden mit XPCS die Auswirkungen der Röntgendosis und der Röntgendosisleistung auf die Struktur und die Dynamik von Proteingelen systematisch untersucht. Bei den Proteingelen handelt es sich um Hühnereiweiß, das bei dreizehn Temperaturen zwischen 50 und 85 °C gekocht wurde. Bei diesen Temperaturen entfalten sich die Proteine im Eiweiß und verbinden sich miteinander, was zur Bildung eines Gelnetzwerks bei Temperaturen $\geq 60\,^{\circ}\mathrm{C}$ führt. Bei diesen Eiweiß-Gelnetzwerken beobachten wir Unterschiede in der Suszeptibilität für Strahlenschäden. Die Gele, die zwischen 63 °C und 70 °C hergestellt wurden, sind empfindlicher gegenüber Strahlungseffekten, und die Gelstruktur wird durch Röntgendosen von 2 bis 8 kGy aufgebrochen, was eine Beschleunigung der Probendynamik bewirkt. Die Eiweiß-Gelnetzwerke, die über 73 °C hergestellt wurden, werden durch denaturiertes Ovalbumin verstärkt, was die Dosisgrenzwerte für Änderungen in Struktur und Dynamik um eine Größenordnung erhöht.

Wie andere Gele zeigen auch die gekochten Eiweißgele eine ballistische Bewegung, bei der einzelne Relaxationsereignisse im Netzwerk Richtungsverschiebungen in den umgebenden Proteinaggregaten verursachen. Aus den XPCS-Ergebnissen leiten wir die Geschwindigkeit der ballistischen Bewegung als Funktion von zehn verschiedenen Photonenflüssen ab und stellen eine lineare Abhängigkeit dieser Geschwindigkeit von der Photonenflussdichte fest. Daraus berechnen wir Grenzwerte für die Röntgenflussdichte, oberhalb derer strahlungsinduzierte Effekte die beobachtete Dynamik dominieren, und finden $\Phi^* = (3 \pm 2) \times 10^{-3}\,\mathrm{ph\,s^{-1}\,nm^{-2}}$ für die strahlungsempfindlichen Gele, die bei $\leq 70\,^{\circ}\mathrm{C}$ hergestellt wurden und $\Phi^* = (0.9 \pm 0.3)\,\mathrm{ph\,s^{-1}\,nm^{-2}}$ für die Gele, die über 70 °C hergestellt wurden. Ein Vergleich mit anderen Probensystemen legt einen

Zusammenhang zwischen Viskoelastizität und Empfindlichkeit gegenüber Röntgenstrahlungseffekten nahe.

In dieser Arbeit wird gezeigt, wie ein Bereich in Bezug auf Dosis und Dosisleistung bestimmt werden kann, in dem die intrinsischen dynamischen und strukturellen Eigenschaften mit XPCS gemessen werden können. Diese Erkenntnisse können genutzt werden, um neue Messverfahren zu evaluieren und den verbesserten kohärenten Röntgenfluss an der nächsten Generation von Röntgenanlagen zu nutzen, was perspektivisch auch XPCS-Messungen an medizinisch hoch relevanten Proteinsystemen ermöglichen wird.

Contents

Chapter 1

Introduction

Proteins are large molecules with a complex structure that arises from three-dimensional folding. They fulfill a variety of tasks necessary for living organisms' functions, for example, as enzymes or antibodies [1]. Thanks to modern artificial intelligence tools, the structure of proteins can, in most cases, be retrieved as soon as the sequence of amino acids is known [2], which is a great achievement. In addition to the proteins' structure, the fulfillment of their functions is determined by their dynamical behavior [3–9]. In contrast to the protein structure, there are still many open questions on the dynamics of proteins. There are different experimental techniques that give insights into the dynamics of samples and that can be applied to the investigations of proteins [10]. One of them is X-ray photon correlation spectroscopy (XPCS).

While most techniques track the diffusion of single tracer particles [11–15], XPCS [16–23] opens up the unique opportunity to study collective dynamics in turbid samples [24, 25]. This is why XPCS recently receives a lot of attention in the context of investigating interactions in crowded protein solutions [26–29]. In an XPCS measurement, a coherent X-ray beam is employed for a sequential illumination of the sample under investigation. If the sample is disordered, the scattering pattern consists of speckles in which the positions of the scatterers inside the sample are encoded. The dynamics of these scatterers inside the illuminated volume can be tracked by correlations of the speckle intensities, and the type of motion can be accessed by fitting Kohlrausch-Williams-Watts functions to the obtained correlation functions.

For a correlation function with a sufficient signal-to-noise ratio, the detector's photon count rate per frame needs to be high enough. Especially in the investigation of fast dynamics on small length scales, a high coherent X-ray flux is required. This poses a challenge for the investigation of biological samples, which are usually extraordinarily sensitive to the energy deposited in the sample by X-rays (dose). This also limits the accuracy of structure determination with X-rays [30–39]. The structure of large proteins can be determined from the diffraction pattern of a

protein crystal [40, 41], where cryo-cooling of the crystal can be used to reduce the propagation of radiation damage through the sample. Thereby, the samples can absorb doses of 10 MGy to 100 MGy before the peaks in the scattering pattern degrade indicating changes to the protein's structure [42–46].

The structure of proteins in (aqueous) solutions is sensitive already to doses in the kGy range [47] as the X-rays generate highly reactive species in the solution [48–51] that react with the proteins. This hampers the investigation of the dynamics of proteins in solution, but it remains elusive how the dose alters the dynamics or whether the dose rate plays a role. So far, XPCS experiments have been successfully performed with protein gels, glasses, and phase-separated protein solutions [27–29, 52–55] where high scattering contrasts and slow dynamics facilitate measurements with low X-ray doses. In most of these experiments, dose and dose rate thresholds were determined from changes in the static scattering.

Recently, it was observed that the dose rate can accelerate the dynamics of oxide, network, and protein glasses [56–61]. However, it still needs to be made clear to which extent this affects other jammed or diffusive systems. In this thesis, the effects of X-ray dose and dose rate are systematically investigated on a protein gel system that was already subject to earlier XPCS experiments: cooked hen egg white [54, 55].

Besides a high amount of water, hen egg white consists of a variety of proteins, where some can be denaturated by heating and subsequently form a stable in-transparent gel network. The denaturation temperatures of the most abundant protein components are distributed over a range from 60 °C to 85 °C, which enables us to generate protein gel networks with different properties by varying the preparation temperature of the egg white samples. This way, we prepare thirteen different egg white gels and investigate structure and dynamics on the gel network's length scale, employing XPCS in the ultra-small angle X-ray scattering geometry.

We identify two classes of gel networks among the egg white samples: a *soft* gel network that is created at preparation temperatures $\leq 70\,^{\circ}\mathrm{C}$ and whose dynamics show a complex dependence on the X-ray dose involving dose-dependent accelerations and slow-downs that set in above thresholds of a few kGy. The second class, we label as *strong* gel networks as they are prepared at higher temperatures leading to a higher density of crosslinks in the gel [62–64]. This makes them less susceptible to radiation effects compared to the *soft* gel networks. All egg white gel samples display linear accelerations of the dynamics as those observed in glassy systems [56–61]. However, for the *soft* gel network, this acceleration is orders of magnitude higher compared to the protein glasses. We interpret this acceleration in the context of a stress relaxation model [65] and derive fluence thresholds below which the intrinsic dynamics dominate the XPCS results.

The approaches for investigating X-ray radiation effects on the structure and dynamics of proteins can help to identify windows of opportunity for future experiments on radiation-sensitive samples. This is especially important in the development of new measurement schemes for the

upcoming fourth generation of synchrotron sources [19, 66, 67] that provide higher coherent fluxes for XPCS experiments.

This thesis is structured as follows: Chapter 2 covers the theoretical foundations for understanding gels, precisely cooked egg white, the employed measurement techniques, and the effects of X-ray radiation on matter, emphasizing the interaction with water. The realization of the experiment is described in Chapter 3, including details on the sample preparation, the experimental setup at the P10 coherence applications beamline, and the measurement protocols. Details on the raw data and their processing are given in Chapter 4. The results are divided into two parts: the results from the static scattering that are related to the sample's structure are presented in Chapter 5, while the XPCS results on the sample dynamics are the subject of Chapter 6. The results from both chapters are unified and discussed in the context of other works in Chapter 7. In the final Chapter 8, the findings are summarized, and an outlook is given.

Chapter 2

Theoretical Concepts

This chapter introduces the theoretical framework necessary to understand how X-ray radiation affects a prototypical egg white protein gel and how we track changes in structure and dynamics with coherent X-ray scattering techniques. Section 2.1 introduces the gel state, where we focus on the theory of gels in Section 2.1.1. The role of gels in food science will be elucidated in Section 2.1.2, especially the role of hen egg white, whose protein components are described in more detail in Section 2.1.3. The employed measurement techniques are introduced in Section 2.2. Section 2.2.1 gives an overview of synchrotron radiation, which is used in both ultra-small angle X-ray scattering, (Sec. 2.2.2) and X-ray photon correlation spectroscopy (XPCS) (Sec. 2.2.3). Section 2.3 covers the interactions of high-energy X-rays with matter. The quantities necessary for quantification of radiation effects, namely flux, fluence, dose, and dose rate, are covered in Sections 2.3.1 to 2.3.3. The last two subsections 2.3.4 and 2.3.5 are dedicated to the radiation-induced radiolysis of water and the subsequent effects on proteins in aqueous solutions.

2.1 Egg White as Prototypical Protein Gel

A topic in condensed matter physics that has received much attention in the last two decades is dynamical arrest in soft matter systems. Dynamical arrest creates solid-like disordered structures with unique properties that are interesting, for example, in the context of food science. These structures arise as the system gets trapped in a non-ergodic state like a gel or a glass. These different non-ergodic states can explained by exploring the phase diagram of a colloidal model system.

2.1.1 Colloidal Gels and Glasses

The following introduction to colloids is based on Ref. [68].

In a colloidal system, large particles (the colloidal particles) are distributed in a medium that consists of much smaller molecules. Due to this size difference, certain aspects of this dispersion medium can be neglected in the theoretical treatment. At the same time, the large size of the colloidal particles leads to longer time scale of the processes in which these particles are involved, facilitating experimental studies with techniques like dynamic light scattering. A common feature of colloidal systems is that the motion of the colloidal particles is irregular, as it is caused by random collisions with the thermally activated molecules from the solvent.

In order to see this random movement of the colloidal particles, they must not exceed certain size limits: the particles need to be small enough such that the displacements from the collisions with the solvent are of relevance, but large enough such that one colloidal particle interacts with multiple solvent molecules at the same time. This last requirement enables us to treat the solvent on a macroscopic level like a fluid whose effect on the motion of the particles can be described in terms of its viscosity or temperature. These considerations limit colloidal particles to sizes of 1 nm to 10 µm.

The colloidal particles move randomly due to collisions with the thermally activated particles from the solvent. This type of motion is also referred to as Brownian motion, as one of the early observers was Robert Brown, who investigated pollen grains in water in 1827. Brownian motion is described in more detail in Sec. 2.2.4.1. In this case, the only interactions between the colloidal particles are hydrodynamics interactions mediated by the solvent.

To study phenomena like phase transitions, other interactions must enter the colloidal model system. The most straightforward case that allows us to study a broad spectrum of phenomena are sphere-shaped colloidal particles. In any case, these particles display two kinds of interaction forces: an attractive van der Waals force [69] and a repulsive hard-sphere interaction that sets in if the volumes of two colloidal particles try to overlap. Charged colloidal particles exert an electrostatic force on each other that is usually repulsive for particles of the same kind [70–74] and that is partly screened by the molecules in the solvent that arrange in a double-layer around the colloidal particle.

The formation of a gel requires a long-range repulsive force, like the electrostatic force, and an additional short-range attractive force, like the van der Waals force mentioned above or depletion forces [75, 76] that attract two colloids whose excluded volumes overlap due to osmotic pressure. This interplay of forces causes competing interactions, also referred to as short-range attraction, long-range repulsion (SALR) interactions. Depending on the volume fraction of the particles ϕ, the attraction strength U between them, and the range of the attractive force ξ [77], the system eventually ends up in different non-ergodic states. In the limit of low volume fraction

and high attractive force, the particles bond to each other, forming chains that interconnect into a fractal-like, percolating network structure with large voids in between that are not occupied by particles [78]. This stabilizing network gives rise to solid-like properties of the system [79, 80] despite the presence of a high amount of liquid in the system. These systems are what we call gels. Material science identifies them by a yield stress below which deformations are elastic [81, 82]. Gel networks can form already at volume fractions as low as $\phi = 10^{-3}$ as a result of a spinodal decomposition where local density fluctuations trigger a demixing of the two phases and the dense phase forms a percolating network [69, 77, 83–85].

A different non-ergodic state is observed in the limit of high volume fractions ($\phi > 0.58$ [77]) and low attractive forces. Here, the distance between the particles decreases, and the long-range repulsive force leads to a caging of the particles between their next neighbors and thereby to dynamical arrest [86–88]. This densely-packed disordered state is called a repulsive glass [89]. Although the structure is comparable to that of a liquid, the viscosity changes dramatically to values above 10^{12} Pa s at the glass transition [90]. These glass transitions can be described on first principles using mode-coupling theory [90, 91]. For an increasing attractive strength, this theory predicts the existence of a second type of glass that is stabilized by the attractive forces. Simulations on dynamical arrest in colloidal suspensions by Zaccarelli and Poon suggest that even at high attractive strengths, this glass is still stabilized by the repulsive forces, but the mean square displacement of the particles is reduced when reaching the scale of the inter-particle bond [89]. In addition, they predict the existence of a dense gel phase at $\phi < 0.62$ where the particles are forming cages similar to a glass, but the particles forming the cages are exchanging over time [89].

There are two common frameworks for describing the formation of a gel network: the *classical* mean field theory by Flory and Stockmayer [92–94] and the more generalized theory of percolation [95]. The classical approach starts with monomers, where each can form up to f bonds with other monomers. The probability for such bond formations is p, independent of the surrounding bonds. The only restriction is that the formation of loops is prohibited. The resulting structure on which the networks may form is a Bethe lattice. Figure 2.1 displays an example of a Bethe lattice where the maximum number of bonds per lattice site is $f = 3$. After bonds have been closed randomly with probability p we can identify clusters on the Bethe lattice, which are sets of two or more sites that are interconnected by closed bonds. The number of closed bonds determines the size s of the cluster. In Fig. 2.1, a cluster of size $s = 6$ is highlighted by a shaded area. The average size of a cluster increases with the bond formation probability p, and at a certain point, an infinite cluster will occur for the first time. This point is called percolation threshold p_c, and the infinite cluster is the gel network [96].

Analytic descriptions of the whole gelation process are complicated, especially on more complex lattices, due to the variety of shapes in which clusters of the same size can come. That is

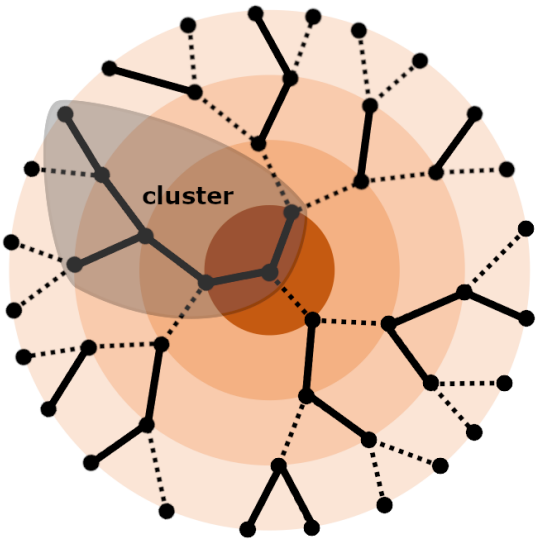

Figure 2.1: Sketch of first three orders of neighboring sites on a Bethe lattice with three next neighbors per site ($f = 3$). Solid lines represent closed bonds (probability p), and dotted lines are open bonds (probability $1 - p$). Closed bonds connect lattice sites to clusters. The largest of these clusters with a size of $s = 6$ in this example is highlighted by a shaded area.

why theoretic descriptions focus on the behavior close to the critical point ($p \to p_c$) [96]. In the case of the Bethe lattice, the cluster size distribution n_s close to the critical point scales like [92, 93, 97]:

$$n_s \propto s^{-5/2} \exp\left((p - p_c)^2 \cdot s\right) \qquad (s \to \infty). \tag{2.1}$$

Percolation theory generalizes the classical approach, which is restricted to the Bethe lattice described above. In percolation theory, the clusters and gels are forming on regular lattices, which is why the number of dimensions is also essential in this framework [96]. There are two ways to introduce the probability p to the lattice and thereby to the cluster/gel formation process: in the first case (bond percolation formalism), all lattice sites are occupied, and p is the probability that a bond between next neighbor sites is formed, analogously to the bond formation on the Bethe lattice. The second case is the site percolation formalism, where p is the probability that a lattice site is occupied and all occupied next neighbor sites contribute to the cluster. In this picture, the smallest cluster size s is equal to one, which corresponds to an occupied site surrounded by unoccupied sites. Although there is, in most cases, no direct translation between the two formalisms, it is commonly accepted that they are equivalent, and in the limit of infinite clusters, yield the same results [98]. The advantage of the site percolation formalism is that it simplifies the realization of computer simulations.

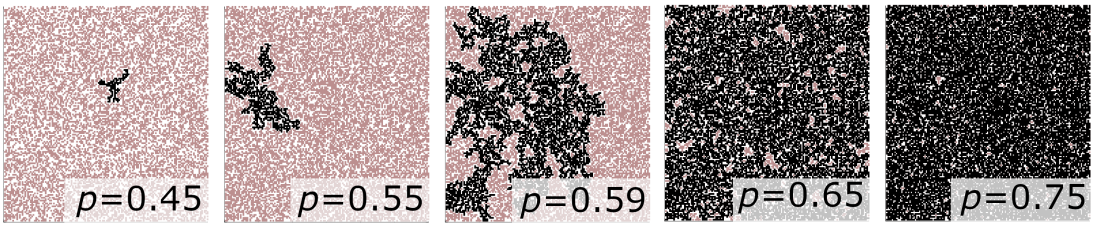

Figure 2.2: Visualization of cluster formation on a square lattice. Here, p is the probability that a lattice site is occupied (pink color). Lattice sites belonging to the largest cluster are marked in black. From left to right, p increases from 0.45 to 0.75, where at $p = 0.59$, a cluster appears that spans across the finite lattice (from top to bottom). Figure adapted from [99].

Figure 2.2 shows a percolation simulation on a finite square lattice that uses the site percolation formalism with different values for the probability p. Occupied sites are pink and the largest cluster of occupied next-neighbor sites is highlighted in black. The size of this cluster increases with increasing p as intuitively expected. In this finite case, the gel is reached by definition as soon as a cluster appears that connects the top row of the lattice with the bottom row. The percolation threshold p_c cannot be derived from a single simulation like in Fig. 2.2 as it is defined in the limit of an infinite lattice and can only be approximated by averaging over a large number of simulations. Moreover, the percolation threshold p_c depends on the dimensions of the system and the number of next neighbors of each lattice site [99].

To describe the size of a complex structure, polymer physicists employ the radius of gyration that is defined via [100]:

$$R_s^2 = \sum_{i=1}^{S} \frac{r_i^2}{s}, \tag{2.2}$$

where i runs over all s lattice sites that are part of the cluster, and r_i is the distance of the ith lattice site to the cluster's center of mass. The relation between the size of a random cluster s (number of connected lattice sites) and the expansion of the cluster (measured via the radius of gyration) is more complex than for compact objects. Imagine, for example, a square in two-dimensional space. If the length of all edges is doubled, the area scales by a factor of $4 = 2^2$. This equals the factor for the increase in length of the edge to the power of the conventional dimensions of the system. The same relation is found for three-dimensional objects in three dimensions where the volume increases by a factor of $8 = 2^3$. This can be generalized to the following expression:

$$\text{mass} \propto \text{length}^{d_f}, \tag{2.3}$$

as Mandelbrot [101] did it. If the dimension d_f in the equation above does not match the Euclidian

dimension of the space, the respective object is called a *fractal* object. In this sense, our clusters formed below the percolation threshold are fractal-like as their fractal dimension is non-integer and smaller than the Euclidian dimension [95]. Simulations on percolation on three-dimensional lattices returned fractal dimensions of $d_f \approx 2.52$ [102–104].

Because of the fractal character, it is difficult to derive the relation between occupation probability p and cluster number distribution $n_s(p)$. But in general, the relation seems to have the form [96]:

$$n_s(p) = s^{-\tau} f[(p - p_c)s^{\sigma}] \qquad (p \to p_c, s \to \infty). \tag{2.4}$$

Here, σ and τ are scaling parameters and we restrict ourselves to the behavior close to the critical point and large cluster sizes s as before in the classical theory. $f(z)$ is the scaling function that currently must be determined via computer simulations for most lattices. In the classical theory on the Bethe lattice, f takes an exponential form, and the scaling parameters are $\tau = \frac{5}{2}$ and $\sigma = 1/2$ [96].

For percolation theory, simulations on different three dimensional lattices yield $\tau = 2.19$ [102, 103, 105, 106] and $\sigma = 0.45$ [103, 105] independent of the structure of the lattice. Even simulations on a continuum [107, 108] yield the same exponents within the error bars as their discrete lattice counterparts, which confirms that close to the critical point, where the cluster sizes become large compared to the distance between neighboring lattice sites, details on the molecular level become less important [96]. This feature of percolation theory is called *universality*. In this understanding, the classical theory becomes just another universality class in the percolation theory framework.

Experimental validation is required to determine if one of the universality classes (classical theory or percolation theory in three dimensions) can describe a gel's formation. One quantity accessible in light scattering experiments is the radius of gyration[109–111]. However, these measurements require a dilution of the gel sample during which the cluster radius might increase [96], and higher precision is necessary to discriminate between different theories. Nevertheless, percolation theory's description of the gel's structure seems "adequate" [96]. Measurements of viscosity and elastic modulus [112, 113] are easier to realize in situ, but the comparison to the quantities predicted by the theories is more difficult [96]. Thus there is no conclusion yet if one of the two universality classes is observed in an experiment.

So far, we have only regarded gel formation in systems where the bonds once formed have an infinite life. This assumption is applicable, for example, for covalent bonds formed during chemical gelation. However, there is another class of gels, physical gels, where the bonds are formed via interactions of the order of $k_B T$ and have a large but finite lifetime. Due to the continuous breaking and reconnecting of the bonds, the gel turns into a highly viscous liquid [114], and dynamics need to be taken into account in the description of a physical gel. This

inhibits the application of percolation theory as it can only describe the static state [115].

2.1.2 Food Protein Gels

During the manufacturing of food, one important aspect is that it can be broken up by teeth as a first step in digestion. To accomplish this, the forces between the food components must not be too strong, but different textures in food are nevertheless desirable [116, 117]. This is where gels come into play, as they possess elastic and liquid characteristics at the same time. These arise from the three-dimensional network that can retain high amounts of liquids, and that defines the texture of the resulting food. In food gels, the gelling agents that are encountered most often are polysaccharides and proteins [118], where we will focus on the latter type of gel. Well-known examples of protein gels are yogurt, tofu, or cooked hen eggs [116, 118]. Protein gels are the results of protein denaturation and subsequent gelation, so a deeper understanding of proteins themselves is necessary.

Proteins consist of a chain of amino acids and obtain their function via a three-dimensional folding. There are 20 different amino acids encountered in proteins, and they all have to main parts: a backbone necessary for the binding in the chain of amino acids and a specific side chain that differs, for example, in charge or binding properties. Typically, 50 to 2000 amino acids are present in a protein, and the sequence in which they occur is called *primary structure* (e.g. [119]). Due to the interactions of the side chains of neighboring amino acids, three-dimensional repeating structures can form like α helices [120], which are *secondary structures*. But the amino acids do not only interact with their next neighbors but also with the side chains of amino acids that are far away in the linear sequence. These interactions cause a complex folding of the chain into the *tertiary structure* of the protein. Depending on the folding and the side chains that are exposed on the surface or buried in the protein's interior, it can bind to other proteins, lipids, etc., and perform important tasks like transportation in living organisms (e.g. [119]).

The folded state of the protein is not stable, and changes in temperature, pH, or pressure can induce changes to the three-dimensional structure of the protein, like unfolding. The sequence of amino acids remains unchanged. This denaturation of the protein affects not only the structure but also physiochemical and biological properties like the exposure of reactive groups [121]. In some cases, the denaturated protein can refold into its original shape once the outer parameters are reset, but in most cases, protein denaturation is irreversible, especially under extreme conditions [121]. The exposure of reactive groups in the denaturated state makes it more likely that the proteins aggregate. These aggregates are eventually arranged in a percolating fractal structure, the gel network.

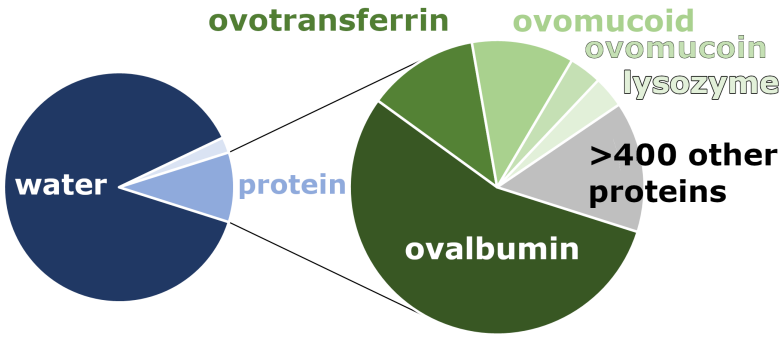

Figure 2.3: Left chart: 10 % of the egg white is made up by proteins. Right chart: The most abundant proteins are ovalbumin (54 %), ovotransferrin (12 %), ovomucoid (11 %), ovomucoin (3.5 %), and lysozyme (3.4 %).

2.1.3 Hen Egg White

In a fertilized bird egg, the role of the egg white is to avert damage from the egg yolk and to serve nutrients for the embryo [122]. Due to their high protein content, egg white and egg yolk have also held significant importance in the human diet since the beginning of human settlement and animal domestication [123]. In western Europe, the eggs of chicken (hen eggs) are most widely used. The egg white's ability to form foams or gels and its adhesion properties makes it not only important for food science applications [121, 124, 125] but also for the development of various bio-materials like degradable packaging [126–129].

Hen egg white consists mostly of water (≈88 %) and proteins (≈10 %). Up to now, 400 unique protein species were identified in hen egg white [122, 130–140], among which ovalbumin, ovotransferrin, ovomucoid, ovomucoin, and lysozyme form the largest fractions

Ovalbumin

With 54 % [62] of the total protein content, ovalbumin [141–144] is the most abundant protein in hen egg white. It has a molecular mass of 45 kDa [145] and a Stokes radius of ≈ 26 nm in the native form [146, 147]. Ovalbumin can be thermally denaturated, and the temperature at which this process starts depends on the environment: In fresh hen egg white, the first proteins start to denaturate slightly around 70 °C [63, 148, 149], where they forms co-aggregates with the ovotransferrin (Sec. 2.1.3) making the gel network stiffer. Unlike the other major protein components of hen egg white, ovalbumin has four free sulfhydryl groups [150]. For other protein systems, like β-lactoglobulin, it has been reported that sulfhydryl groups act as an agent for covalent disulfide bonds [151]. The formation of disulfide bonds has also been observed in egg

white [64], especially between the egg proteins ovalbumin and lysozym [152]. But the exact role of ovalbumin's sulfhydryl groups in the egg white aggregation and gelation and if other, non-covalent forces might increase the elasticity in the same way is still under investigation [153]. If the egg white is stored, ovalbumin converts into the more heat-stable S-ovalbumin [154, 155], that denaturates around 82 °C [149]. The denaturation temperature of pure ovalbumin is even higher and around 87 °C [149].

Ovotransferrin

Ovotransferrin [156, 157], formerly known as conalbumin, makes up 12 % of the protein content in hen egg white [62]. It plays a key role in the transport of ferric ions to the embryo as it can bind two Fe^{3+} ions [158] and is effective against viruses and microbes [159–167]. It's molecular mass is 78 kDa to 80 kDa [167]. Like ovalbumin, ovotransferrin displays heat-induced denaturation that sets in at $\approx$ 50 °C in the hen egg environment [149]. Between 60 °C to 65 °C the whole ovotransferrin content is denaturated, and it forms a weak gel [62, 149, 168, 169].

Ovomucid

About 11 % of the hen eggs protein content are made up by ovomucid [170, 171]. It has a molecular mass of 28 kDa [150], and in contrast to ovalbumin and ovotransferrin, it is heat-stable and is not denaturating in the regime below 100 °C [129]. Ovomucid is suspected to be the major allergen in egg [172, 173]

Ovomucin

With a molecular mass of 200 kDa to 8000 kDa ([174] and references therein), ovomucin [175, 176] is the largest protein within the major protein components of egg white. It makes up 3.5 % of the egg white [62]. Liquid egg white at room temperature can be subdivided into a thin and a thick part, where the ovomucin content in the thick part is four times higher compared to the thin part, giving rise to a gel network that reduces bacterial movement towards the embryo [150, 177]. Although no thermal denaturation of ovomucin has been reported [169], it has been recently shown that it is involved in the early gel formation in egg white at 72 °C [178] maybe via the close interaction with lysozyme [179]. Ovomucin is also important for the foaming properties of egg white [180] and is used as a foam stabilizer [181].

Lysozyme

About 3.4 % of the proteins in hen egg are lysozyme [62]. It has a molecular weight of 14.3 kDa [62] and it's four disulfide bridges make it unusually compact [167]. Lysozyme is used as a food

preservative due to its antibacterial activity [182, 183] In egg white, lysozyme starts to denaturate at 57 °C and most of the lysozyme content is denaturated at 75 °C [149, 169].

Heat-induced Gel Formation

The different denaturation temperatures of the protein components of egg white enable the creation of gel networks with different structures and dynamics. Bonilla et al. [184] performed rheology and microscopy measurements on egg white samples that were heated to 69 °C, 72 °C and 75 °C, which equals about 10 %,50 % and 90 % denaturation of the total content of ovalbumin. The gel network at the lowest temperature, which is primarily formed by ovotransferrin, has a low yield stress and is not self-supporting at room temperature. Upon increasing the preparation temperature to 72 °C and above, Bonilla et al. observed a significant increase in yield stress.

Their super-resolution stimulated emission depletion microscopy images revealed that small aggregates with a size of $0.07\,\mu m^2$ are forming that assemble into a gel network in a second step. With increasing temperature, additional particles of the same size form and attach to the network, introducing more crosslinks that increase the rigidity.

2.2 X-ray Scattering Techniques

X-rays are electromagnetic waves with wave lengths λ between 10^{-8} m and 10^{-11} m. The electric field $\vec{E}$ and the magnet field $\vec{H}$ are perpendicular to each other and to the direction of propagation, which is given by the wave vector $\vec{k}$ ($|\vec{k}| = 2\pi/\lambda$). The spatial and temporal variation of the electric field with amplitude E_0 at a position $\vec{r}$ and time t can be described by plane waves of the form (e.g. [185]):

$$\vec{E}(\vec{r},t) = \vec{\varepsilon} E_0 e^{\vec{k}\cdot\vec{r}-\omega t}. \tag{2.5}$$

Here, $\vec{\varepsilon}$ is the polarization vector of the electric field, and ω is the angular velocity. If the X-ray is scattered, the wave vector $\vec{k}$ is altered by an amount $\vec{q} = \vec{k} - \vec{k}'$, where $\vec{k}'$ is the wave vector of the scattered radiation. We are interested in the case of elastic scattering, where the wave length of the scattered X-rays is the same as the wave length of the incoming X-rays, as this is the scenario where the X-rays carry information on the scattering object and are able to interfere with each other. For elastic scattering, the absolute value of the momentum transfer $\vec{q}$ is given by (e.g. [185]):

$$|\vec{q}| = 2|\vec{k}|\sin\theta = \left(\frac{4\pi}{\lambda}\right)\sin\theta, \tag{2.6}$$

where θ is the scattering angle.

2.2.1 Synchrotron Radiation

In this section, we will summarize the basic principles behind the generation of synchrotron radiation by accelerated free electrons and look at some of the unique characteristics that make synchrotron radiation a suitable tool for investigating a broad spectrum of phenomena.

Charged particles are the source of electromagnetic fields, as described by the Maxwell equations. As long as the particle is in uniform motion through a vacuum, the electrostatic field points radially away from the particle to infinity. If the particle is accelerated, the information on the acceleration leaves the particle with the speed of light, causing distortions to the electrostatic field. These distortions are the electromagnetic radiation that we are interested in (e.g. [186]). If magnets realize the acceleration perpendicular to the direction of travel of the particle, like in circular synchrotrons, the emitted radiation is called synchrotron radiation. The spatial distribution of the radiation emitted in this acceleration geometry can be calculated from the Liénard-Wiechert potential [187, 188]. Details on the calculation can be found in the work of Wiedemann [186]. The final expression for the angular distribution of the radiation power takes the form:

$$\frac{\mathrm{d}P}{\mathrm{d}\Omega} \propto \beta^4 \frac{(1-\beta\cos\vartheta)^2 - (1-\beta^2)\sin^2\vartheta\cos^2\phi}{(1-\beta\cos\vartheta)^5}, \tag{2.7}$$

where β is the particle's velocity normalized to the velocity of light. ϑ is the angle between the direction of the instantaneous velocity of the particle and the direction of acceleration, and ϕ is the angle in the plane perpendicular to the direction of the velocity as indicated in Fig. 2.4.

For highly relativistic particles, angular distribution is confined to a cone in the forward direction with an opening angle that is proportional to the inverse of the Lorentz factor [186]:

$$\nu_\gamma = \pm\frac{1}{\gamma} = \pm\sqrt{1-\beta^2}. \tag{2.8}$$

If users at modern synchrotron facilities want to adapt the properties of the emitted synchrotron radiation, insertion devices like undulators or wigglers are used. These devices consist of altering pairs of magnets that force the electrons into a sinusoidal movement. In an undulator, the wavelength of the emitted radiation is proportional to the period length between the magnets λ_p but is reduced by a factor γ^2, which enables the generation of hard X-rays. The two Lorentz factors γ arise from the relativistic contraction on the one hand and from the Doppler effect on the other hand [189]

The quality of synchrotron radiation can be described in terms of the brilliance $\mathcal{B}$ that is essentially the density of photon flux in phase space, evaluated at the origin of the phase space [190]

$$\mathcal{B} = \left.\frac{\mathrm{d}\mathcal{F}}{\mathrm{d}\vartheta\mathrm{d}\phi\mathrm{d}x\mathrm{d}y}\right|_0. \tag{2.9}$$

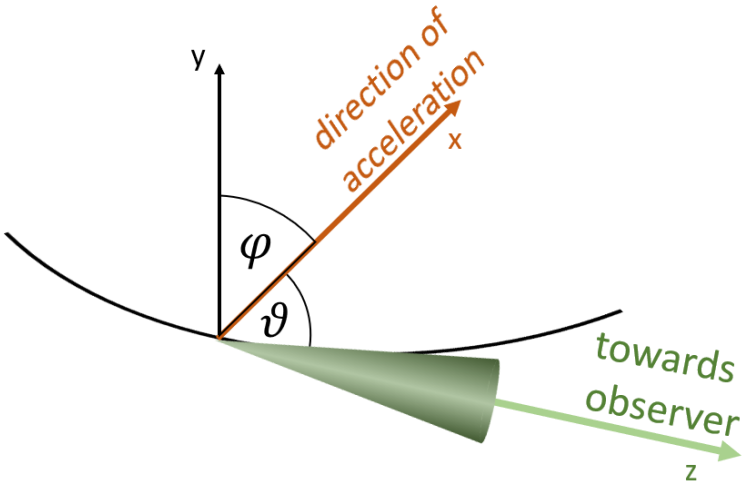

Figure 2.4: Sketch on the shape of synchrotron radiation emitted by a particle that is kept on a circular track. The z-axis is defined in the direction of the velocity of the particle, while the x-axis points in the direction of the acceleration. The distribution of the emitted radiation can be described in terms of the angles ϕ and ϑ. For highly relativistic particles, the radiation power is emitted into a cone in the forward direction. Figure is redrawn after [186].

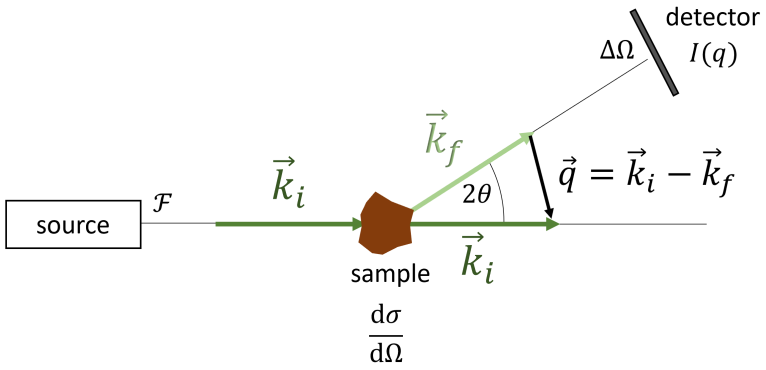

Figure 2.5: Sketch of a basic scattering experiment. The X-ray source emits a photon flux $\mathcal{F}$ that is scattered from a sample under an angle 2Θ into the solid angle $\Delta\Omega$ where a detector records the intensity I. The momentum transfer $\vec{q}$ is the difference of the wave vector of the incoming wave $\vec{k}_i$ and the scattered wave $\vec{k}_f$.

.

Here, ϑ, ϕ, x, and y are the angles and coordinates as indicated in Fig. 2.4. At the PETRA III storage ring, brilliances beyond 10^{21} ph s^{-1}mm^{-2} mrad^{-2} 0.1%BW are reached [191] where BW is the bandwidth .

2.2.2 Ultra-Small Angle X-ray Scattering

Figure 2.5 shows a basic setup for a scattering experiment: The X-ray flux $\mathcal{F}$ impinges on the object under investigation and causes scattering of the intensity I into the solid angle $\Delta\Omega$. The ratio of scattered intensity to incoming flux and detection angle is the differential scattering cross-section

$$\left(\frac{\mathrm{d}\sigma}{\mathrm{d}\Omega}\right) = \frac{I}{\mathcal{F}\,\Delta\Omega}. \tag{2.10}$$

If the scattering object is a single free electron, the differential scattering cross-section becomes (e.g. [185]):

$$\left(\frac{\mathrm{d}\sigma}{\mathrm{d}\Omega}\right) = r_0^2 |\vec{\varepsilon}\cdot\vec{\varepsilon}'|^2, \tag{2.11}$$

where $r_0 \approx 2.8 \times 10^{-15}$m is the Thomson scattering length and $|\vec{\varepsilon}\cdot\vec{\varepsilon}'|^2$ is a polarization factor that can be omitted as we will restrict our considerations to small scattering angles. Suppose we want to describe the scattering from an atom. In that case, we need to multiply the Thomson scattering length r_0 by an atomic scattering factor f that depends on the photon energy and the

scattering angle where the latter can be neglected at small scattering angles [192]. The general form of the atomic scattering factor is [192]:

$$f = Z + f'(E) + if''(E), \tag{2.12}$$

where Z is the number of electrons and f' and f'' are the anomalous scattering factors that take the rapid change of scattering at the absorption edges of a material into account.

We want to obtain an expression for the scattered intensity as a function of the momentum transfer $I(q)$ from which we can draw conclusions on the structure of the sample. The starting point for systems that are more complex than a single electron is the scattering amplitude $A(\vec{q})$ that is related to the differential scattering cross-section via:

$$\left(\frac{\mathrm{d}\sigma}{\mathrm{d}\Omega}\right)(\vec{q}) = A(\vec{q})A^*(\vec{q}) = |A(\vec{q})|^2. \tag{2.13}$$

For the more general case scattering of scattering from a volume V containing N particles with individual scattering lengths $b_p = r_0 f_p$, it is helpful to introduce the scattering length density $\rho(\vec{r})$. It is related to the density of particles $\rho_p(\vec{r}) = N/V$ via $\rho(\vec{r}) = \sum_{p=1}^{N} b_p \rho_p(\vec{r})$ [192]. With this we can express the scattering amplitude $A(\vec{q})$

$$A(\vec{q}) = \int_V \rho(\vec{r}) e^{-i\vec{q}\cdot\vec{r}} \mathrm{d}\vec{r}. \tag{2.14}$$

Here, we applied the Born approximation that is valid for weakly scattering systems like proteins in solution. With this expression, the differential scattering cross-section becomes

$$\left(\frac{\mathrm{d}\sigma}{\mathrm{d}\Omega}\right)(\vec{q}) = A(\vec{q},t)A^*(\vec{q},t) = \int_V \int_V \rho(\vec{r},t) e^{-i\vec{q}\cdot\vec{r}} \rho(\vec{r}',t) e^{i\vec{q}\cdot\vec{r}'} \mathrm{d}\vec{r}\mathrm{d}\vec{r}'. \tag{2.15}$$

The contributions of the scattering from the particles themselves and interference due to the spatial configuration of the particles can be separated by substituting $\vec{r} = \vec{r_i} + \vec{u}$, where $\vec{r_i}$ is the position of the center of mass of particle i. With this, the expression above becomes:

$$\left(\frac{\mathrm{d}\sigma}{\mathrm{d}\Omega}\right)(\vec{q}) = \sum_{i=1}^{N} e^{-i\vec{q}\cdot\vec{r}_i} \int_{V_{\mathrm{par}}} \rho_i(\vec{u}) e^{-i\vec{q}\cdot\vec{u}} \mathrm{d}\vec{u} \sum_{j=1}^{N} e^{i\vec{q}\cdot\vec{r}_j} \int_{V_{\mathrm{par}}} \rho_j(\vec{u}) e^{i\vec{q}\cdot\vec{u}'} \mathrm{d}\vec{u}'. \tag{2.16}$$

The integration over the individual particles is the particle's form factor amplitude $f_j(\vec{q}) = \int_{V_p} \rho_j(\vec{u}) e^{-i\vec{q}\cdot\vec{u}} \mathrm{d}\vec{u}$. In the limit of large q values, the form factor amplitude decays to zero due to the large fluctuations of the phase factors. If we assume that only one kind of particle is present in the system, e.g., the system is monodisperse, the form factor amplitudes can be taken out of

the summation and combined into a form factor intensity $|f(\vec{q})|$:

$$\left(\frac{\mathrm{d}\sigma}{\mathrm{d}\Omega}\right)(\vec{q}) = |f(\vec{q})|^2 \sum_{i=1}^{N}\sum_{j=1}^{N} e^{-i\vec{q}\cdot\vec{r}_i} e^{i\vec{q}\cdot\vec{r}_j}. \tag{2.17}$$

In a scattering experiment on particles in solution, where the scatterers are a large number of particles with different orientations, we will measure the orientational average of the form factor intensity $P(q) = \langle|f(\vec{q})|^2\rangle_\Omega$. For spherical monodisperse particles, Eq. (2.17) can be completely decoupled like [e.g. [192]]:

$$\left(\frac{\mathrm{d}\sigma}{\mathrm{d}\Omega}\right)(q) = P(q)S(q). \tag{2.18}$$

The remaining integration is summarized in the structure factor $S(q)$ that depends on the configuration of the particles. For some particle shapes, the form factor can be calculated analytically. For example, for a homogeneous sphere of radius R, $P(q)$ becomes:

$$P(q) \propto \left[3\left(\frac{\sin(qR) - qR\cos(qR)}{q^3R^3}\right)\right]^2. \tag{2.19}$$

The structure factor is related to the Fourier transform of the pair correlation function $g(r)$ [e.g., [193]]

$$S(q) = 1 + \phi\int (g(r)-1)e^{i\vec{q}\cdot\vec{r}}\mathrm{d}\vec{r} \tag{2.20}$$

$$\overset{\text{isotropic}}{=} 1 + 4\pi\phi\int_0^\infty [g(r)-1]r^2\frac{\sin(qr)}{qr}\mathrm{d}r. \tag{2.21}$$

Scattering from fractals

In Section 2.1.1, we introduced fractals as objects whose attributes like mass or surface do not scale like those of compact objects and whose structures show self-similarity. According to this scaling behavior, fractals can be divided into categories like mass, surface, pore, fat, or multifractals. Details on these categories can be found in Ref. [194]. All types of fractals have in common that at an intermediate range in momentum transfer q, the intensity scales like [195]

$$I(q) \propto q^{d_s - 2(d_m + d_p) + 2d}. \tag{2.22}$$

Here, d_s, d_m, and d_p are the surface, mass, and pore fractal dimensions, respectively, and d is the Euclidian dimension of space. For example, for a mass fractal in three dimensions, the following

relations hold [193]:

$$0 < d_m < 3 \qquad d_m = d_s \qquad d_p = 3,$$

such that the intensity scales like $I(q) \propto q^{-d_m}$. Similarly, for a surface fractal in three dimensions, the fractal dimensions fulfill [194, 196]

$$2 < d_s < 3 \qquad d_m = d_p = 3,$$

such that the intensity scales like $I(q) \propto q^{d_s-2}$. With these considerations, we can already distinguish surface from mass fractals by looking at the scattering intensity. If the intensity decays with an exponent $-\delta$ and δ is smaller than the Euclidian dimension, we are dealing with a mass fractal. In contrast, for $d < \delta < d-1$ the fractal object belongs to the category of surface fractals [194].

For an ideal fractal, the self-similarity and scaling laws hold on all length scales. For a physical system, this assumption is only valid on intermediate length scales and, thereby, at intermediate values of q. This behavior can be introduced to Eq. (2.22) by adding upper and lower cut-off lengths in q. The lower limit is related to the largest distance between two points of the fractal that is comparably large for a percolating fractal network. The upper limit in q is given by the size of the smallest building block of the fractal, which is the size of the protein microaggregates in our case. Empirical models that are built on these assumptions are the Beaucage [197, 198] and Guinier-Porod [199] models. We will concentrate on a description in terms of fractal dimensions in the analysis of the USAXS data.

2.2.3 Coherent Scattering Techniques and Correlation Functions

Not only information on the structure can be obtained from X-ray scattering experiments, but also information on the dynamics of a sample by illuminating with coherent X-rays and correlating the intensities of the speckles in the scattering. This is done in XPCS, which will be introduced in the following section.

As explained in the last section, the scattered intensity, precisely the structure factor $S(q)$ depends on the spatial position of the particles itself and the positions of the particles relative to each other. Thus, changes in this configuration due to the movement of the particles should be encoded in the scattered intensity. However, if we illuminate the sample with incoherent X-rays, the information, especially on equilibrium dynamics, is lost. This can be avoided by using coherent X-rays, which introduce speckles to the scattering pattern that contain information on the density distribution.

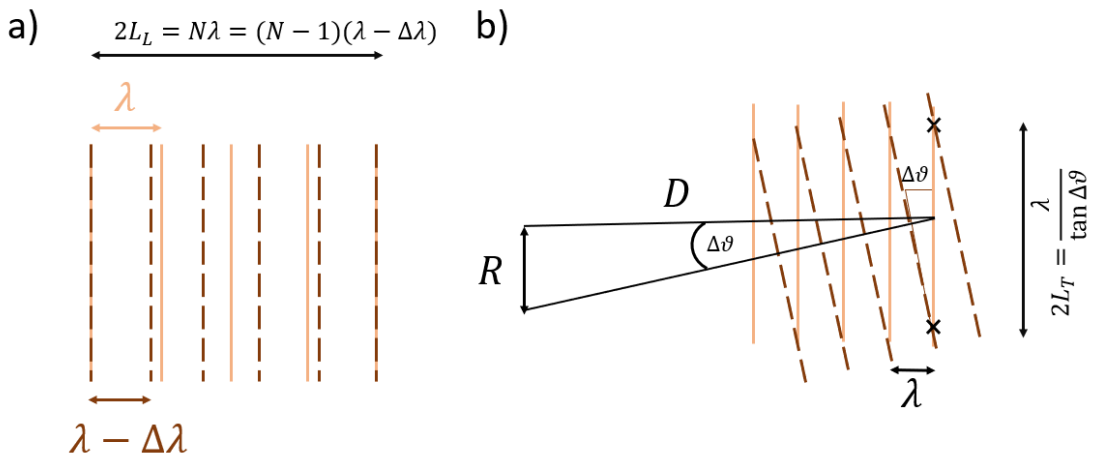

Figure 2.6: Sketch of different coherence lengths. (a) Two waves with slightly different wavelengths λ and $\lambda - \Delta\lambda$, indicated by different colors and line styles, propagate in the same direction. The distance after which they are in phase again is two times the longitudinal coherence length $2L_L$. (b) Two waves propagate in directions that differ by an angle $\Delta\vartheta$ as their origins at a distance D were apart by a distance R are different. The distance between two points where the wavefronts are in phase is twice the transverse coherence length $2L_T$ (Fig. redrawn after [185]).

2.2.3.1 Coherence

X-rays can deviate from the ideal plane wave in two ways: longitudinal and transverse to the direction of propagation. The degree of coherence can be quantified by introducing the longitudinal coherence length L_L and the transverse coherence length L_T. Figure 2.6 illustrates how these are related to the bandwidth and size of the X-ray beam.

In Fig. 2.6(a), two waves with slightly different wavelengths λ and $\lambda - \Delta\lambda$ propagate in the same direction. After a distance of $N\lambda$ has been covered, they are in phase again as the second wavefront with wavelength $\lambda - \Delta\lambda$ has performed an additional oscillation. We define that this distance is twice the longitudinal coherence length and write (e.g. [185]):

$$2L_L = N\lambda = (N+1)(\lambda - \Delta\lambda). \tag{2.23}$$

For XPCS, X-rays with a high degree of coherence are necessary where $\Delta\lambda \ll \lambda$, which results in $N \gg 1$. With this, the second part of Eq. (2.23) can be rearranged using $N \approx \lambda/\Delta\lambda$, which is the inverse of the bandwidth. Insertion in Eq. (2.23) yields

$$L_L \approx \frac{1}{2}\frac{\lambda^2}{\Delta\lambda}. \tag{2.24}$$

The case of transverse coherence is depicted in Fig. 2.6(b) where waves with the same wavelength λ propagate in directions that differ by an angle $\Delta\vartheta$. We define the transverse coherence length L_T as twice the distance between two neighboring points along one wavefront where the wave is in phase with the second wave. Looking at the triangle on the right in Fig. 2.6(b), this can be expressed by (e.g. [185]):

$$2L_T = \frac{\lambda}{\tan(\Delta\vartheta)}. \tag{2.25}$$

Again, we restrict our considerations to situations where $\Delta\vartheta$ is small, and the approximation $\tan\theta \approx \theta$ holds. If the differences in the direction of propagation are caused by the spatial extension R of the X-ray source at a distance D, we can also replace $\tan\Delta\vartheta = R/D$ and Eq. (2.25) becomes:

$$L_T = \frac{1}{2}\frac{\lambda}{(R/D)} = \frac{\lambda}{2}\left(\frac{D}{R}\right). \tag{2.26}$$

The transverse coherence length is often split into a vertical and a horizontal part. Together with the longitudinal coherence length, they span the coherence volume V_c. Typical coherence lengths at the third-generation synchrotron source PETRA III are [200, 201]:

$$L_L = 1 - 5\,\mu\text{m}, \qquad L_T^{\text{hor.}} = 10 - 40\,\mu\text{m}, \qquad L_T^{\text{vert.}} = 260 - 280\,\mu\text{m}.$$

2.2.3.2 X-ray Photon Correlation Spectroscopy

If (partially) coherent light is scattered from a disordered but static medium, the scattering pattern consists of sharp fringes, so-called speckles [202–204]. This speckle pattern changes as soon as the scatterers within the medium are moving. The concept of XPCS is to monitor these fluctuations using second-order correlation functions. In the case of a detector with a single pixel with a position matching the momentum transfer $\vec{q}$, this second-order correlation function of the recorded intensities $I(t)$ would be of the form

$$g^{(2)}(\vec{q},\tau) = \frac{\langle I(\vec{q},t)I(\vec{q},t+\tau)\rangle_t}{\langle I(\vec{q},t)\rangle_t^2}, \tag{2.27}$$

where $\langle\rangle_t$ denotes an average over the measurement time t. In XPCS experiments, large two-dimensional detectors are employed, which increases the statistics of the correlation function. In this case, regions of interest (ROIs) need to be defined, and an average $\langle\rangle_p$ over the pixels in the ROI is introduced to the expression of the correlation function

$$g^{(2)}(\overline{q},\tau) = \frac{\langle\langle I(\vec{q},t)I(\vec{q},t+\tau)\rangle_t\rangle_p}{\langle\langle I(\vec{q},t)\rangle_t\rangle_p^2}. \tag{2.28}$$

In our case, the ROIs will be concentric annuli around the position of the direct beam, which is why we lose the information on the direction of $\vec{q}$ and replace $\vec{q}$ with the average momentum transfer $\overline{q}$ of the ROI. For simplicity and readability, we will refer to $\overline{q}$ with q from now on. The first order correlation function that corresponds to Eq. (2.28) is the $g^{(1)}$ function that correlates the electric fields $E(t)$:

$$g^{(1)}(q,\tau) = \frac{\langle\langle E(q,t)E(q,t+\tau)\rangle_t\rangle_q}{\langle\langle E(q,t)\rangle_t\rangle_q^2}. \tag{2.29}$$

It can also be expressed in terms of the structure factor introduced in Sec. 2.2.2 via $g^{(1)}(q,\tau) = S(q,\tau)/S(q,0)$ which illustrates the relation to the trajectories of the scatterers [22]. If the statistics of the intensities are Gaussian distributed, as for partially coherent light, the $g^{(2)}$ and $g^{(1)}$ function are related via the Siegert relation [205, 206]

$$g^{(2)}(q,\tau) = 1 + \beta|g^{(1)}(q,\tau)|^2. \tag{2.30}$$

The speckle contrast β considers the degree of coherence of the scattered light and is related to the coherence volume [207, 208]. For fully coherent light, β is equal to unity.

An expression for the $g^{(1)}$ function that works well for most sample systems is a Kohlrausch-Williams-Watts (KWW) expression that describes an exponential decay with a decay rate Γ and an exponent k [209]:

$$g^{(1)}(q,\tau) = \exp\left(-(\Gamma\tau)^k\right). \tag{2.31}$$

Insertion into Eq. (2.30) gives:

$$g^{(2)}(q,\tau) = 1 + \beta\exp\left(-2(\Gamma\tau)^k\right). \tag{2.32}$$

Figure 2.7 displays the impact of the parameters β, Γ and k on the shape of the function. In the semi-logarithmic plot, a variation of Γ causes a shift of the $g^{(2)}$ function along the time axis while keeping the slope of the decay. The slope can be adapted through the parameter k while β defines the intercept with the y-axis. All three parameters typically depend on the momentum transfer q.

In the case of dynamics that are out of equilibrium, a description with $g^{(2)}$ functions obtained like in Eq. (2.28) is not useful due to the averaging over the measurement time. Instead, we can employ a two-time correlation function (TTC) [210]:

$$c^{(2)}(q,t_1,t_2) = \frac{\langle I(\vec{q},t_1)I(\vec{q},t_2)\rangle_p}{\langle I(\vec{q},t_1)\rangle_p\langle I(\vec{q},t_2)\rangle_p}. \tag{2.33}$$

For a specific value of q, a TTC is a two-dimensional map that is symmetric along the $t_1 = t_2$ diagonal. An example is shown in Fig. 2.8(a). Similar to the $g^{(2)}$ function, the values of the TTC

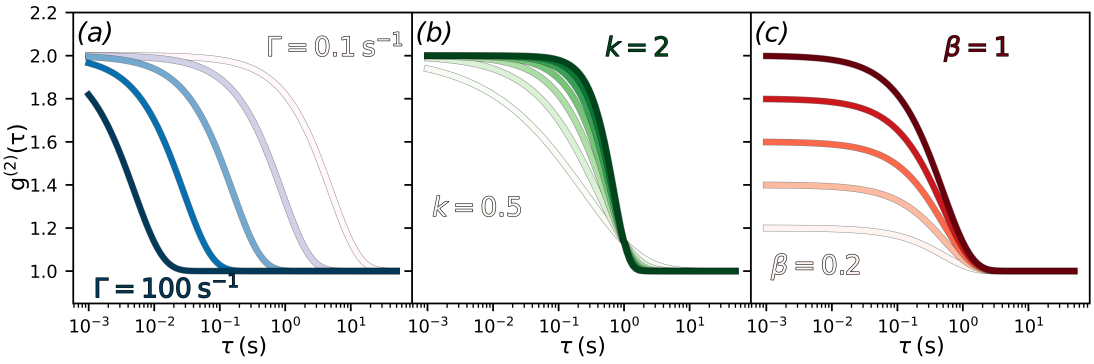

Figure 2.7: Effect of variation of Γ, k or β on the shape of the $g^{(2)}$ function. The parameters that are not varied are set to one. (a)The decay rate Γ is varied between $0.1\,\mathrm{s}^{-1}$ to $100\,\mathrm{s}^{-1}$, causing a shift of the decay in time while keeping the slope in the semi-logarithmic representation. (b) The KWW exponent k is varied between 0.5 and 2. The decay of the $g^{(2)}$ function gets steeper upon increasing k. (c) The contrast β is increased from 0.2 to 1 leading to an increase of the y-intercept.

vary between one and the speckle contrast β. We want to extract $g^{(2)}$ functions from the TTC to apply KWW fits. Therefore, we use $g^{(2)}$ cuts that start at different waiting times $t_w = t_1 = t_2$ on the diagonal of the TTC such that the evolution of the system can be tracked by comparing cuts from different waiting times. There are two directions in which the $g^{(2)}$ cuts can be extracted: either horizontally parallel to one of the time axes or diagonally, perpendicular to the $t_1 = t_2$ diagonal [211]. In this work, we will employ the horizontal cuts as indicated by the arrows in Fig. 2.8(a). The statistics of these $g^{(2)}$ cuts are increased by averaging along small bins along the t_2-axis (see Sec. 4.4.1 for details). Figure 2.8(b) shows the $g^{(2)}$ cuts from the TTC in (a) fitted with a KWW expression.

2.2.4 Fingerprints of Dynamics in XPCS Results

XPCS measurements and the results from KWW-type fits introduced above can be used to discriminate between different types of motions. In Sec. 2.1, we encountered the colloidal model systems that display Brownian motion for non-interacting colloidal particles. In Sec. 2.2.4.1 below, we will approach Brownian motion from a mathematical point of view and derive features of the $g^{(2)}$ functions obtained from systems that display Brownian motion. The other type of dynamics relevant for this study is stress-relaxation motion, as it is encountered in gels or glasses. This will be treated in Sec. 2.2.4.2.

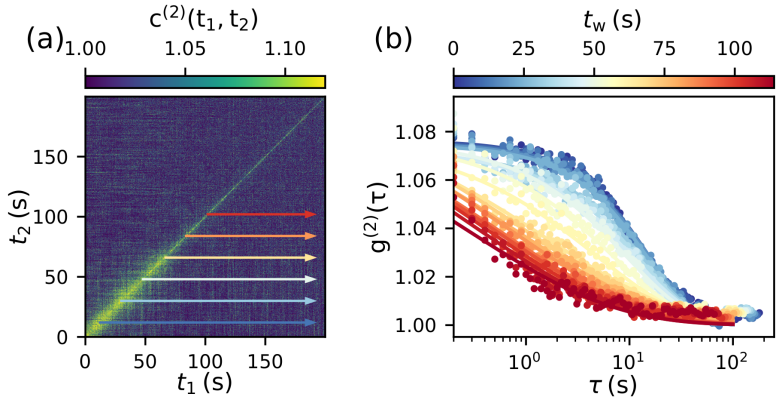

Figure 2.8: Example for TTC and how $g^{(2)}$ cuts are extracted. (a) TTC from a measurement with 4000 frames recorded in 200 s. The width of the TTC along the $t_1 = t_2$ diagonal decreases with increasing time, indicating an acceleration of the dynamics. The horizontal arrows indicate some positions where the $g^{(2)}$ cuts are extracted in the horizontal direction. (b) $g^{(2)}$ cuts for different waiting times t_w. The colors match the colors from panel (a). The data points were fitted with a KWW function (Eq. (2.32)).

2.2.4.1 Brownian motion

Non-interacting colloidal particles display a random motion called Brownian motion caused by collisions with the thermally activated molecules of the solvent. The solvent molecules collide with the colloidal particles on time scales of 10^{-14} s, which causes a rapidly varying force $\vec{f}(t)$ on the colloidal particle. The resulting movement of the colloidal particle happens on time scales $\geq 10^{-9}$ s. The velocity of the colloidal particle is $\vec{v} = \vec{p}/M$ where $\vec{p}$ is the momentum and M the mass of the particle. This directional movement of the colloidal particle leads to systematic collisions with the solvent molecules that can be approximated as a hydrodynamic friction force because of the size difference between solvent molecules and the much larger colloidal particles [68]. For the small velocities encountered in colloidal systems, this friction force is directly proportional to the velocity of the particle $f_f(t) = -\kappa\vec{p}(t)/M$ with the proportionality constant [68]

$$\kappa = 6\pi\eta_0 R_p. \tag{2.34}$$

Here, η_0 is the shear viscosity of the solvent, and R_p is the radius of the colloidal particle. With this, the equation of motion of the colloidal particle becomes [68]

$$\frac{\mathrm{d}\vec{p}}{\mathrm{d}t} = -\kappa\vec{p}/M + \vec{f}(t). \tag{2.35}$$

This kind of equation of motion with a fluctuating force is called Langevin equation [212]. Due to the random nature of $\vec{f}(t)$, it makes no sense to solve the above equation for a single colloidal particle. However, making use of the separation of time scales between solvent molecules and colloidal particles and the random orientation of the collision force, we can derive properties averaged over all colloidal particles like the mean square displacement $\langle[\vec{r}(0) - \vec{r}(t)]^2\rangle$.

For times scales $\gg M/\kappa$, the mean square displacement is proportional to the observation time [18, 68]:

$$\langle[\vec{r}(0) - \vec{r}(t)]^2\rangle = 6D_0 t. \tag{2.36}$$

D_0 is the diffusion coefficient that is related to the temperature T and the viscosity of the continuous medium η via the Stokes-Einstein relation [213]

$$D_0 = \frac{k_B T}{6\pi\eta R_p} \tag{2.37}$$

where R_p is the radius of the particle and k_B the Boltzmann constant. The diffusion coefficient is related to the decorrelation rate of the $g^{(2)}$ correlation function (Eq. 2.32) via

$$\Gamma = D_0 q^2 \tag{2.38}$$

The distribution of the relaxation times is reflected in the KWW exponent that is $k = 1$ for most diffusive systems [214], such that the $g^{(2)}$ function takes the form

$$g^{(2)}(q,\tau) = 1 + \beta \exp\left(-2D_0 q^2 \tau\right). \tag{2.39}$$

for diffusive systems.

2.2.4.2 Stress relaxations

The dynamics observed in jammed systems like gels or glasses differ from the abovementioned diffusive motion. These jammed systems are trapped in a state far from equilibrium, and the relaxation towards equilibrium happens on long time scales beyond experimental times. In some cases, a two-step decay is observed where the first decay represents the locally confined, diffusive motion of the gel or glass constituents [65, 215, 216]. The decorrelation rates of the dominant, slow decay observed in gel and glass systems are proportional to the momentum transfer $\Gamma \propto q$ [27, 29, 215–220] while in diffusive systems $\Gamma \propto q^2$ holds (Eq. (2.38)). Therefore, the origin of the gel dynamics must be other than diffusive. At the same time, the decay of the correlation function in these glass or gel systems is steeper than exponential with KWW exponents of $k \approx 3/2$ at low q. This excludes that thermally activated formation or breaking of bonds is the driver for the

dynamics as these rare and uncorrelated events would lead to a simple exponential decay with $k = 1$ [215]. Another common feature in the dynamics of gels and glasses is a slow-down of the dynamics as a function of waiting time, which is referred to as aging [221–223].

Here, we will briefly discuss the foundations of two related models that aim to explain the anomalous dynamics observed in gels. The first model was published by Cipelletti et al. [215, 216] who locate the origin of the dynamics in the shrinking of the gel (syneresis). This shrinking might be induced by van der Waals forces reducing the inter-particle distance of the gel constituents locally [215]. This shrinking is not isotropic because of the adhesion of the gel to the walls of the sample environment, in our case, quartz capillaries. Instead, randomly distributed regions arise where the sample is deformed due to local shrinking events that induce stress [215]. Because of the elasticity, these deformations also affect the surroundings or the origin of the stress, which can be expressed as a displacement field ΔR. If ΔR is expressed in powers of $1/r$, the leading term is of the order $1/r^2$ as the $1/r$ term corresponds to a point-like external source that is not present in the system [216]. A general expression for the leading term of the displacement field takes the form [216]:

$$\Delta R(t) = A(t)r^{-2}. \tag{2.40}$$

Close to the origin of the stress, the exponent might deviate from -2 due to higher multipole contributions [216]. Equation (2.40) can be rewritten using the cluster size of the gel R_c and the strain field $e(t)$ as [215]:

$$\Delta R(t) \propto e(t)R_c^3 r^{-2}. \tag{2.41}$$

In the final step, Cipelletti et al. [215] derive the functional form of the correlation function by calculating the probability that a particle is not displaced more than q^{-1} and thus contribute to the correlation function. They find that the minimum distance from a stress source for this contribution is:

$$r_{\min} = \sqrt{e(t)qR_c^3}. \tag{2.42}$$

Together with the assumption that the stress sources are randomly distributed and that $e(t)$ is a linear function of time on intermediate time scales, the correlation takes the expected functional form $\propto \exp(-2(\Gamma t)^{3/2})$ and Γ has a ballistic nature ($\Gamma \propto q$) The aging behavior can be included into this model by a more complex functional form of $e(t)$ on longer time scales[216].

These arguments were substantiated by computations of Bouchaud and Pitard [224] on randomly distributed stress dipoles in an elastic medium. In addition to the regime where the structure factor scales with $k = 3/2$, they identify two regimes as the sample ages: one where the KWW exponent is lowered to $k = 5/4$ and one regime where the $\Gamma \propto q$ scaling does not hold anymore. With this, the exponential growth of $1/\Gamma$ and the subsequent saturation in an aging glass can be explained, but it turned out to be challenging to match the different regimes

to experimental time windows [224].

The model of randomly distributed stress dipoles is grounded on the assumption that the scaling with $k = 3/2$ holds across the whole range of momentum transfers q, which was observed in the q range accessed with dynamic light scattering experiments at that time. Dynamic light scattering is the counterpart of XPCS using laser light. Duri and Cipelletti [65] extended the q range towards higher q ($q = 5.5\,\mu\mathrm{m}^{-1}$) and observed that towards higher q, the KWW exponent decreases from $k = 3/2$ to $k = 1$. The same behavior was observed in an early XPCS experiment with a q range up to $90\,\mu\mathrm{m}^{-1}$. This cannot be explained within the model introduced above, so it was modified in the spirit of a continuous random walk model [225–227].

In this model, the continuous ballistic motion is replaced by a series of instantaneous discrete displacement events that have the same amplitude [65]. We need to find an expression for the degree of decorrelation that every step introduces. We call this function h and expect it to depend on the momentum transfer q, the age of the sample t_w and the time parameter τ of the correlation function [65]. Both time parameters act on the degree of decorrelation h through the number of events n that occur between t_w and $t_\mathrm{w} + \tau$ such that we obtain $h[q, n(t_\mathrm{w}, \tau)]$. With this, we can express the intermediate scattering function $f(q, \tau) = \sqrt{(g^{(2)} - 1)/\beta}$ as [65]

$$f(q, \tau) = \sum_{n=0}^{\infty} P_\tau(n) h(q, n). \tag{2.43}$$

The amplitude $P_\tau(n)$ is the probability that n events occur in the scattering volume during the time τ. For the computation of the $g^{(2)}$ function, we need to find expressions for P_τ and h. We assume that the displacement events are independent of each other such that the easiest form for P_τ is a Poisson distribution:

$$P_\tau(n) = \exp(-\gamma\tau)(\gamma\tau)^n/n!. \tag{2.44}$$

Here, γ is the rate of the relaxation events such that $1/\gamma$ is the mean time between two events [228].

For the expression of h, we recall the displacement field $\Delta\vec{R}$ introduced in the first model in Eq. (2.40). With this, the degree of decorrelation can be expressed as [65, 229]

$$h(q, N) = \langle \exp(-in^\alpha \vec{q} \cdot \Delta\vec{R}) \rangle \tag{2.45}$$

where $\langle \cdots \rangle$ denotes the average over all particles and all directions of $\vec{q}$. The exponent α needs to be adapted to the nature of the particle's motion [65, 228]. The case $\alpha = 1$ represents ballistic motion, where all N displacements are oriented in the same direction. With this, we can express

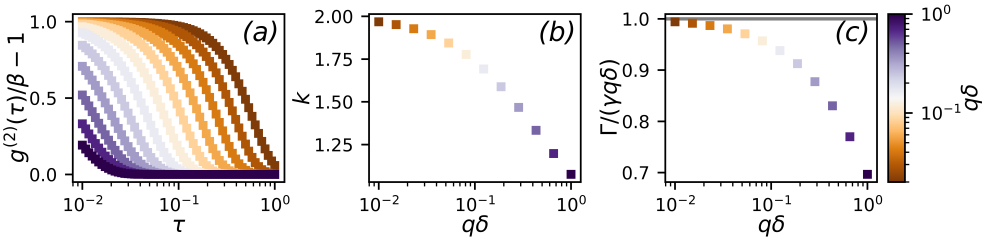

Figure 2.9: Calculated $g^{(2)}$ functions according to the random walk model for stress relaxations. Here, we modeled $N = 200$ relaxation events with a rate $\gamma = 120$. (a) $g^{(2)}$ functions for twelve values of $q\delta$ indicated by the different colors. Solid lines are fits with KWW functions (Eq. (2.32)). (b) Fit results for KWW exponents k. (c) Fit results for decorrelation rate Γ normalized to the rate of relaxation events γ and $q\delta$.

h in terms of the probability distribution function (PDF) of the particle displacements [65, 229]:

$$h(n,q) = \int \mathrm{PDF}(\Delta\vec{R}) \exp\left(in\vec{q}\cdot\Delta\vec{R}\right). \tag{2.46}$$

Recalling the assumption from the first model that the displacements are caused by local rearrangements of the gel that cause dipolar stresses, the expression for h becomes [65]:

$$h(q,n) \approx \exp(-(qn\delta)^{\zeta}), \tag{2.47}$$

where δ is the average displacement of a single relaxation and the parameter ζ can be adapted to get the right decay of the PDF. Caronna et al. used a simple Gaussian distribution for $\Delta\vec{R}$ and obtain the $\zeta = 2$ case of Eq. (2.47) [228]

$$h(q,n) \approx \exp(-(qn\delta)^2). \tag{2.48}$$

For our computation we will use this expression for $h(q,n)$ such that the correlation function becomes:

$$g^{(2)}(q,\tau) = 1 + \beta\left(\sum_{n=0}^{N} \frac{\exp(-\gamma\tau)(\gamma\tau)^n}{n!} \exp(-(qn\delta)^2)\right)^2. \tag{2.49}$$

In Fig. 2.9 we compute Eq. (2.49) for twelve values of $q\delta$ between 0.01 and 1. We assume $N = 200$ consecutive relaxation events occurring with a rate $\gamma = 120\,\mathrm{s}^{-1}$. The resulting correlation functions are fitted with a KWW function (Eq. 2.32). Fig. 2.9(b,c) shows the results for the fit parameters Γ and k, which will be used later in the interpretation of the fit results of the egg white. It can be seen that in this random walk model for stress relaxations, the $g^{(2)}$ function agrees with a compressed exponential form $k > 1$ as expected.

2.3 Radiation effects

X-rays can also interact with matter in ways other than elastic scattering, potentially altering the sample's structure and/or dynamics. These additional interactions are the photoelectric effect, Compton scattering, pair production, and photodisintegration [230], and their relevance depends on the energy of the scattered X-rays and the absorbing material. In the case of water and X-ray energies of $\approx 10\,\mathrm{keV}$, the dominant processes besides elastic scattering are the photoelectric effect and Compton scattering.

The photoelectric effect is the dominant process at low X-ray energies. The X-ray photon gets absorbed by one of the bound electrons in the material, leading to an ejection of this electron. The photon energy is used to overcome the binding energy, and the rest is converted into kinetic energy of the now free electron. The atom is left with an excited hole in the shell where the electron was before, and this excitation is released via a combination of characteristic X-ray radiation and Auger electrons [231]. In the end, the absorption of a single photon often leads to the emission of two or more electrons. The cross-section of the photoelectric effects increases dramatically as soon as the photon energy exceeds the binding energy of a specific shell of the atom, resulting in sharp material-specific absorption edges (e.g. [230]).

With increasing X-ray energy, the probability of incoherent or Compton scattering increases. Here, the X-ray photon transfers some of its energy to one of the loosely bound electrons in the outer shell and gets scattered at an angle Θ [232]. Due to the energy loss, the wavelength of the X-ray photon is increased by an amount $\Delta\lambda = \lambda_c(1 - \cos\Theta)$, where $\lambda_C = 0.0024\,\mathrm{nm}$ is the Compton wavelength [233]. The electron is ejected as well.

To quantify the amount of X-ray photons that interact with a material of thickness z, we use the Lambert-Beer law [234, 235]:

$$I(z) = I_0 e^{-\mu z}, \tag{2.50}$$

where μ is the attenuation coefficient. As the attenuation depends strongly on the density of the medium, the mass attenuation coefficient, which is the attenuation coefficient divided by the density ρ, is the more fundamental quantity [230]. Figure 2.10 shows the mass attenuation coefficients for photoelectric effect/absorption, elastic, and Compton scattering. Our experiments were performed with a photon energy of $8.54\,\mathrm{keV}$, where the photoelectric effect is the dominant process.

The relevant quantities for further consideration are the amount of energy that is deposited per sample mass, the dose $\mathcal{D}$, and the rate of that energy deposition, the dose rate $\dot{\mathcal{D}}$ that are linear functions of the incident photon flux $\mathcal{F}$.

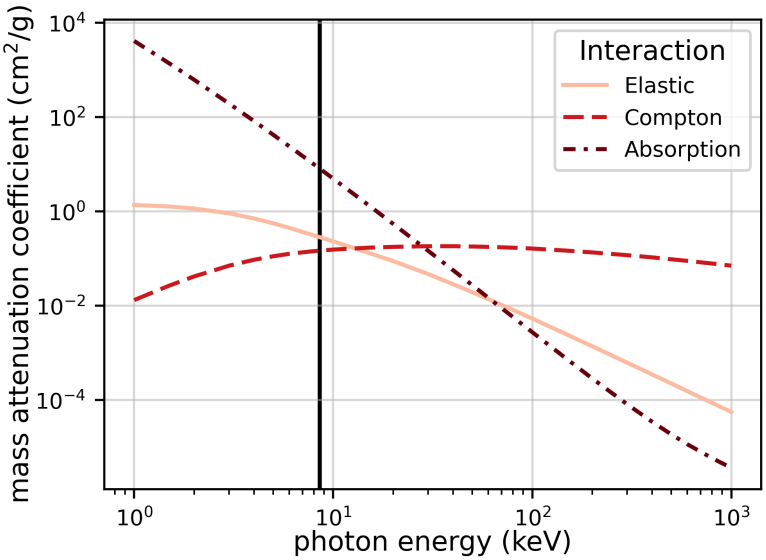

Figure 2.10: Mass attenuation coefficients in water for the three dominant processes of X-ray matter interactions at photon energies between 1 keV and 1 MeV. The vertical line indicates the energy of 8.54 keV at which the experiment was conducted. The mass attenuation coefficient for absorption does not display any discontinuities in this energy range as the K-shell binding energy is at ≈ 0.5 keV [230]. Data taken from [236].

2.3.1 Flux and Fluence

The amount of radiation effects is strongly dependent on the amount of X-ray photons that are used for illumination. These can be expressed in terms of the photon flux $\mathcal{F}$ or the photon fluence Φ. The photon flux $\mathcal{F}$ is the number of photons N_{ph} that impinge on the sample per time interval t and is given in units of photons per second:

$$\mathcal{F} = \frac{N_{\mathrm{ph}}}{t}. \tag{2.51}$$

A typical photon flux at a coherence beamline of a third-generation synchrotron is of the order of $10^{10}\,\mathrm{ph\,s^{-1}}$. The photons are collimated into a beam that illuminates an area A on the sample. To compare radiation effects among different experiments with different beam sizes, it makes sense to express results in terms of the photon fluence, which is the photon flux normalized to the area A of the beam:

$$\Phi = \frac{\mathcal{F}}{A}. \tag{2.52}$$

In experiments, the photon fluence is usually not homogeneous over the illuminated area but follows a Gaussian beam profile [60]. The photon fluence on the sample can be reduced by inserting material between the X-ray source and sample such that the number of photons is reduced according to the Lamber-Beer law (Eq. 2.50).

2.3.2 X-ray Dose

The X-ray dose is the amount of energy E that is transferred from the X-ray photons to a sample of mass m,

$$\mathcal{D} = \frac{E}{m}, \tag{2.53}$$

and has units of Gray ($1\,\mathrm{Gy}{=}1\,\mathrm{J\,kg^{-1}}$). In an X-ray scattering experiment, the dose after an exposure of t_{exp} of the sample to a photon flux $\mathcal{F}$ is given by [237]:

$$\mathcal{D} = \frac{t_{\mathrm{exp}}\mathcal{F}E(1-T)}{V\rho} = \frac{t_{\mathrm{exp}}\Phi E(1-T)}{z\rho}, \tag{2.54}$$

where E is the photon energy and $V = A \times z$ is the illuminated sample volume. A is the area of the X-ray beam which is $100\,\mu\mathrm{m} \times 100\,\mu\mathrm{m}$ in our experiment and z is the thickness of the sample which is $\approx 1.5\,\mathrm{mm}$. Because of the high water content of the egg white, we will approximate the X-ray absorption of egg white with that of water. T is the transmission, that is $T = 0.28\,\%$ for 1.5 mm of water and 8.54 keV X-rays. As sample density ρ we use the density of water $\rho = 1000\,\mathrm{kg\,m^{-3}}$.

2.3.3 X-ray Dose Rate

Besides the total amount of energy deposited in the sample volume, the rate of energy deposition might also be decisive for minimizing the effects of X-ray radiation on the sample. This is described by the dose rate $\mathscr{D}$ that is the dose $\mathcal{D}$ divided by the exposure time t_{exp}:

$$\mathscr{D} = \frac{\mathcal{F}E(1-T)}{V\rho} = \frac{\Phi E(1-T)}{z\rho} = \frac{\mathcal{D}}{t_{\mathrm{exp}}}. \tag{2.55}$$

The unit of the dose rate is $\mathrm{Gy\,s^{-1}}$.

2.3.4 Radiolysis and Radicals

As water is the largest fraction in egg white samples, the decomposition of water molecules due to ionizing radiation (radiolysis) is important for understanding beam effects on egg white. Radiolysis encompasses a variety of processes that take place on different time scales [238]. The starting point is the ionization and excitation of an atom as described in Sec. 2.3, which happens on the femtosecond scale. During the relaxation of these excited states, charged particles with high velocities are generated (fs to ps). The reactions of these particles are divided into two groups: non-homogeneous and homogeneous reactions [239–242]. In the non-homogeneous case that sets in earlier ($\approx$ ps), the reactions of the particles are clustered around the track of the initial particle and build so-called "spurs". The homogeneous reactions are those initialized by particles that diffuse away from the spur, which is observed between 10^{-10} and 10^{-6} s.

To account for the non-homogeneity of the radiolysis reaction, the linear energy transfer (LET) for ionizing particles was introduced, which is the energy deposited per path length $-\mathrm{d}E/\mathrm{d}x$. One can distinguish low-LET radiation like γ-rays and X-rays that distribute their energies along long spurs from high-LET radiation (α particles, heavy ions) with LET values in the range $1\,\mathrm{MeV\,mm^{-1}}$ to $100\,\mathrm{MeV\,mm^{-1}}$ [243, 244]. The latter confine their effects to small regions where a high amount of energy is deposited.

During these radiolysis processes, electrons with an energy of $\leq 100\,\mathrm{eV}$ play a key role. This is due to the oscillator strength distribution of the valence electrons that peaks around 30 eV and practically vanishes above 100 eV [238]. Accordingly, the "G value" was defined as the yield of radiochemical species per 100 eV of absorbed energy. Theoretical predictions of these yields are somewhat difficult as the first-order Born approximation does not hold at these low electron energies [245]. But some Monte Carlo simulations [246, 247] predict rates for the different radiochemical species as discussed below.

The species that are generated in the radiolysis of water can be summarized as [248]:

$$\mathrm{H_2O} \overset{\text{ionizing radiation}}{\rightarrow} \mathrm{e^-_{aq}}, \mathrm{HO\bullet}, \mathrm{H\bullet}, \mathrm{HO_2\bullet}, \mathrm{H_3O^+}, \mathrm{OH^-}, \mathrm{H_2O_2}, \mathrm{H_2}. \tag{2.56}$$

More details on the reactions involved can be found in the review of Garrett et al. [238].

In the equation above, the dot • represents an unpaired electron [249], which makes the respective species exceptionally reactive. These highly reactive species are also referred to as radicals [249]. For low-LET radiation like X-ray photons, the yield of the molecular products H_2O_2 and H_2 significantly beyond the microsecond timescale as they tend to recombine with the radicals into water another radical via the reactions [248, 250, 251]:

$$\mathrm{HO}\bullet + \mathrm{H_2} \rightarrow \mathrm{H_2O} + \mathrm{H}\bullet, \tag{2.57}$$

$$\mathrm{H}\bullet + \mathrm{H_2O_2} \rightarrow \mathrm{H_2O} + \mathrm{HO}\bullet. \tag{2.58}$$

We will focus our consideration on the yield of the highly reactive HO• hydroxyl radicals on the timescale beyond microseconds as they are most likely to diffuse to the proteins of the egg white and change their structure and/or dynamics. For 8.54 keV the Monte Carlo simulations give hydroxyl yields of ≈ 2 radicals per 100 eV on the microsecond time scale [246, 247]. With these numbers, we will later derive estimations on radical densities necessary to induce radiation-driven dynamics in the different egg white sample systems (Sec. 7.2).

2.3.5 Radiation Effects on Proteins

This section reviews findings on X-ray radiation effects on proteins in aqueous solutions and protein crystals. This might help to understand the effects on proteins in a gel network, where a considerable amount of water is bound in the mesh-like structure. In the water content of the samples, the irradiation with X-rays leads to the generation of free radicals as described in Sec. 2.3.4. These radicals diffuse through the sample and attach to the backbones or the side chains of the proteins [252]. These radical-activated proteins are likely to form aggregates with other activated proteins through covalent or non-covalent bonds [253]. These processes can be tracked with the fluorescent biomarker tyrosine that indicates oxidative stress to proteins as it is induced by radiation [254]. An increased level of dityrosine is also associated with various diseases such as eye cataracts, Alzheimer's, or Parkinson's disease [255, 256].

The investigation of a highly crowded protein solution of α-crystallin revealed that the dynamics of the proteins on the molecular scale are accelerated with increasing dose rate, while dose can both, accelerate and slow-down the dynamics depending on how close the sample is to a glass transition [60]. This behavior is explained via the formation of covalent links between the protein radicals, that cause displacements to other proteins due to the dense packing of the proteins.

In a crystal environment, structural changes to the proteins itself are observed. These are the breaking of disulfide bonds and increasing B factors and unit cell volumes [257].

Chapter 3

Experimental Realization

This chapter presents details on the experiments, starting with a general description of the P10 coherence applications beamline in Sec. 3.1. Details on the configuration used for our experiments are given in Sec. 3.2 followed by details on the preparation of the egg white samples in Sec. 3.3. In Sec. 3.4, the signal-to-noise ratio (SNR) is introduced as a measure for the feasibility of an X-ray photon correlation spectroscopy experiment. This is the basis for the different measurement schemes described in Sec. 3.5.

3.1 P10 Coherence Applications Beamline

The USAXS-XPCS experiments were conducted at the P10 Coherence Applications Beamline at the PETRA III storage ring at Deutsches Elektronen-Synchrotron (DESY) in Hamburg. Figure 3.1 summarizes the main technical components explained in the following. This section is based on the P10 Coherence Beamline User Guide [258].

The source of X-rays for the P10 beamline is a 5 m long U29 undulator that provides X-ray radiation with a brilliance of [259]:

$$\mathcal{B} = 4 \times 10^{20}\,\mathrm{s}^{-1}\,\mathrm{mm}^{-2}\,\mathrm{mrad}^{-2}\,(0.1\%\mathrm{BW})^{-1}. \tag{3.1}$$

The beam is shaped using two sets of slits (PS1 and PS2 in Fig. 3.1). In the optical hutch (OH), the bandwidth of the beam is reduced in the standard PETRA III high heat load monochromator. In the next step, the beam is reflected horizontally by two flat X-ray mirrors (M1, M2), which suppresses the higher harmonics generated in the undulator. In the first experimental hutch (EH1), the beam is focused on the sample using compound refractive lenses (CRL). An X-ray shutter with a minimum closing time of 0.1 s can be used to adapt the sample's illumination and

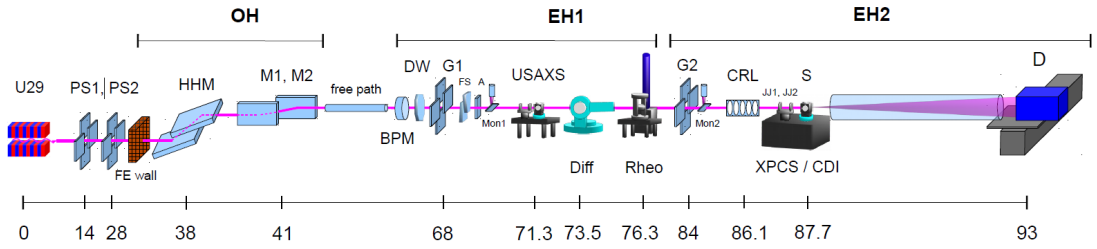

Figure 3.1: Layout of the P10 Coherence Applications Beamline at the PETRA III storage ring. The beam is prepared in the optics hutch (OH) before passing through the first and second experimental hutch (EH1, EH2). The components that are most relevant for our USAXS-XPCS experiment are the undulator (U29), power slits (PS1, PS2), a high heat load monochromator (HHM), two mirrors (M1, M2), guard slits (G1, G2), the sample stage that is placed in the EH1, and the detector (D) at the end of the beamline in EH2. (Figure taken from [258])

reduce the dose.

Figure 3.2 shows a photo of the experimental setup in the EH1. The incident beam approaches the sample from the right side of the photo. The capillaries with the samples are placed in a Linkam stage that enables temperature control, which was not used to measure radiation effects. The Linkam is enclosed by a box with a constant nitrogen flow that prevents condensation on the Linkam stage during cooling. Behind the sample stage, the scattered beam is guided into the EH2, where the detector is placed.

3.2 Experimental Setup

The experiment was realized in the ultra-small angle X-ray scattering (USAXS) geometry where the sample is placed in the EH1, and the detector is placed 21.2 m downstream in the EH2. The two-dimensional detector is an EIGER X 4M with a pixel size of 75 µm × 75 µm and 2070 × 2167 pixels in total. With this setup, the accessible range in momentum transfer at a photon energy of 8.54 keV is $q \in [0.006, 0.02]\text{nm}^{-1}$ where the limits are determined by the diameter of the flight tube between EH1 and EH2 and the size of the beam stop that is inserted to block the direct beam. Figure 3.3 shows a section of a typical scattering pattern recorded by the detector.

The EIGER X 4M detector can be operated at 750 Hz [260] which corresponds to a minimum exposure time of $t_{\text{exp}} \approx 0.0014\,\text{s}$. The readout of the data takes a few microseconds, such that it is negligible compared to the exposure time. The X-ray shutter that is controlled by the detector allows for added delay times without X-ray exposure of 0.1 s and higher, but this option is not used in our experiment. The number of frames recorded in one series is limited by the internal storage of the detector and should be kept below ≈ 8000 frames. Longer exposures can be realized

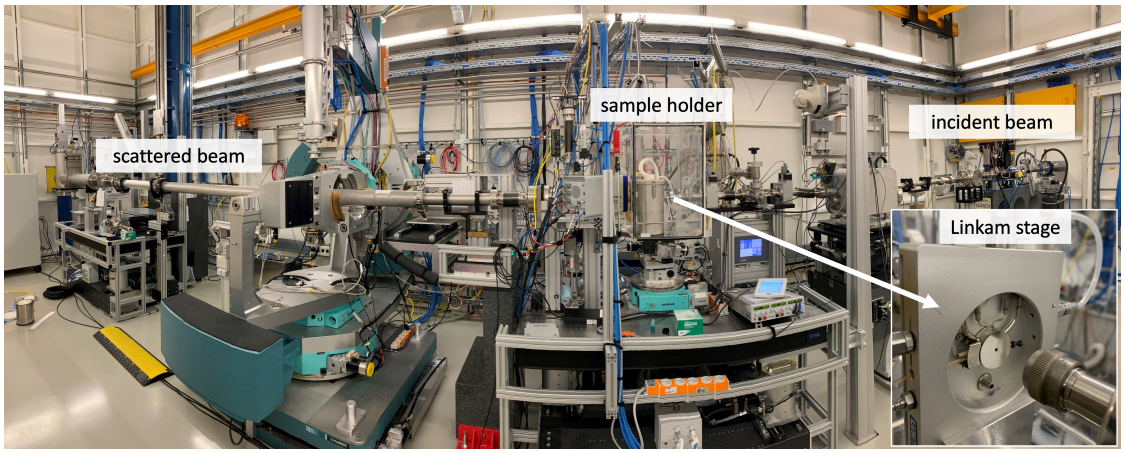

Figure 3.2: Picture of the experimental setup in the first hutch (EH1) where the samples are placed. The sample holder is a Linkam temperature control stage placed in a box with constant nitrogen flow.

by taking more than one series on the same sample spot. Between two series, there is a dead time of up to eleven seconds for file storage [261].

The sample thickness must be balanced between high absorption of X-rays in very thick samples and a low probed volume in very thin samples. The optimum sample thickness was found to be such that the transmission T of the sample is the inverse of Euler's number [262]:

$$T = \frac{I_{\text{transm.}}}{I_{\text{inc.}}} = e^{-1} \approx 0.35. \tag{3.2}$$

The transmission and the optimal sample thickness depend on the atomic scattering factor and, thereby, on the photon energy (Eq. 2.12). Assuming that the egg white's absorption is comparable to that of water, the optimal sample thickness would be 1.3 mm for 8.54 keV X-rays [263]. Our samples were filled in quartz capillaries with diameters between 1.4 mm to 1.5 mm, which is close to the optimal sample thickness and fits the hole of the Linkam stage sample holder.

The size of the X-ray beam on the sample was set to $A_{\text{beam}} = 100\,\mu\text{m} \times 100\,\mu\text{m}$ as this large beam size reduces the energy that is absorbed per sample volume and, thereby, the dose rate $\mathscr{D}$. Together with the sample thickness of $z_{\text{sample}} \approx 1.5\,\text{mm}$ the irradiated Volume V_{irr} becomes

$$V_{\text{irr}} = A_{\text{beam}} \times z_{\text{sample}} = 100\,\mu\text{m} \times 100\,\mu\text{m} \times 1.5\,\text{mm} \tag{3.3}$$

We neglect absorption in the capillary walls and assume a flat beam profile. The highest available

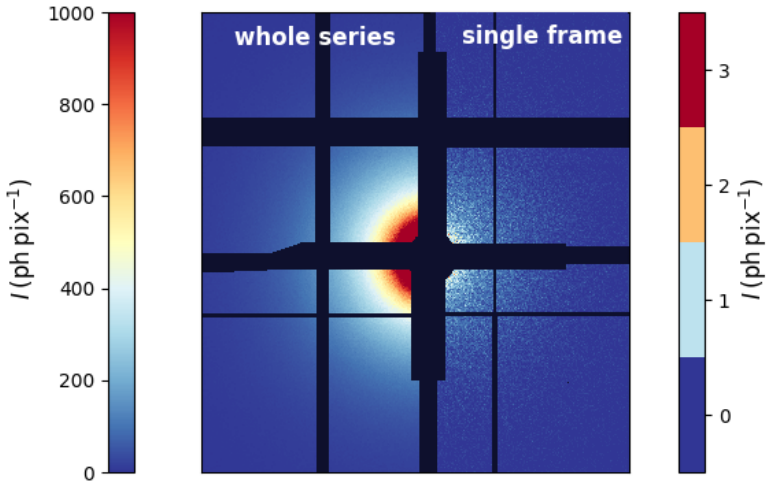

Figure 3.3: Typical scattering pattern from cooked egg white on the EIGER X 4M detector. The right half shows the intensity from a single frame, and in the left half, the intensity is integrated over the whole series (200 s).

flux on the sample in our setup is

$$\mathcal{F}_0 = 6 \times 10^{10}\ \mathrm{ph\,s^{-1}}. \tag{3.4}$$

It can be reduced by inserting a number of silicon wafers with a thickness of 25 µm before the sample. At a photon energy of 8.54 keV, each silicon wafer attenuates 26.7 % of the flux such that the reduced fluence after n absorbers is

$$\mathcal{F}_{\mathrm{red}}(n) = \mathcal{F}_0 \times (1 - 0.267)^n. \tag{3.5}$$

Dividing the X-ray flux by the irradiated area A_{beam} gives the X-ray fluence Φ (Eq. 2.52). At the P10 beamline, only certain combinations of silicon wafers n are allowed. Table 3.1 lists the first ten values for n with the corresponding fluxes and fluences. The dose rate given in the fourth column is calculated using Eq. (2.55) with the transmission and density of water.

3.3 Sample Preparation

We purchased organic hen eggs for the egg white sample preparation at a local supermarket. Due to the time that passes between the laying of the egg and the arrival at the supermarket, we expect a significant fraction ($\geq 50\,\%$) of the ovalbumin protein component to be present in the

Table 3.1: Reduced fluxes and fluences for different absorber configurations and resulting dose rate on a water equivalent sample. n - number of 25 µm Si wafers inserted to attenuate the beam; $\mathcal{F}_{\text{red.}}$ - incident flux; $\Phi_{\text{red.}}$ - fluence on sample; $\mathscr{D}$ - dose rate. Fluence and dose rates are rounded to one significant digit in the text.

n	$\mathcal{F}_{\text{red.}}(\text{ph s}^{-1})$	$\Phi_{\text{red.}}(\text{ph s}^{-1}\,\text{nm}^{-2})$	$\mathscr{D}(\text{kGy s}^{-1})$
0	6×10^{10}	6	4
1	4.4×10^{10}	4.4	2.9
2	3.2×10^{10}	3.2	2.1
4	1.7×10^{10}	1.7	1.1
6	9×10^{9}	0.9	0.6
8	5×10^{9}	0.5	0.3
12	1.4×10^{9}	0.14	0.09
16	4×10^{8}	0.04	0.03
18	2×10^{8}	0.02	0.01
24	3×10^{7}	0.003	0.002

more heat-stable S-ovalbumin form at that time [264].

The sample preparation was done in the P10 preparation laboratory. All samples within one set of measurements were prepared from the same hen egg. To access the egg white, the egg shell is cracked, and the egg white and egg yolk are put into a Petri dish. If the egg yolk is damaged during this transfer, it must be repeated with a different egg to avoid mixing the yolk and white components. Egg white consists of two fractions, the thin and the thick egg white, with different levels of ovomucin. This causes the gelling properties of thin and thick egg white to be different [265]. In this study, we focus on the gelling of the thin egg white, which is separated from the thick component and the egg yolk, using a pipette with a 10 mL tip.

For the first data set, the egg white was prepared with 50 mmol of sodium chloride (NaCl, ordered at Merck, Germany). The basis is a stock solution of purified Milli-Q water with 2 mol NaCl from which a small amount is mixed with the egg white to achieve the desired concentration of 50 mmol. The egg whites that are used for measuring data sets two and three are prepared without adding NaCl.

All egg white solutions are filled into quartz capillaries with a diameters of 1.4 mm to 1.5 mm (WJM-Glas Müller, Germany). The transfer from the beaker into the capillaries is done using long syringe needles with a diameter of 0.8 mm that are attached to 1 mL syringes. Tiny air bubbles emerging in this procedure are removed by shaking the capillary manually. Afterward, the capillaries are sealed with parafilm and kept in the fridge at 5 °C.

Before cooking, the capillaries with the samples are left at room temperature for about 30 min. The samples for dataset one are cooked with a temperature-controlled Linkam stage installed at the beamline, while the samples for datasets two and three are cooked in a water bath in the

preparation laboratory. The heating rate of the Linkam stage is set to $150\,\mathrm{K\,min^{-1}}$ and the capillaries are heated for $\approx 40\,\mathrm{min}$ followed by cooling to $22\,^{\circ}\mathrm{C}$ with the same rate. After 12 min at $22\,^{\circ}\mathrm{C}$, the measurements on radiation effects are started with the sample in the Linkam stage. For datasets two and three, the samples are cooked in a water bath in the preparation laboratory to use the measurement time more efficiently. Figure. 3.4 shows the cooking setup. The water is stirred with a magnetic stirrer at 200 rpm and the temperature of the water bath is cross-checked with an external thermometer that gave a deviation of $\approx 1\,^{\circ}\mathrm{C}$ towards lower temperatures. The capillary is held by a pair of tweezers such that the angle between the surface of the water and the capillary is $\approx 30^{\circ}$ to 40° (Fig. 3.4(a,c)). We found that this is the best compromise between cooking the capillary horizontally, where lots of air bubbles are forming along the upper edge, and cooking the capillary vertically, where the observed dynamics depend on the position of the spot on the capillary where the measurement is performed. This might be due to gravitational effects on heavier gel parts. The top part of the capillary that is sealed with Parafilm is kept above the surface of the water (Fig. 3.4(c)). The cooking time in the water bath is 40 min as well, but in contrast to the Linkam setup, the capillaries are left at room temperature for about one hour before being measured. For experimental reasons, the sample environment during the measurement was a Linkam stage as well, but the temperature control was turned off to avoid vibrations on the sample.

The cooking duration of 40 min was chosen to facilitate the comparison of earlier work on XPCS with egg white by Begam et al. [54, 55] and turned out to match the cooking duration for microscopy on cooked egg white performed by Bonilla et al. [184]. If the cooking temperature exceeds the denaturation temperature of a protein component, the fraction of denaturated proteins increases with time and with temperature. The last protein that denaturates in the egg white is (S-)ovalbumin, which starts to denaturate around $70\,^{\circ}\mathrm{C}$. The plot in Ref. [266] shows that after 40 min at $80\,^{\circ}\mathrm{C}$, almost the whole ovalbumin content is expected to be denaturated. All cooking environments and temperatures for the different data sets are summarized in table 3.2.

Table 3.2: Overview on sample preparation for different beamtimes/data sets.

data set	beamtime ID	cooking environment	NaCl	temperatures (°C)
1	II-20210008	Linkam stage	50 mmol	70,75,78,80
2	I-20211600	water bath	0 mmol	60,65,68,70,73,75,78
3	I-20210097	water bath	0 mmol	50-85

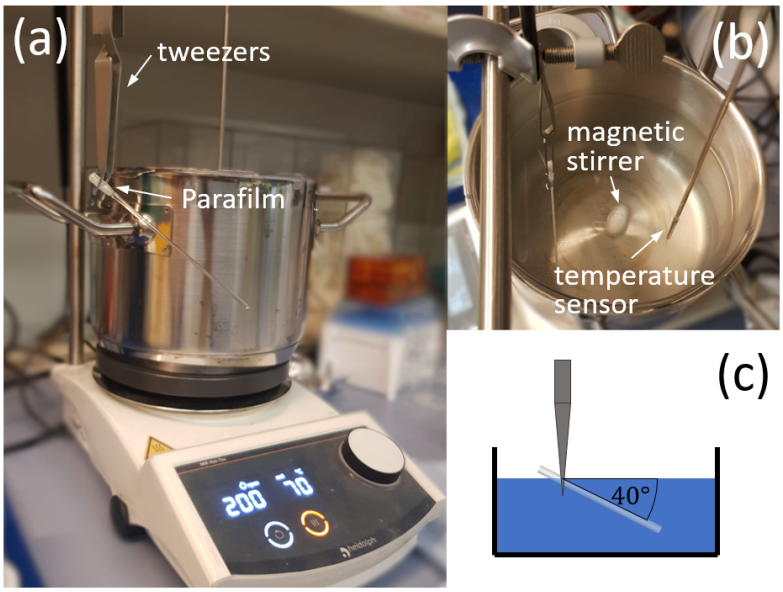

Figure 3.4: Setup for cooking egg white samples in the water bath. (a) Side view with a capillary in front of the heating stage. (b) Top view with a magnetic stirrer and temperature sensor. (c) Sketch of a side view: the top part sealed with Parafilm is above the surface of the water.

3.4 Feasibility of XPCS Experiments

The feasibility of an XPCS experiment can be determined by calculating the signal-to-noise ratio (SNR) that is given by [19, 26, 267]:

$$R_{\mathrm{SN}} = \beta \times I_{\mathrm{pix}} \times \sqrt{N_{\mathrm{pix}} \times N_{\mathrm{fr}} \times N_{\mathrm{rep}}}. \tag{3.6}$$

and thus depends on the speckle contrast β, the intensity per pixel I_{pix}, the number of pixels N_{pix}, frames N_{fr} and repetitions N_{rep}.

The speckle contrast β contains information on the coherence of the beam and how the size of the speckles matches the size of the detector pixels [19]. β depends on the the momentum transfer q and can be determined by measuring XPCS on a static sample. We used an Aerogel sample which gave contrasts of 10.6 % at $q = 0.006\,\mathrm{nm}^{-1}$ and 9.7 % at $q = 0.02\,\mathrm{nm}^{-1}$.

I_{pix} is the mean intensity per pixel per frame in units of photons. For samples that are not scattering many photons, I_{pix} can be increased by increasing the exposure time t_{exp} per frame on the cost of temporal resolution of the measurement. The upper limit for I_{pix} is given by the count rate of the detector that is $5 \times 10^8\,\mathrm{ph\,s^{-1}\,mm^{-2}}$ for the EIGER X 4M [268].

N_{pix} denotes the number of detector pixels per q-region of interest (ROI). In our analysis

setup, we define twelve ROIs as concentric annuli around the beam stop from $q = 0.006\,\mathrm{nm}^{-1}$ to $q = 0.08\,\mathrm{nm}^{-1}$. The first five rings have a width of $0.002\,\mathrm{nm}^{-1}$ while the rings at larger q have a width of $0.006\,\mathrm{nm}^{-1}$ to compensate for the lower photon count rates at high q. Accordingly, the number of pixels increases from $N_{\mathrm{pix}} \approx 400$ at $q = 0.006\,\mathrm{nm}^{-1}$ to $N_{\mathrm{pix}} \approx 100000$ at $q = 0.03\,\mathrm{nm}^{-1}$

N_{fr} is the number of frames within one series from which the intensities are correlated. In our experiment, this is limited by the memory of the detector. Therefore, keeping N_{fr} below 8000 is recommended. A high number of frames also increases the time for calculating correlation functions.

Moving the direct beam by twice the beam size after each irradiation is a common practice to avoid radiation effects on neighboring spots. Together with our large beam of $100\,\mu\mathrm{m} \times 100\,\mu\mathrm{m}$ the number of measurement spots on the capillary is limited. This also restricts the number of repetitions of each measurement N_{rep}, which is why we perform only a single measurement per temperature and fluence.

3.5 Measurement Protocols

This section introduces the different measurement protocols that were used in the three experiments.

3.5.1 Standard Measurement

In all three beam times, we performed the same kind of measurement, which we will call the standard measurement. With that, we record the effects of dose $\mathcal{D}$, dose rate $\dot{\mathcal{D}}$, and preparation temperature T_{prep} simultaneously. In a standard measurement, we record one XPCS series per fluence/absorber configuration in table 3.1. We start with the lowest fluence to reduce radiation effects on neighboring measurement spots caused by radicals diffusing in the sample. At the lowest fluences, the photon yield on the detector I_{pix} in Eq. (3.6) is low, which we compensate by rather long exposure times ($t_{\mathrm{exp}} \approx 0.5\,\mathrm{s}$). With increasing fluence, we can reduce the exposure time and increase the number of frames for better resolution at the same SNR. Table 8.1 in the appendix shows typical combinations of absorbers, t_{exp} and N_{fr}.

For high fluences $\Phi \geq 5 \times 10^9\,\mathrm{ph\,s^{-1}\,nm^{-2}}$, we record two series per fluence: one with a short exposure time $t_{\mathrm{exp}} = 0.005\,\mathrm{s}$ to resolve effects of low doses and one with a longer exposure time $t_{\mathrm{exp}} = 0.04\,\mathrm{s}$ to reach high doses without increasing the number of frames above the memory capacity of the detector.

These standard measurements were recorded on all three sample sets approximately one hour after the sample preparation at T_{prep} (Table 3.2.)

3.5.2 Dose Effects

The second type of measurement is designed to disentangle the effects of the dose from those of the dose rate. To achieve this, we irradiate a single spot on the sample with a low dose rate ($\dot{\mathscr{D}} \leq 0.03\,\mathrm{kGy\,s^{-1}}$) for times on the scale of hours. These measurements were performed with samples prepared at 68 °C and 75 °C from sample set two and the 65 °C, 70 °C, 75 °C, and 80 °C samples from data set three.

3.5.3 Dose Rate Effects

To explore the nature of the dose rate effects, we performed a third type of measurement inspired by experiments of Ruta et al. on oxide glasses [56]. There, the fluence, and thereby the dose rate, on the sample are changed during the recording of a series of detector frames. At P10, it was at the time of the experiment not foreseen to change the absorber during a series, so we split the measurement into several series on the same spot with a change of absorbers between the series. We start with a low fluence/dose rate, comparable to the ones from the dose-effect measurement, and switch to increasingly higher dose rates, always returning to the initial fluence/dose rate in between to track changes in the dynamics. These measurements were performed on the 57 °C, 65 °C, 70 °C, 75 °C, and 80 °C samples from data set three. A typical sequence of absorbers, exposure times, and number of frames is given in Table 8.2.

3.5.4 Aging Effects

Gels and glasses relax very slowly towards equilibrium, which is called aging of the gel/glass [215, 269, 270]. It is necessary to investigate how the time scales of these aging effects compare to the time scales of measurements that aim for other effects like radiation effects. Therefore, we performed some aging studies on the samples prepared at 70 °C and 80 °C from data set one. The measurement is very similar to the standard measurement. However, we record three consecutive series per fluence/dose rate to see if there are differences on the time scale of several hundred seconds. In addition, we add standard measurements on the same samples three and six hours after the first measurement to investigate aging effects on the time scales of hours.

Chapter 4

Data Handling

Because of the large 2D detectors and the long time series, X-ray photon correlation spectroscopy (XPCS) experiments can create data amounts on the order of terabytes and more, especially at X-ray free electron lasers where the exposure times are short. Currently, there are combined efforts in the scientific community to make data findable, accessible, interoperable, and reusable (FAIR) [271] to increase the efficiency of scientific research. In this chapter, we will see how XPCS data are stored at the P10 coherence applications beamline (Sec. 4.1), how metadata are organized (Sec. 4.2) and how the data are processed (Sec. 4.3). Details on the data analysis are given in Sec. 4.4. A structure for the joint storage of metadata and processed data and results is presented in Sec. 4.5.

4.1 Raw Data Format and Storage Structure

An XPCS experiment requires the recording of a time series of scattered intensities, which is nowadays done with large 2D detectors. The EIGER X 4M detector used in this study consists of eight detector panels with more than four million pixels in total. A typical XPCS series consists of a few thousand frames, so a few billion photon count values need to be saved for every series.

In the P10 file storage location, one folder is created per data-taking command where all the data are saved. The folder name starts with a user-given string and is automatically extended by an integer that is incremented for every new data-taking command. Within this folder, there is one sub-folder for every detector that recorded data and an additional file with the extension *.fio* where parameters from the beamline are saved, like, for example, the sample-to-detector distance, properties of the detector, and the photon energy.

There are two commands for recording a series of detector frames at P10: the series command

and the scan command. The series command takes the number of frames, the exposure time, and the delay time as input and records a single XPCS series. The scan command can be used for recording the same XPCS series on different sample positions to increase statistics or test the homogeneity of the sample. In addition to the arguments of the series command, it takes the name of one of the sample motors, an upper and lower limit for the movement, and the number of spots in that range. Both commands return a three-dimensional array for every spot where the photon counts are stored; these are stored in the sub-folder of the respective detector. The format is the hierarchical data format 5 (HDF5) which allows to store several data arrays next to metadata in a single file with a tree-like organization. This option of adding data is currently not used. Instead, the raw data files are complemented by a batchinfo file and a master file.

From the batchinfo file, information like the number of frames, exposure time, and the position of the beam center on the detector can be extracted. The master file contains more detailed information on the detector elements or can be used for saving positions of sample stages with more complex orientations, which is not necessary for our setup. We will mainly access the raw scattering data and the meta data that are used for matching detector pixels and momentum transfer values.

Our setup contains a Linkam temperature control stage. Its temperatures are automatically written in a separate log file every two seconds, together with a time stamp. This allows the reconstruction of the temperature during the experiment.

4.2 Meta Data Storage

Not all metadata are stored in the online P10 data storage. In addition, there are usually two logbooks that need to be maintained by the experimenting group: one hand-written logbook where all measurements, sample/setup changes, and irregularities are reported in chronological order. These log books are stored at the beamline and must be scanned at the end of the experiment.

The second logbook is typically an online folder shared among the participants of the experiment. It may contain more details on the sample preparation, a table with all measurements, code snippets for the data analysis, or preliminary plots of the recorded data.

In order to make data FAIR, one would need to collect all the information from the logbooks and the beamline metadata and store them together with the raw data. As the raw data of typical XPCS experiments with a duration of four days easily reach terabyte sizes, it is worthwhile to consider to what extent processed data could replace raw data without lowering the data quality. Some basic data processing steps are introduced in the next section.

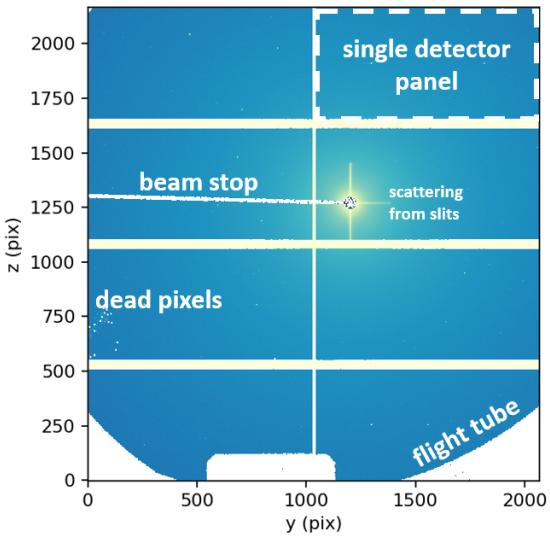

Figure 4.1: Scattering pattern from cooked egg white recorded with the EIGER X 4M detector. Features that need to be masked before analysis: the region between single detector panels, beam stop, hot/warm/dead pixels, slit scattering, and the shadow of the flight tube.

4.3 Data Processing

Before calculating correlation functions or ultra-small angle X-ray scattering (USAXS) profiles, we need to mask some detector artifacts and identify regions of interest (ROIs).

4.3.1 Detector Masking

We record our data with a two-dimensional EIGER X 4M detector. Figure 4.1 shows some raw scattering data integrated over time where several artifacts are visible that need to be masked to obtain meaningful data.

The EIGER X 4M detector consists of eight modules that are arranged in a 2×4 grid. Between the detector modules, there are some rows/columns where no data are recorded and that need to be masked away. Each module consists of eight quadratic readout chips with 256×256 pixels [272], and the edges of these readout chips must also be masked. The direct X-ray beam is blocked by a beam stop as the high photon counts from the direct beam would harm the detector. In addition to the shadows of the circular beam stop and its horizontal holder, there is a shadow from the flight tube that connects the two experimental hutches, limiting the q range in the USAXS geometry. All these shadows are marked as bad pixels in our mask. The coherent part of the X-ray beam is selected using pairs of slits. The scattering from these slits causes intense

scattering in the vertical and horizontal directions close to the direct beam. We mask these intense streaks and extend this mask of the horizontal and vertical scattering to the edges of the detector (Fig. 4.2).

Other artifacts are hot, dead, and warm pixels of the detector. Hot pixels pretend to detect photons in every frame and can be identified by masking all pixels with high counts in a data set with a low scattering intensity. Dead pixels no longer count photons and can be identified in the reverse way by masking all pixels with no photon counts in a strongly scattering sample like aerogel. Warm pixels are the most difficult to detect as they overestimate the photon count but are not counting all the time. They cause a sharply defined peak in the integrated scattering curve and can be identified by being significantly brighter than their neighbor pixels. Currently, one warm pixel is on the EIGER X 4M detector at P10.

The mask for this study is created with the `drawmask` tool from the pyFAI (python fast azimuthal integration) library, which contains tools for masking different shapes. There are two conventions for the definitions of the mask. Most X-ray analysis libraries mark the pixels to be ignored by one and the intact pixels by zero. The X-ray analysis software for XPCS data (Xana) [273] that we use requires masks where the good pixels are marked as one and the bad pixels as zero, which has the advantage that masking can be done as a multiplication of the intensity with the respective mask.

4.3.2 ROI Definition

The calculation of the $g^{(2)}$ function (Eq. (2.28)) contains an average over pixels that is useful to increase statistics. In our transmission geometry, together with the randomly oriented proteins and protein gels, we expect a scattering pattern that is azimuthally symmetric around the position of the direct beam. We can, therefore, sacrifice the information on the direction of q and gain statistics if we define our q-ROIs as concentric annuli around the direct beam. The twelve annuli used in this study are shown in Fig. 4.2 together with the final detector mask.

The q-ROIs cover a q range from $0.006\,\mathrm{nm}^{-1}$ to $0.08\,\mathrm{nm}^{-1}$ which corresponds to length scales of $\approx 0.1\,\mu\mathrm{m}$ to $1\,\mu\mathrm{m}$ to catch the dynamics of the gel network. The five annuli at the lowest q have a width of $\delta q = 0.002\,\mathrm{nm}^{-1}$ which is increased to $\delta q = 0.006\,\mathrm{nm}^{-1}$ for the annuli at higher q to compensate the lower photon statistics with more pixels. In total, the q-ROIs cover 4.4×10^6 pixels which is $< 10\,\%$ of the pixels of the EIGER X 4M. Consequently, the data storage volume for XPCS data could be reduced significantly by storing only the time-resolved intensities in the q-ROIs.

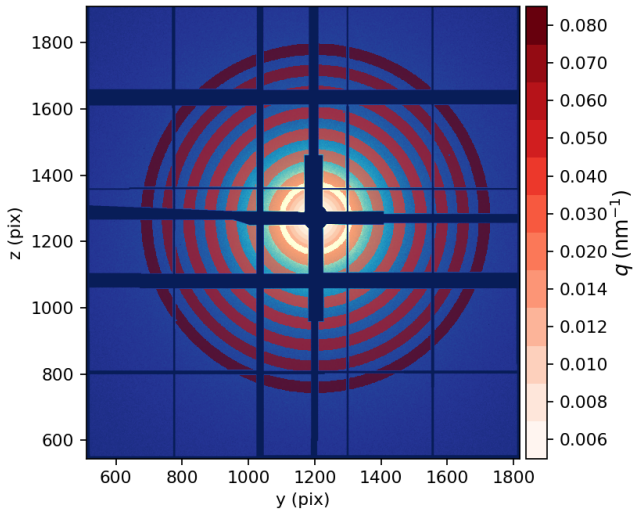

Figure 4.2: Scattering pattern after masking. The twelve regions of interest are highlighted in red. The mean momentum transfer q for every region is indicated on the color bar.

4.3.3 Xana Working Principle

The processing of the raw data and the calculation of scattering profiles and correlation functions are done with Xana [273]. Xana can handle the storage structures and detectors of the P10 beamline at Deutsches Elektronen-Synchrotron (DESY) and the ID02 and ID10 beamlines at the European synchrotron radiation facility (ESRF), which are the established beamlines for XPCS experiments at European synchrotrons.

Having created a mask file, which can also be done within Xana, the next step is to create a setup file where the q-ROIs are defined. Here, the metadata need to be inserted that are needed to convert pixel position into momentum transfer like photon energy, beam position, and sample-to-detector distance. Once the setup file is saved, it can be reused to analyze all measurements with the same experimental setup.

For the analysis of the data, a Xana object needs to be created that gets a path to the setup file and a folder for saving the processed data. This Xana object is connected to several folders with experimental raw data. After this connection, Xana can display a table with the number of frames, exposure time, and delay time for every recorded series in the connected folders. From this table, we can identify the measurements to be analyzed.

Xana can perform three different kinds of analyses: X-ray photon correlation spectroscopy (XPCS), small-angle X-ray scattering (SAXS), and X-ray speckle visibility spectroscopy (XSVS)

[274]. We use the first two analysis modes. Once the first analysis is started, Xana creates a database file in the results folder, where the information on the analyses is stored with the paths to the processed data. The processed data are stored in pickle files with one file per correlation function or scattering profile. For further analysis and plotting, Xana objects can be connected to this database file from which all the processed data can be accessed. There is also the option to filters for series, sample names, or analysis types.

4.3.3.1 Correlation analysis

In the XPCS analysis mode, Xana calculates by default a multi-τ $g^{(2)}$ correlation function like in Eq. (2.28) as long as the data are equally spaced in time. This $g^{(2)}$ function is helpful for the investigation of equilibrium dynamics, but for the investigation of beam effects, the calculation of two-time correlation functions (TTCs) is required. Xana offers different options for normalization of the TTC from which we chose the option *symmetric*, which used the mean intensities in each q-ROI for the denominator of Eq. (2.33). The current version of Xana does not include a method for TTC cutting, which was programmed separately for our analysis.

4.3.3.2 Calculation of Scattering Profiles

The SAXS analysis mode of Xana is based on the pyFAI azimuthal integrator [275], which takes the detector geometry and a two-dimensional raw data array as input and returns an integrated scattering profile $I(q)$. It can be used for the calculation of our scattering profiles recorded in the USAXS setup, as they only differ in the geometry of the beamline setup. For the analysis of the structure, we do not require the precision of a few thousand time-resolved scattering profiles per series, but we can average the data into chunks in time, which is an option directly offered by Xana. For every recorded series, we perform one round of SAXS calculations where 100 frames are averaged together. This time resolution is sufficient to compare the overall effect of the dose.

For the comparison of the structural changes under different dose rates at small doses, we need additional calculations with higher precisions. Therefore, we perform a second round of SAXS analyses where only the SAXS curves up to a total dose of 200 kGy are regarded. Within this range, we calculate 100 averaged SAXS curves for comparison. For example at absorber 0, the 200 kGy are reached within 50 s which equals 1250 frames with an exposure time of 0.04 s. So, in this second round, we would calculate 100 SAXS profiles in steps of twelve frames to resolve the low-dose behavior of the structure.

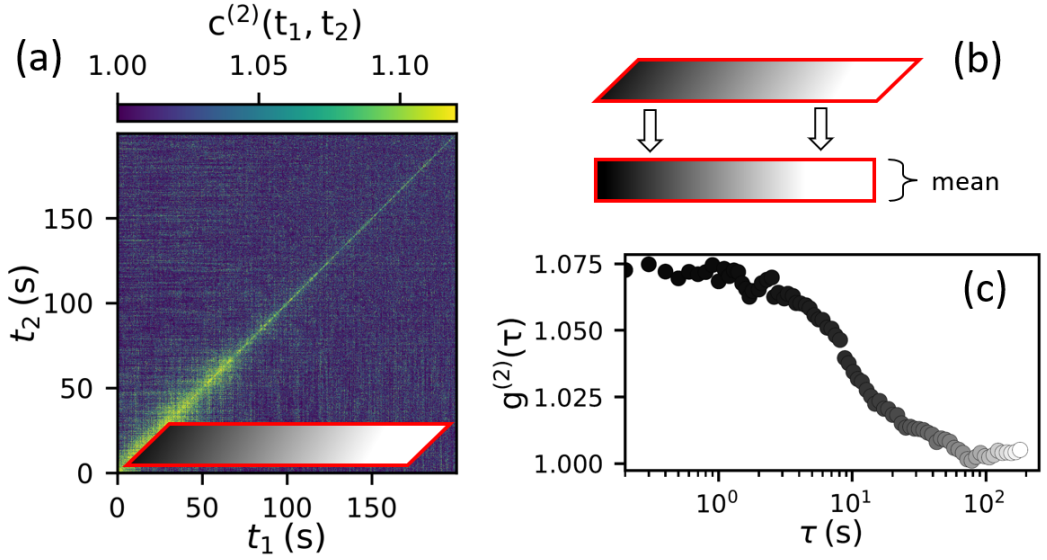

Figure 4.3: Illustration on the average over several horizontal $g^{(2)}$ cuts. (a) TTC from an egg white sample prepared at 63 °C. For the average over several $g^{(2)}$ cuts along the t_2-axis, we consider a region with the shape of a parallelogram. (b) the average is taken over data points with a similar distance to the $t_1 = t_2$ diagonal, which is indicated by similar shades of gray here. So the parallelogram is reshaped into a rectangle before the average along t_2 is done. (c) final $g^{(2)}$ function on a logarithmic scale.

4.4 Data Analysis

The TTCs calculated by Xana offer a first impression of the temporal evolution of the system. For quantitative insights, we need to extract $g^{(2)}$ cuts and fit those with a Kohlrausch-Williams-Watts (KWW) type exponential decay. Here, we describe the cutting of the TTCs and explain the fitting procedure in those cases where the decay of the $g^{(2)}$ function is not fully included in the experimental time window and the case of a double-exponential decay.

4.4.1 $g^{(2)}$ cuts

From the TTCs, we extract $g^{(2)}(q, \tau)$ functions via horizontal cuts starting at the $t_1 = t_2$ diagonal of the TTC at different starting times. The $g^{(2)}$ cuts are thus functions of the time difference $\tau = t_1 - t_2$ with $t_1 \geq t_2$. We increase the statistics by averaging several cuts along the t_2-axis, as shown in Fig. 4.3. We calculate the average $g^{(2)}$ cut from these parallelogram-shaped regions such that points with the same distance τ to the diagonal end up in the same data point. This is

indicated by the different shades of gray in Fig. 4.3(b,c). The averaged $g^{(2)}$ cut is labeled with the mean of the time range along t_2 which would correspond to $\approx 15\,\mathrm{s}$ in the illustration in Fig. 4.3.

In the analysis, we vary the range for averaging according to the SNR of the TTC and the exposure time of one frame: for the long measurements with the highest absorber (abs. 24, $\Phi = 0.003\,\mathrm{ph\,s^{-1}\,nm^{-2}}$,$\mathscr{D} = 0.002\,\mathrm{kGy\,s^{-1}}$), a time interval of 200 s leads to fittable $g^{(2)}$s. At high fluences, we could add a fast measurement with $t_{\mathrm{exp}} = 0.005\,\mathrm{s}$. For these, we obtain a reasonable signal-to-noise ratio (SNR) in the $g^{(2)}$s already when averaging over time frames with a sub-second width. With increasing starting time of the $g^{(2)}$ cuts, they become shorter in time, which might lead to less precision in the fits.

4.4.2 $g^{(2)}$ fits

We model the $g^{(2)}$ correlation functions by a KWW function [209]:

$$g^{(2)}(q,\tau) = 1 + \beta(q)\, e^{-2(\Gamma(q)\tau)^{k(q)}}. \tag{4.1}$$

Here, $\beta(q)$ is the q-dependent speckle contrast [276], $\Gamma(q)$ is the decorrelation rate and $k(q)$ is the KWW exponent that describes the distribution of Γ and thereby contains information on the type of motion [20, 22]. The contrast can be determined experimentally by measuring a static sample like an aerogel. In our experiment, these measurements yield speckle contrasts of $\beta(q = 0.006\,\mathrm{nm^{-1}}) = 10.6\,\%$ and $\beta(q = 0.02\,\mathrm{nm^{-1}}) = 9.7\,\%$. In some measurements, this y-intercept of the $g^{(2)}$ function does not match this experimental speckle contrast. This might be caused by a second decay of the correlation function at times shorter than the experimental time window or by fluctuations in the contrast induced by intensity variations over time. Figure 4.4 shows such $g^{(2)}$ functions from measurements on a 63 °C sample with absorber 18 ($\Phi = 0.02\,\mathrm{ph\,s^{-1}\,nm^{-2}}$). Instead of setting a fixed contrast in the fits, we put the experimental contrast as an upper boundary for the β parameter. The results for β in the example fit are shown in the upper panel in the right column. All fitted contrasts lie below the experimental contrast of 10.6 %. The panel figures below give the results for the other two fit parameters Γ and k.

In Fig. 4.5, we compare fits on $g^{(2)}$ cuts starting at the same dose but at different momentum transfers q and notice that especially at intermediate q ($0.2\,\mathrm{nm^{-1}}$ to $0.4\,\mathrm{nm^{-1}}$) the $g^{(2)}$ function does not decay to one but to some finite plateau. We label this offset as b and add it to the fitting function via

$$g^{(2)}(q,\tau) = 1 + b + \beta \exp\left(-2(\Gamma\tau)^k\right). \tag{4.2}$$

We need to clarify the origin of this offset as $g^{(2)}$ decays to some finite plateau were already observed in other gel-like systems earlier [216]. For the Siegert relation (Eq. (2.30)) that describes the relation between $g^{(1)}$ and $g^{(2)}$ correlation functions, we required the intensity to be Gaussian

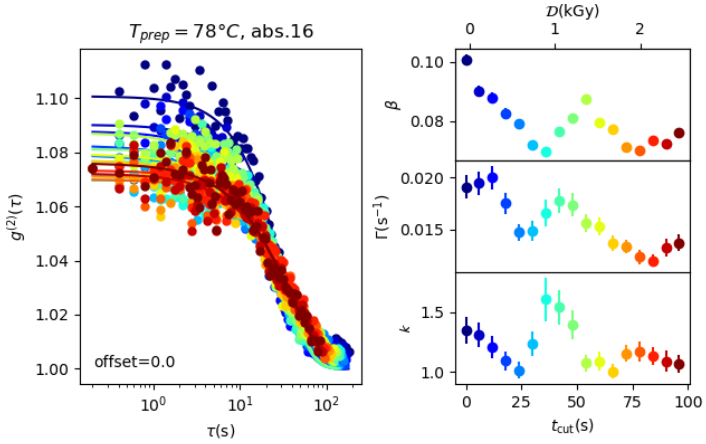

Figure 4.4: Example for KWW-fit on $g^{(2)}$ functions of the sample prepared at 63 °C and measured with a fluence of $\Phi = 0.02\,\mathrm{ph\,s^{-1}\,nm^{-2}}$ (abs. 18). The y-intercept of the $g^{(2)}$ function fluctuates at values lower than the determined speckle contrast ($\beta(q = 0.006\,\mathrm{nm^{-1}}) = 10.6\,\%$). We consider that by putting the speckle contrast as an upper limit for the fit range of β.

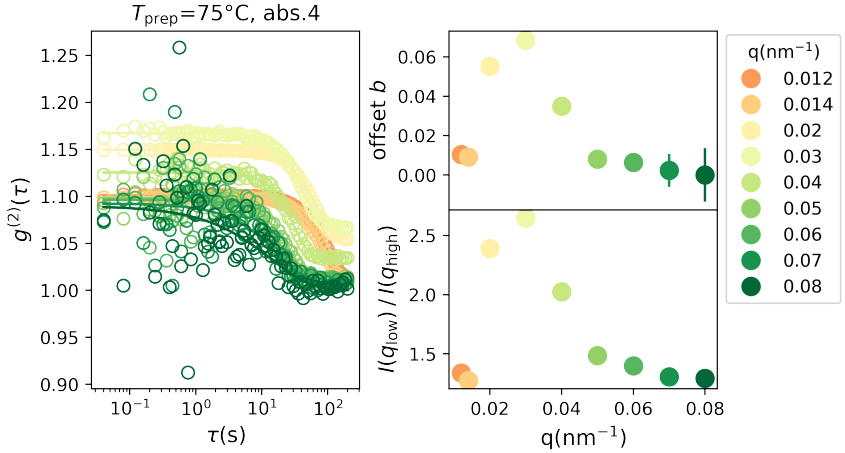

Figure 4.5: Example for modified KWW-fits (Eq. (4.2)) on $g^{(2)}$ functions of the sample prepared at 75 °C and measured with a fluence of $\Phi = 1.7\,\mathrm{ph\,s^{-1}\,nm^{-2}}$ (abs. 4). (a) comparison $g^{(2)}$ cuts with a mean dose of 0.5 kGy at different momentum transfers q as indicated in the legend. Solid lines are fits with Eq. (4.2). (b) fit results for the offset parameter b as a function of q. (c) Quotient of the intensities at the lower and upper edge of each q-ROI.

distributed. Recalling Fig. 4.2 where the q-ROIs were defined, we see that the scattered intensity decreases for increasing q such that the intensity is different at the inner and outer edge of each of the annuli that make up the q-ROIs. To clarify if this is the origin of the decay to a plateau, we plot the quotient of scattered intensity at the inner and outer edge of each q-ROI $(I(q_{\mathrm{low}})/I(q_{\mathrm{high}}))$and compare it to the parameter b. The results are shown in the right panels of Fig. 4.5, where we can see that the trends of both quantities match with a peak around $q = 0.03\,\mathrm{nm}^{-1}$. One can nicely see how the offset b increases as we increase the width of the q-ROIs from $\mathrm{d}q = 0.002\,\mathrm{nm}^{-1}$ to $\mathrm{d}q = 0.006\,\mathrm{nm}^{-1}$ for $q \geq 0.02\,\mathrm{nm}^{-1}$. From this, we conclude that the plateau does not originate from confined motion in the gel but from deviations in the intensity statistics caused by the finite width of the q-ROI.

In the data analysis, we handle this by introducing b to the fit function as in Eq. (4.2). For systems that display slow dynamics, the decay of the $g^{(2)}$ function might be cropped as shown in Fig. 4.6. In these cases, we need to fix the offset b to obtain the correct decorrelation rates and KWW exponents while not fixing the contrast. As described above, the parameter b depends on the shape of the scattered intensity profile and is, therefore, q- and sample-specific. The samples where we do not measure the complete decay are those prepared at high temperatures and measured with a low fluence. In these samples, we can shift the $g^{(2)}$ decay to earlier times by applying higher fluences and get the value of b. This can be done as the structure and, thereby, the static scattering profile of the samples prepared at high temperatures is resistant to fluence effects for doses of several tens of kGy, as we will see later. For Fig. 4.5 the offset was fixed to $b = 0.065$.

In the results of some samples, we find that the $g^{(2)}$ functions display a double exponential decay. For the egg samples from data set two, this is observed through all preparation temperatures. In contrast, in data set three, this is only found in the results of the 75 °C and the 78 °C samples when they are measured with the highest dose rates ($\dot{\mathscr{D}} \geq 2\,\mathrm{kGy\,s}^{-1}$). An example is shown in Fig. 4.7. Double-exponential decays of $g^{(2)}$ functions occur if two main processes are happening on two distinct time scales. This is also observed in gel systems, where one process is the locally confined thermal movement of the constituents of the gel network, and the other is the relaxation of the larger structure of the gel network itself. We describe these double-exponential decays with a linear combination of two KWW expressions weighted with a relative amplitude β_0:

$$g^{(2)}(q,\tau) = 1 + b + \beta \left(\beta_0\, e^{-2(\Gamma_1 \tau)^{\alpha_1}} + (1-\beta_0)\, e^{-2(\Gamma_2 \tau)^{\alpha_2}} \right). \tag{4.3}$$

Here, the parameters describing the slower decay are indexed with 1 (upper triangles in Fig. 4.7), and those belonging to the fast decay are indexed with 2 (lower triangles in Fig. 4.7). As we are interested in the stress-relaxation dynamics of the gel network, we focus our analysis on the slower second decay, which displays ballistic motion and yields results that are consistent with

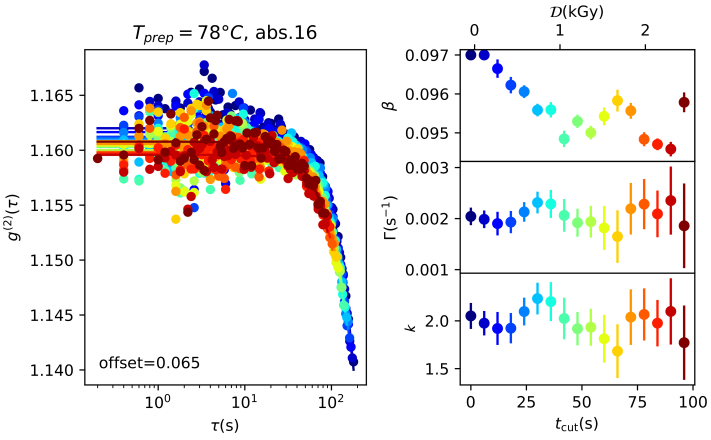

Figure 4.6: Example for KWW-fit on $g^{(2)}$ functions of the sample prepared at 78 °C and measured with a fluence of $\Phi = 0.04\text{ph}\,\text{s}^{-1}\,\text{nm}^{-2}$ (abs. 16). Due to the slow dynamics, the correlation function does not decay completely within the time frame of the measurement. The offset of 0.065 is known from measurements with a higher fluence where the decay shifts into the experimental time frame. The panels on the right show the results for the three free fit parameters: contrast β, decay rate Γ, and KWW exponent k.

those from the single-exponential $g^{(2)}$ functions at other temperatures/fluences.

4.4.3 $\Gamma(q)$ fits

For a comparison of radiation effects across preparation temperatures and momentum transfers, we make use of the ballistic motion of the stress relaxations in the gel network. For this type of motion, the decorrelation rate Γ is proportional to the momentum transfer q such that we can fit functions of the type

$$\Gamma(\Phi, \mathcal{D}, T_{\text{prep}}, q) = v(\Phi, \mathcal{D}, T_{\text{prep}}) \cdot q \tag{4.4}$$

to obtain the slope $v(\Phi, T_{\text{prep}})$ that has units of a velocity. An example for this procedure is shown in Fig. 4.8. We eliminate the dependency on the dose $\mathcal{D}$ from Eq. (4.4) by regarding only $g^{(2)}$ cuts that start at a mean dose of 1 kGy. As described in section 4.4.1, we average the $g^{(2)}$ cuts over some time interval along the t_2 time axis of the TTC. This time interval is chosen such that the time in the middle of the cut equals 1 kGy. We decided for this specific dose as for even lower doses we might face opening effects of the detector shutter in the very first frames of each measurement.

For some measurements, a fit with Eq. (4.4) does not describe the data well, but we need to

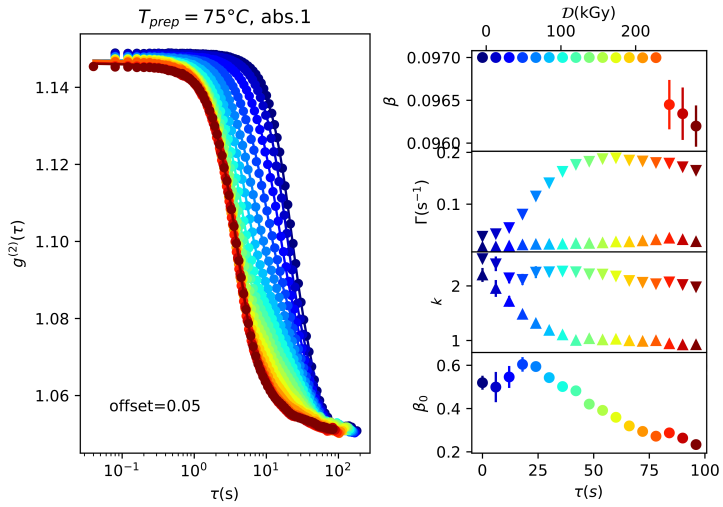

Figure 4.7: Example for KWW-fit on $g^{(2)}$ functions of the sample prepared at 75 °C and measured with a fluence of $\Phi = 4.4\,\mathrm{ph\,s^{-1}\,nm^{-2}}$ (abs.1). Upon increasing dose (color change from blue to red), the correlation functions displays a second decay. The panels on the right show the results for the six free fit parameters: contrast β, two decorrelation rates Γ, the corresponding KWW exponents k, and the relative amplitude of the slower decay β_0. The fit results for the slower decay are indicated with upper triangles (▲), and the results for the faster decay with lower triangles (▼). It can be seen that the aerogel contrast of 9.7 % was set as an upper limit for the contrast.

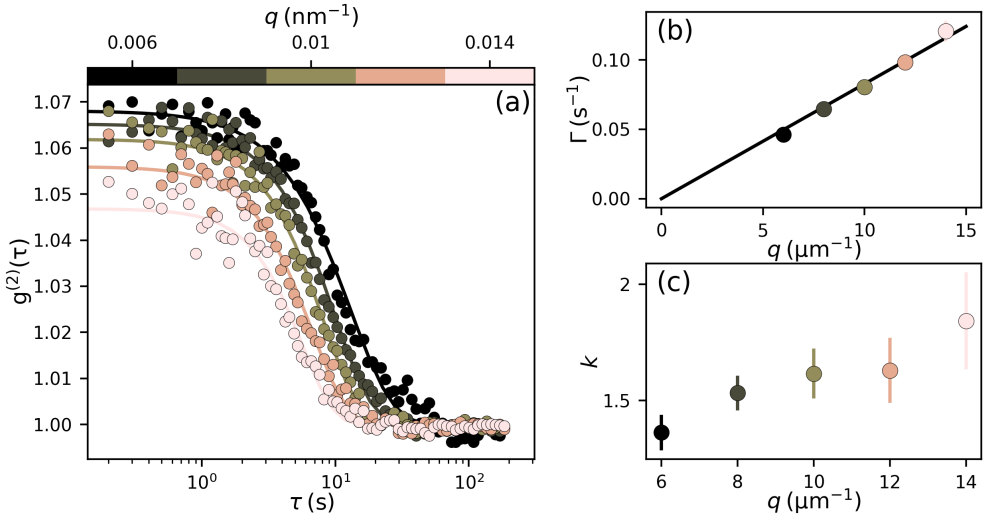

Figure 4.8: Illustration of the determination of the velocity v from $g^{(2)}$ cuts at different q. The data stem from an egg white gel prepared at 63 °C and measured with a fluence of $0.14\,\mathrm{ph\,s^{-1}\,nm^{-2}}$. (a) $g^{(2)}$ cuts starting at a mean dose of 1 kGy for different momentum transfers q indicated by color. Solid lines are fits with Eq. (4.2). (b) Decorrelation rates from the fits in (a). The black solid line is a linear fit $\Gamma = vq$. (c) KWW exponents from fits in (a).

add a y-intercept that is larger than zero:

$$\Gamma = \Gamma\prime + v \cdot q. \tag{4.5}$$

This q-independent contribution $\Gamma\prime$ is attributed to caging and confinement effects [277, 278]. We use Eq. (4.5) for the fit of $\Gamma(q)$ instead of Eq. (4.4) for the description of data of the following samples from data set three: $T_{\mathrm{prep}} = 70\,^{\circ}\mathrm{C}$, $\mathscr{D} < 0.09\,\mathrm{kGy\,s^{-1}}$; $T_{\mathrm{prep}} = 73\,^{\circ}\mathrm{C}$, $\mathscr{D} < 0.9\,\mathrm{kGy\,s^{-1}}$; $T_{\mathrm{prep}} > 75\,^{\circ}\mathrm{C}$, $\mathscr{D} > 0.9\,\mathrm{kGy\,s^{-1}}$.

4.5 Storage of Metadata and Results

As XPCS experiments generate large amounts of raw data and calculations of correlation functions can become time-consuming, it is useful to store processed data. In this section, we will present the quantities we store from the analyses presented above and the structure of this processed data file.

The neutron and X-ray scattering community has worked on a common format for data exchange for a long time. A result of this discussion was the development Neutron X-ray μ

(muon) science (NeXus) data format, which aims to combine raw data from detectors and other monitors together with metadata on samples and users and plottable processed data [279–281]. This NeXus data format is based on the HDF5 data format [282] in which the raw data for our experiments are stored. Instead of the NeXus format, we will use the standard HDF5 data format and not follow the NeXus storage principles as the joint storage of processed data with raw and monitor data requires close collaboration with the facilities, which is/was realized in projects like DAPHNE4NFDI, PaNOSC or ExPaNDS [283]. Here, we will present the data storage structure for the results of a standard measurement (Sec. 3.5.1), where we record a series of detector frames with different fluences. We summarize all these different scans in one HDF5 file per preparation temperature.

HDF5 files consist of three elements: groups, data sets, and attributes. Groups are used to build the tree-like structure of the HDF5 file. We will create one group for each scan such that one can navigate to the location of some XPCS results for scan X in a file f via `f['scan_X/XPCS]`. Here, `XPCS` would be another group that is nested in the primary group `scan_X`. To each group or the file itself, we can add data sets. Data sets are typically generated from arrays of Python's standard array library `numpy`. In our case, these data sets could be masks, intensities, or numeric axis labels. Other types of data, like strings or tuples, can be added as attributes to either groups or data sets. This enables the joint storage of some metadata together with the processed data from the XPCS experiment.

The structure of the HDF5 file for storage of meta and processed data is shown in Fig. 4.9. Groups are marked by bold letters; subgroups are indicated by indention. Attributes are written in italic letters to distinguish them from data sets. The data sets and attributes that belong to a specific group are enclosed by a colored rectangle. Accessing the data works in the following way: For example if we open the HDF5 file (in this case `eggwhite_60C.hdf5`) into a Python object that we call `f` we could get the TTC from the first scan and the first q-ROI via `f[/scan_1/q_0/ttc/][()]`. In HDF5 files, there is also the option to access only part of the data by putting the indices of these data points in the second set of square brackets in the expression above. This is especially useful when computer memory is limited.

On the top level (dark purple box in Fig. 4.9) we store general information on the beam time like beam time ID or the beam size. These quantities usually remain unchanged during an experiment, and we add them as attributes to the root of the file tree. Information on the sample put into the beam is stored in a group `scan_info`. This is accompanied by information on the beam center on the detector, as this can be easily changed by moving the detector. Accordingly, the mask file needs to be adapted, which is why the mask file is added as a data set to this group.

On the same level as the `scan_info` group, we create one group for every series that is recorded on this sample. We start to numerate the scans with one in line with the numeration of the P10 file system. To each of these `scan_X` groups, we add the following attributes related to

Figure 4.9: Structure of HDF5 file for storing processed and selected meta data.

the settings for the respective series of data frames: number of silicon absorbers used, resulting transmission of the absorber setup, number of frames, and exposure time.

The results for every scan are divided into three parts: q-ROI specific XPCS results like TTCs, dose-specific results, and SAXS results. The groups for the q-ROI specific results are named by the number of the q-ROI starting at zero. In this group, we store the calculated TTC, the time labels for the TTC axes and add the value of q in units of inverse nanometer as an attribute to the group. Within the group, there are up to two subgroups: `horizontal_cuts` and `diagonal_cuts`, which gives the opportunity to test both directions for $g^{(2)}$ cuts on the data. In our study, we employ the horizontal cuts. On this level, there are two subgroups, one for fits with a single-exponential decay (`1_exp_fit`) and one for fits with a double exponential decay (`2_exp_fit`). For both variants, we store the start times of the cuts, the dose equivalents of these times, the resulting $g^{(2)}$ functions, and the time labels of their data points. On the same level, the results from the fits with the respective fit function are stored. These results are saved in two-dimensional arrays with one dimension for the number of fit parameters and one dimension for the number of $g^{(2)}$ cuts. To retrieve the right assignment of parameters to the entries in the array, a list with the parameter names is added as an attribute to the array with the fit results. A similar array is saved for the standard deviation of the fit results. During the fit, we have the opportunity to define the initial value of each parameter and limit the range of the outcome. As we make use of this option, especially for the contrast and the offset, we store these constraints in another subgroup `fit_settings`. This subgroup contains one data set per fit parameter that is named starting at `par0`. Each data set is an array with three entries, the first being the lower boundary for the fit range, the second being the initial value of the parameter, and the third being the upper boundary for the fit range. This information makes it possible to reconstruct the $g^{(2)}$ fits.

Besides the groups for the q-ROI specific XPCS results, we create a group for results spanning different q-ROIs. For our study, these are the results where we compare $g^{(2)}$ functions starting at the same dose on the diagonal of the TTC and therefore name this group `constant_dose`. Within this group, we create one subgroup for every dose where $g^{(2)}$s are compared. For all temperatures, there is a 1 kGy subgroup, which is complemented by groups for higher doses in some data sets. In each of these groups, we save the range of doses over which we averaged the $g^{(2)}$ functions (for a 1 kGy cut, a typical range is 0.5 kGy to 1.5 kGy) and the time equivalents of these dose ranges as well as an array with the resulting $g^{(2)}$s and their time and q labels. The results from the $g^{(2)}$ fits are stored in an array similar to those in the q specific results. In addition, there is one dataset with the velocity resulting from the $\Gamma(q)$ fit and its standard deviation. In the case of the fits at a constant dose, we do not need to employ double-exponential fits, which is why no subgroups are discriminating between fit functions on this level.

The results from the static scatting are added in a group `SAXS` which is located on the same

tree level as the `constant_dose` group (dark gray box in Fig. 4.9). Within the `SAXS` group, there are two subgroups: one for results that are azimuthally integrated around the direct beam and one for results that have the original shape of the detector. The latter is used to store an array with the intensity in each detector pixel integrated over the whole series. This can be useful to identify scans with anisotropic scattering, which might occur if the beam hits the capillary wall. We call this subgroup `mean_intensity` and the data set in this group `detector`. The other subgroup is named `profiles`, where we store the azimuthally integrated intensity as a function of q and waiting time as it comes out of the Xana analysis.

For a measurement set with 15 to 16 series, the HDF5 file described above has a size of 1 GB to 2 GB without using the HDF5 compressing options so far. We restricted the q-specific analysis to one or two q-ROIs. The file could be complemented by the pixel-wise intensity in the q-ROIs in all frames. This would enable a recalculation of TTCs with different normalizations or thinner q-ROIs. This would enlarge the file for the processed data but could serve as a replacement for storing the whole raw data.

Chapter 5

Results from Static Scattering

This chapter is based on Ref. [261]. In Section 5.1, we investigate the effect of the preparation temperature T_{prep} on the structure of the egg white, which is the foundation for the interpretation of the radiation effects on the different egg white gel networks. Section 5.2 covers the effect of the accumulated dose on egg white gel networks. These investigations are complemented by the effects of different dose rates in Section 5.3

5.1 Temperature Effect

We prepared egg white samples at temperatures between 50 °C to 85 °C, which covers the denaturation temperatures of three of the main proteins present in egg white, which are ovalbumin, ovotransferrin, and lysozyme. The onset of the denaturation can seen from the capillaries with the egg white samples prepared at the lowest temperatures (right panel in Fig. 5.1). There, we notice an increase of turbidity around 60 °C. This is a signature of the first step towards gelation, which is the formation of spherical aggregates by the denaturated proteins [62]. The aggregates in the right panel of Fig. 5.1 are predominantly formed by the ovotransferrin protein that denaturates around 60 °C [62, 149, 168, 169]

Together wit the increase in sample turbidity, the scattered USAXS intensity increases. For the investigation of the temperature effect, we recorded a short measurement with a low dose rate ($\dot{\mathscr{D}} = 10\,\mathrm{Gy\,s^{-1}}$) and kept the accumulated dose below 0.2 kGy. The left panel of Fig. 5.1 shows the azimuthally integrated intensity averaged over the first 100 frames of every measurement to increase the statistics. The scattered intensity in Fig. 5.1 increases with preparation temperature and thereby with the amount of denaturated proteins that participate in the gel network. The most rapid increase by two orders of magnitude is observed around 60 °C, which coincides with

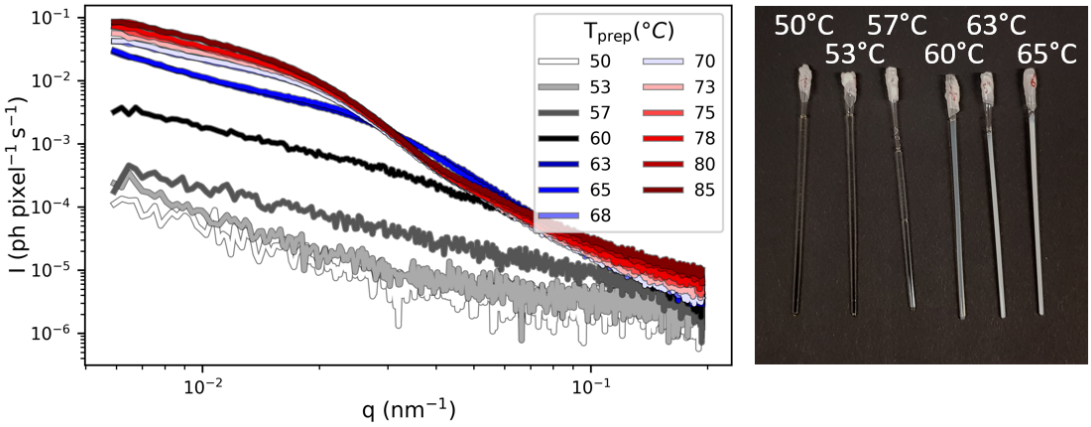

Figure 5.1: Left: USAXS profiles of all samples from data set 3 recorded at a low dose rate of $10\,\mathrm{Gy\,s^{-1}}$. The displayed profiles are averages over the first 100 frames (0.5 s to 20 s depending on exposure time) taken in every measurement to reduce noise. Right: change of turbidity of samples in capillaries after cooking.

the increase in turbidity due to the formation of the aggregates described above.

In Section 2.1.1, we learned that gel networks have fractal properties [115]. It is observed that the intensity scattered from fractals obeys a power law [194, 195, 284],

$$I(q) \propto q^{-\delta}, \tag{5.1}$$

where the exponent δ is connected to the fractal dimension. In a double logarithmic plot, this results in straight lines with a negative slope δ (Fig. 5.2(a)). The above relation holds only at intermediate q between the size of the fractal network and the size of the building blocks of the fractal, which are the protein aggregates in our case. Below the lower q cut-off, the intensity is expected to level off in a Guinier region where $I(q) = \text{const.}$ [194]. This region is not observed in our q-range probably because the percolating gel network is too large and the lower q cut-off is shifted behind the beam stop. Moreover, we do not observe a power law decay with a single exponent, but the exponents change as a function of q, especially at higher preparation temperatures T_{prep}. To catch the different exponents δ we fit eq. (5.1) to the intensity curves in two different regions: one covers the lowest q values ($q \in [0.006, 0.014]\,\mathrm{nm^{-1}}$) and one the region where we see the steepest decrease as a function of q ($q \in [0.04, 0.09]\,\mathrm{nm^{-1}}$). The fitted lines are displayed in Fig. 5.2(a); the results for the exponents δ are shown in Fig. 5.2(b).

The fits in the low q region can be compared to the power law fits on USAXS data by Begam et al. on egg white during the cooking procedure [54, 55]. After 40 min of cooking, they find

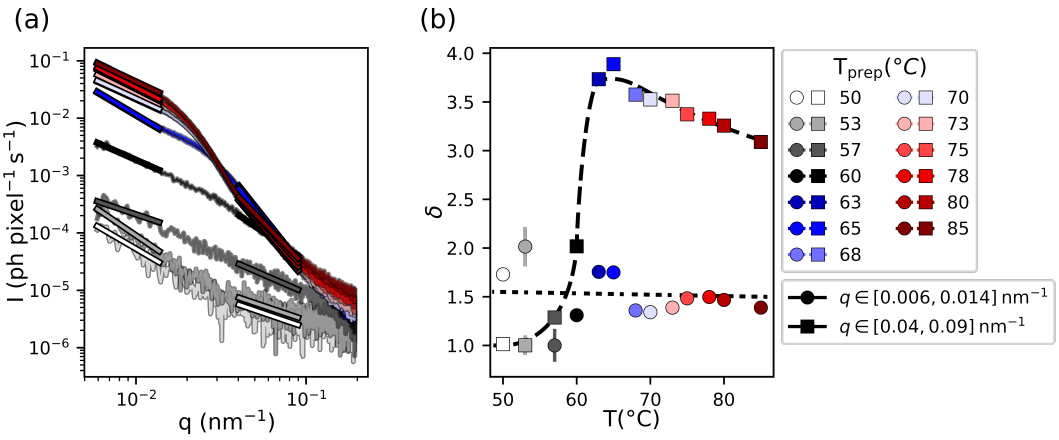

Figure 5.2: (a) Scattered intensities from Fig. 5.1 with fitted power laws from eq. (5.1) in two different q regions ($q \in [0.006, 0.014]\,\mathrm{nm}^{-1}$ and $q \in [0.04, 0.09]\,\mathrm{nm}^{-1}$). (b) Result for the exponent δ obtained from the fits in (a). Circles indicate the fits at low q while square markers represent the fits at higher q. Dotted and dashed lines are guides to the eye.

values of $1.5 < \delta < 2.2$ and conclude that the gel is in the strong link regime, where the inter-aggregate bonds are more robust than the intra-aggregate bonds. The difference to the data presented here is that their samples were measured at the preparation temperature T_{prep} and not at room temperature. Our power-law fits at low q (dotted line and circles in Fig. 5.2(b)) return values of $1.4 < \delta < 2$ at all temperatures except 57 °C and 60 °C, which will be discussed below. This aligns with the interpretation of protein gels as mass-fractals as δ is smaller than the Euclidian dimension ($\delta < 3$). Therefore, we can identify δ at low q with the mass fractal dimension d_m and interpret it as the compactness of the fractal structure [284, 285]. Besides the shape of the USAXS intensity, numerous other experimental techniques allow access to the fractal dimension of a protein gel, like the storage modulus of the gel or its wavelength-dependent turbidity [286]. These studies on a variety of protein gels found values of $1.5 < d_f < 2.8$ [286–293] comparable to our mass fractal dimensions. For our samples prepared at 57 °C and 60 °C, we find lower values of δ approaching one. In the literature, this marks the threshold value below which an interpretation as a mass fractal is not feasible, but the system behaves somewhat like a system of disconnected points [194]. A reason for this loss of fractal properties around 57 °C might be the onset of the denaturation of the ovotransferrin at this temperature. We know that egg white has gel-like properties already at room temperature due to the network formed by the ovomucin protein. Around 57 °C, the denaturation of the first protein (ovotransferrin) sets in and aggregates form. The diffusion of these aggregates that are not yet forming a gel network

might disturb the existing ovomucin network and thus lead to a loss of fractal properties of the USAXS profiles for the samples prepared at 57 °C and 60 °C.

For the fits at higher q we find exponents δ outside the range reported for other proteins. Here, δ increases rapidly from values close to one to $\delta > 3$ for preparation temperatures above 60 °C. These values do not allow for an interpretation as a mass fractal, which indicates that we are above the upper cut-off for the q range where relation (2.22) holds. The upper cut-off is determined by the size of the building blocks of the gel network, which are the protein microaggregates in our case. The formation of these microaggregates leads to an increasing electron density contrast compared to the surrounding water, and the form factor of the microaggregates appears in the scattered intensity. This is why the exponent δ cannot be identified with a fractal dimension at these q values.

Due to the stochastic nature of the proteins' aggregation process, we expect that the size of aggregates follows some (unknown) distribution. We can estimate the upper edge of this distribution as the value of q where the slope of the intensity changes in Fig. 5.1. We will refer to this point as *knee* of the intensity, inspired by the description of the power law spectrum of cosmic rays in astrophysics [294]. For temperatures between 60 °C and 70 °C, this knee is located around $0.03\,\mathrm{nm}^{-1}$ which corresponds to microaggregates of $2\pi/q \approx 200\,\mathrm{nm}$. For higher temperatures, the knee shifts abruptly to $0.02\,\mathrm{nm}^{-1}$ indicating larger microaggregates of $2\pi/q \approx 300\,\mathrm{nm}$. The preparation temperature of 70 °C, where the size of the microaggregates increases, matches the temperature where the ovalbumin protein starts to denaturate. With further increase of the preparation temperature, the size of the microaggregates remains unchanged, even though we expect a higher amount of denaturated ovalbumin.

The average size of the microaggregates in egg white was already determined with another experimental technique: Bonilla et al. [184] performed super-resolution microscopy measurements on egg white prepared at 69 °C, 72 °C and 75 °C and found that the microaggregates cover an area of $\approx 0.07\,\mu\mathrm{m}^2$ on the resulting picture and that their size is comparable at all three recorded temperatures. Assuming a spherical shape of the microaggregates, this area can be translated into a diameter of 300 nm, which is comparable estimations from the USAXS curves above.

From this section on temperature effects, we can conclude that cooked egg white has properties of a mass fractal on length scales of 0.3 µm to 1 µm. At 60 °C, the denaturation of the ovotransferrin causes the formation of microaggregates with a size of ≈ 200 nm. For samples prepared at 70 °C and above, the size of these microaggregates increases to ≈ 300 nm which might be caused by the denaturation of the ovalbumin that sets in at these temperatures.

5.2 Dose Effect

In this section, we investigate how the USAXS intensity is affected by the deposition of high amounts of X-ray energy in the samples, i.e., high doses. We look at the evolution of the intensity during measurements with the highest dose rate $\dot{\mathcal{D}} = 4\,\mathrm{kGy\,s^{-1}}$. The duration of the measurements is 200 s such that the accumulated dose at the end is $\mathcal{D} = 800\,\mathrm{kGy}$.

The first sample is the one prepared at 53 °C where no heat-induced gel network has been formed. The USAXS profiles for increasing time/dose are displayed in Fig. 5.3(a). The scattered intensity increases over the whole q range by a factor greater than three (normalized curves in Fig. 5.3(b)), which points towards an increase in the electron density contrast. As one would naively expect, the increase is initially relatively higher at high q/small length scales (blue curves in Fig. 5.3), with a peak in the normalized intensity around $q = 0.05\,\mathrm{nm^{-1}}$. This indicates that the radiation-damaged proteins assemble into structures with sizes of tens to hundred nanometers. At larger measurement times and doses (red curves in Fig. 5.3), the increase in intensity extends up to the micrometer scale as larger structures form. As the intensity seems to follow a power law decay at low q, this might also be a fractal structure formed by the protein assemblies. The mechanism that causes the proteins to stick together and form the observed assemblies is most likely not the heat-induced denaturation, i.e., unfolding of the protein and exposure of reactive groups, that is responsible for the formation of the microaggregates that constitute the gel network. Instead, the outer shell of the protein is activated by the ionizing X-rays and the radicals formed from the egg white's water content. The proteins turn into highly reactive protein radicals that can aggregate easily. We will refer to these radiation-induced aggregates as protein assemblies to distinguish them from the heat-induced aggregates that form the egg whites gel network.

In the next step, we regard the same measurement performed on a sample prepared at 63 °C, where a gel network formed by ovotransferrin microaggregates is present. Figure 5.4 shows the evolution of the USAXS intensity upon increasing dose. To enhance the details of the changes, panel (b) shows the intensity normalized to the first curve $I(t = 0)$. We observe three different behaviors of the intensity depending on the value of q: At $q > 0.12\,\mathrm{nm^{-1}}$, the intensity increases significantly with the dose. We interpret this, in line with the findings for the 53 °C sample above, as a radiation-induced formation of small protein assemblies from the non-denaturated protein content in the sample. These are smaller than the ovotransferrin microaggregates that form upon heating during the sample preparation. At the lowest q ($q \leq 0.02\,\mathrm{nm^{-1}}$), there is a slight increase in intensity followed by a decrease at doses $\geq 100\,\mathrm{kGy}$. This points towards the formation of larger structures from the gel network at low doses, which we will later interpret as a fluidization of the gel network in the light of the results for the sample dynamics. At high doses, the intensity decreases also in the intermediate q range. We associate this decrease at all

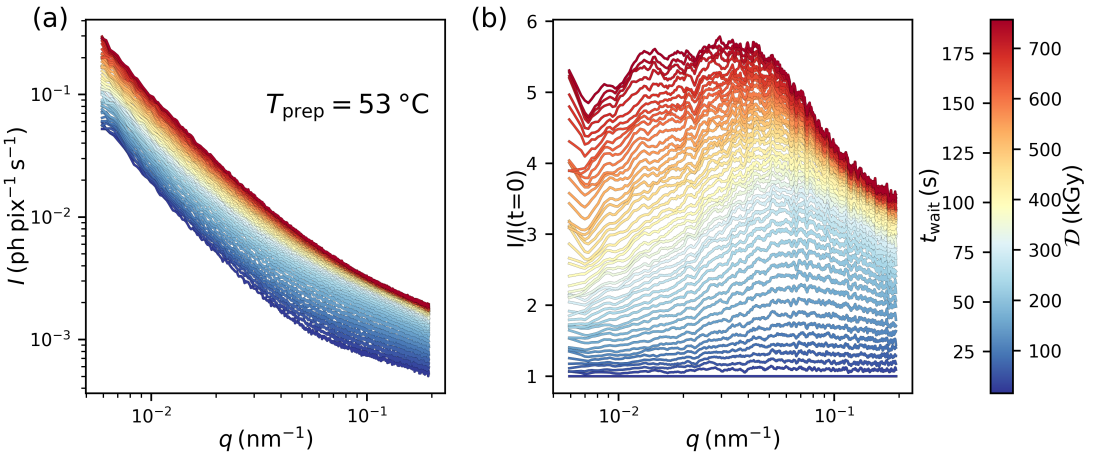

Figure 5.3: (a) Evolution of the USAXS signal under irradiation with $\mathscr{D} = 4\,\mathrm{kGy\,s^{-1}}$ for 200 s. The sample was prepared at 53 °C. (b) USAXS signal normalized to the curve at $t = 0$ s.

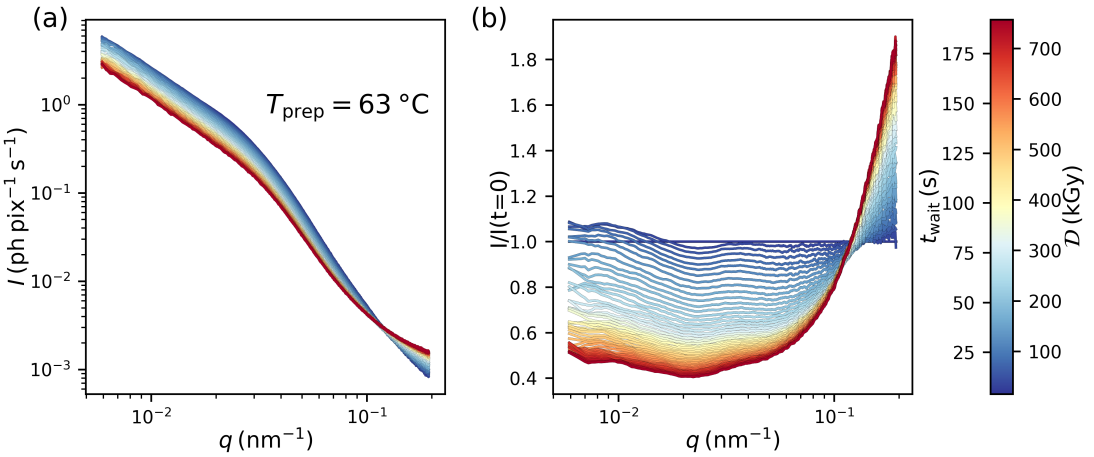

Figure 5.4: (a) Evolution of the USAXS signal under irradiation with $\mathscr{D} = 4\,\mathrm{kGy\,s^{-1}}$ for 200 s. The sample was prepared at 63 °C. (b) USAXS signal normalized to the curve at $t = 0$ s.

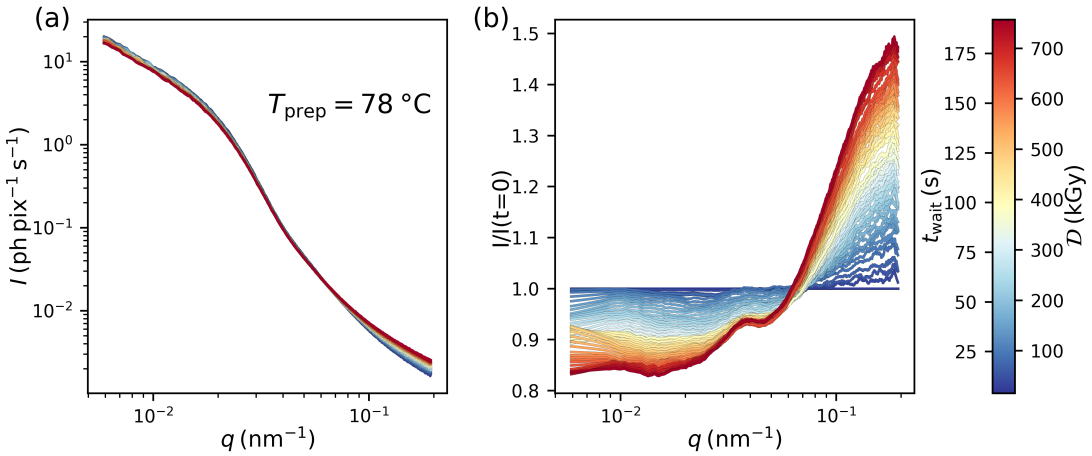

Figure 5.5: (a) Evolution of the USAXS signal under irradiation with $\mathscr{D} = 4\,\mathrm{kGy\,s^{-1}}$ for 200 s. The sample was prepared at 78 °C. (b) USAXS signal normalized to the curve at $t = 0\,\mathrm{s}$.

$q \leq 0.12\,\mathrm{nm^{-1}}$ with a loss in electron density contrast compared to the initial gel network. It seems like the radicals and the ionization of the proteins trigger a restructuring of the network, where the new structure is less capable of expelling the water. We will interpret these results further in the context of the results for the sample dynamics in section 6.3.

The effects of radiation on the structure change if we increase the preparation temperature further. Figure 5.5(a) shows the dose-induced changes on the USAXS profiles of a sample prepared at 78 °C. Compared to the $T_{\mathrm{prep}} = 53\,^{\circ}\mathrm{C}$ and 63 °C samples, the overall changes are relatively smaller and hardly visible. The normalization to the first intensity curve in panel (b) reveals that, like for the 63 °C sample, we observe an increase in intensity at high q and a decrease in intensity at low q. At the same time, the point of transition between these two regions is shifted towards lower q ($q = 0.07\,\mathrm{nm^{-1}}$) compared to the 63 °C sample. This indicates the radiation-induced formation of protein assemblies from the non-denaturated protein content, as observed already at the lower preparation temperatures. Due to the comparison of the USAXS profiles at different temperatures (Sec. 5.1) we assume that the radius of the microaggregates increases when the preparation temperature increases. This would also explain the shift of the turning point in Fig. 5.5(b) to larger length scales as we can then track the growth of the protein assemblies to larger length scales before reaching the length scale of the existing microaggregates. The initial increase in the intensity at the lowest q values, which was the third region that we identified in the 63 °C sample, is absent in the 78 °C sample. An additional feature in the normalized plot of the USAXS profiles of the 78 °C sample (Fig. 5.5(b)) is a peak around $q = 0.04\,\mathrm{nm^{-1}}$ which points towards the present of a length scale on which the egg white is less sensitive to radiation damage.

The q value of the peak is slightly above that one where the onset of the size distribution of the microaggregates disturbs the fractal behavior of the gel network. Thus, this peak could mark the size of a special microaggregate constellation that is more robust against radiation effects than the others.

We can conclude that the stability of the cooked egg white against dose effects increases with preparation temperature. To identify the reason for these differences, we need to look at the USAXS profiles of the whole set of preparation temperatures in Fig. 5.6. The normalized version of the profiles is shown in Fig. 5.7. For the samples prepared at the lowest temperatures $T_{\mathrm{prep}} < 60\,^{\circ}\mathrm{C}$, we observe the increase in intensity caused by aggregation of the not denaturated proteins. The preparation temperature of 60 °C marks a transition point. Here, the ovotransferrin protein denaturates, causing the form factor *knee* in the intensity profile. All samples prepared between 60 °C and 70 °C display the initial increase in intensity and start to degrade already after X-ray doses of a few kGy (Fig. 5.7(b)). Looking at the denaturation temperatures of the egg white proteins, these are the samples where the gel network is formed by ovotransferrin and lysozyme. At preparation temperatures above 70 °C, the samples are suddenly less susceptible to radiation effects as the overall changes in the intensity are reduced and set in at higher doses. This can be attributed to the participation of the ovalbumin protein in the formation of the gel network. Ovalbumin denaturates around 70 °C [63, 148, 149]. It is the most abundant protein in egg white and is the only one with free sulfhydryl groups that might act as agents for disulfide bridges like those observed between lysozyme and ovalbumin [152]. This increase in stability of the gel networks causes an increased resistance of the gel network structure against the effects of accumulated X-ray dose. Based on this finding, we will refer to the samples prepared at 63 °C, 65 °C, 68 °C and 70 °C as *soft gel networks* and the samples prepared at 73 °C and above as *strong gel networks*.

The peak that was observed in the normalized plot of the 78 °C sample (Fig. 5.5(b)) is also present in all other soft and strong gel networks (Fig. 5.7(b,c)). It is more pronounced at the higher preparation temperatures, where the overall changes to the structure are reduced. The q position at $0.04\,\mathrm{nm}^{-1}$ is the same regardless of the preparation temperature, which supports our thesis that there is a certain microaggregate from egg white proteins that is less susceptible to radiation damage. But clearly, measurements with other experimental techniques are required to confirm or falsify this.

We note already here that the scattered intensity for the samples without a gel network ($T_{\mathrm{prep}} \leq 60\,^{\circ}\mathrm{C}$, Fig. 5.6(a)) is not high enough to analyze the dynamics with a sufficient time resolution, at least in the current setup, as the signal to noise ratio is not high enough (see Sec. 3.5).

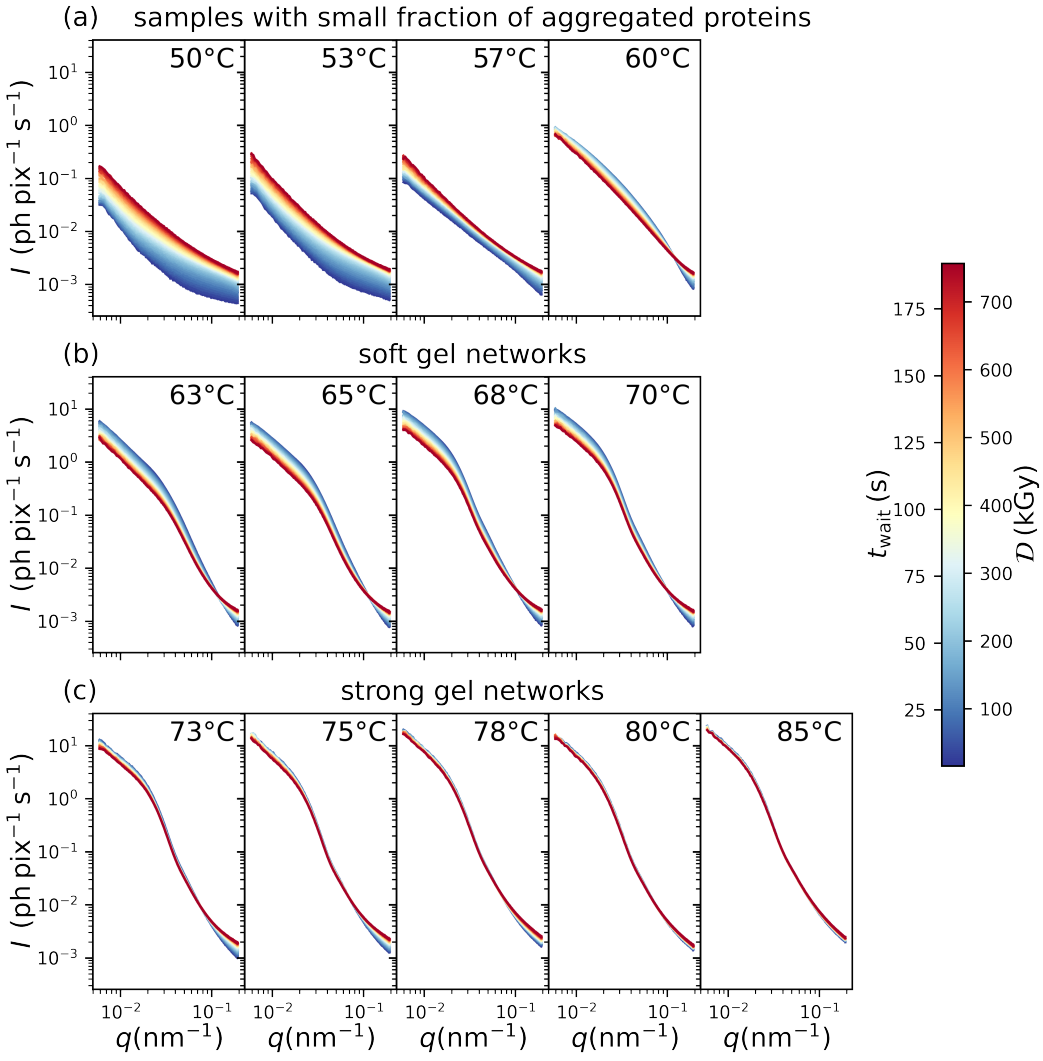

Figure 5.6: Evolution of the USAXS signal under irradiation with $\mathscr{D} = 4\,\mathrm{kGy\,s^{-1}}$ for 200 s for all preparation temperatures. (a) samples with a small fraction of aggregated proteins without a percolating gel network. (b) soft gel network with a low fraction of ovalbumin (c) strong gel network with a high fraction of ovalbumin.

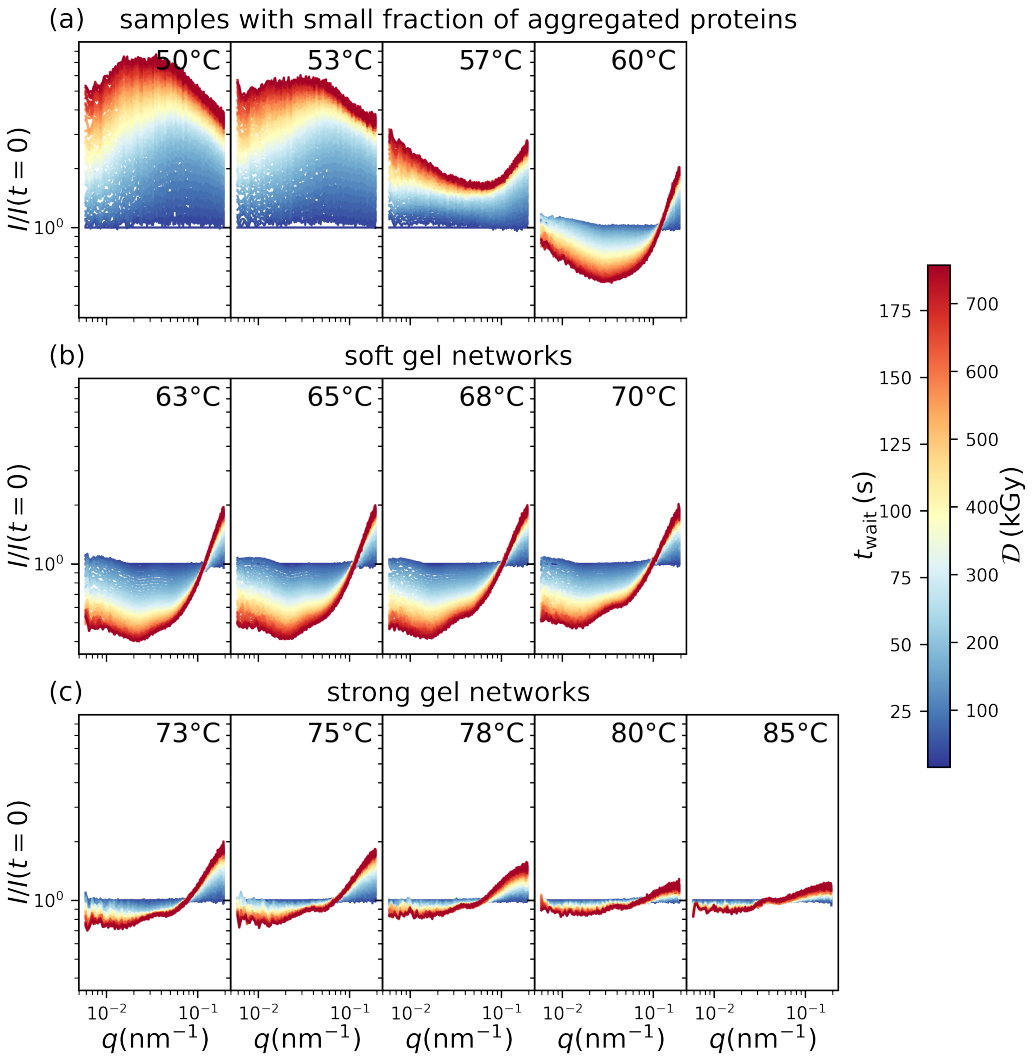

Figure 5.7: Evolution of the USAXS signal under irradiation with $\mathscr{D} = 4\,\mathrm{kGy\,s^{-1}}$ for 200 s for all preparation temperatures, normalized to the first recorded scattering profile of every series. (a) samples with a small fraction of aggregated proteins without a percolating gel network. (b) soft gel network with a low fraction of ovalbumin (c) strong gel network with a high fraction of ovalbumin.

5.3 Dose Rate Effecs

So far we investigated changes in the ultra-small angle X-ray scattering (USAXS) intensity as a function of the energy deposited in the sample, the dose $\mathcal{D}$, at different sample preparation temperatures. In this section, we will extend this study to different rates of energy deposition in the sample, the dose rate $\dot{\mathcal{D}}$. We compare the evolution of the structure at the highest dose rates $\dot{\mathcal{D}} \geq 0.3\,\mathrm{kGy\,s^{-1}}$ as a function of the dose aiming to disentangle effects of the dose and the dose rate. The four lowest dose rates are excluded here as the maximum accumulated dose during a measurement is significantly lower and thus not suitable for comparison. We focus in this study on the samples prepared above 60 °C as these are the ones where we can also gain insights on the dynamics via X-ray photon correlation spectroscopy (XPCS) later.

To facilitate a comparison of different dose rates, doses, and preparation temperatures, we aim for a condensation of the USAXS profile obtained at a specific time into a single data point. To achieve this, we calculate the mean of the azimuthally integrated intensity in the q range $0.006\,\mathrm{nm^{-1}}$ to $0.03\,\mathrm{nm^{-1}}$ and normalize this to the mean intensity at $t = 0\,\mathrm{s}$. The q range is adapted to the region where we observe the most significant changes in intensity and is also the range where the intensity is sufficient to perform an XPCS analysis. The values for I/I_0 as a function of dose and dose rate are shown in Fig. 5.8 with one panel per preparation temperature. In this representation, it is also easier to resolve the increase in intensity at low doses in the soft gel networks (Fig. 5.8(a)). The position of the maximum intensity shows a clear dose rate dependence: With increasing dose rate, the maximum shifts towards higher intensity deviations and higher doses. From this plot, we can now define thresholds for the dose via the maximum tolerable deviation in intensity from the initial intensity I_0. Reiser et al. set a threshold of 1 % relative deviation in the Porod invariant in their study on antibody proteins [26]. If we transfer this value to our mean intensity, we find dose thresholds between 3 kGy to 9 kGy for the soft gel networks almost independent of the dose rate. These values are indicated by vertical bars on the x-axis in Fig. 5.8, where the color matches the color of the corresponding dose rate $\dot{\mathcal{D}}$. It is important to note that we restricted our considerations to the length scales of the gel network. The threshold for the formation of protein assemblies with sizes of tens of nanometers might be lower.

The sample prepared at 70 °C marks a transition from soft to strong gel network: for $\dot{\mathcal{D}} < 1\,\mathrm{kGy\,s^{-1}}$ the increase in intensity is not pronounced enough to cross the 1 %-threshold which shifts the dose threshold to higher doses of 20 kGy to 40 kGy where the intensity decreases due to the opening of the gel structure. As expected from the comparison of the USAXS profiles, the changes in intensity in the strong gel networks (Fig. 5.8(b)) are smaller compared to the soft gel networks, and the increase in intensity is absent. This is reflected in the threshold values for the dose that are shifted to $\geq 30\,\mathrm{kGy}$. It is remarkable that this threshold for the strong gel networks

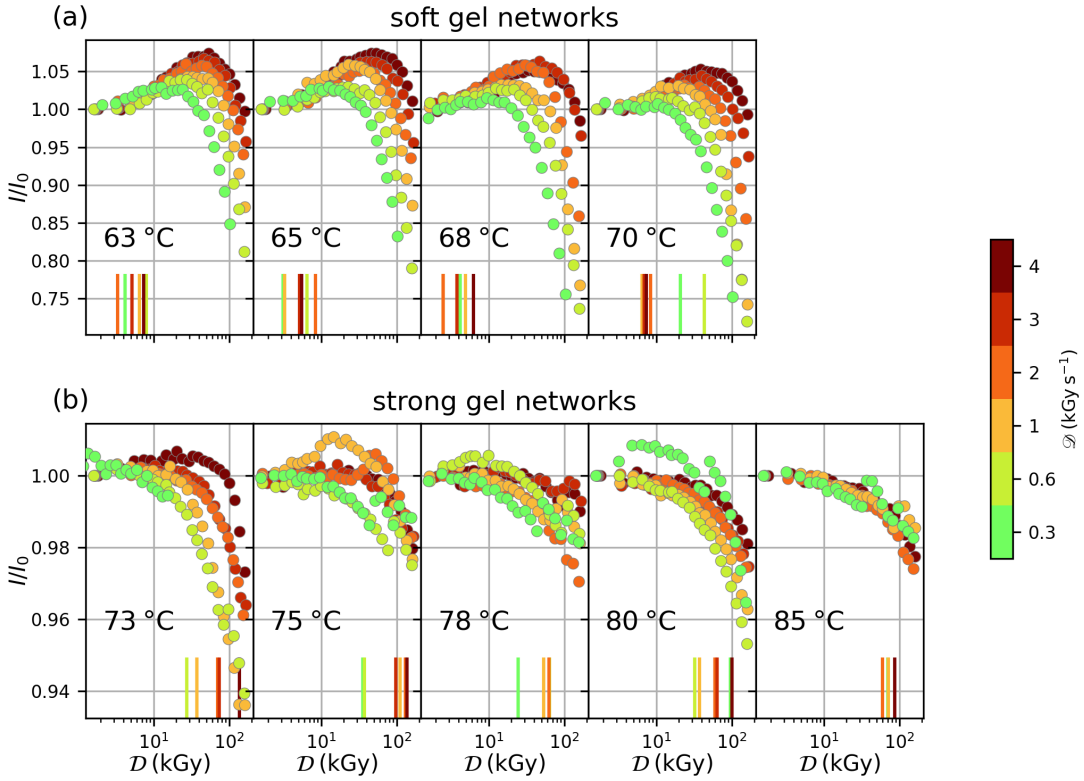

Figure 5.8: Changes in the mean scattered intensity as a function of dose (x-axis) and dose rate (color). For each data point, the azimuthally integrated USAXS intensity is averaged in the q-interval $0.006\,\mathrm{nm}^{-1}$ to $0.03\,\mathrm{nm}^{-1}$ and normalized to the intensity at the beginning of the measurement I_0. The small vertical lines close to the x-axis indicate the dose values where the deviation of relative intensity exceeds 1 %.

displays a dose rate dependence and is shifted towards higher doses with increasing dose rates. A premature conclusion of this is to recommend higher dose rates for USAXS measurements to reduce radiation effects. We will review this later in light of the XPCS results on the dynamics.

Chapter 6

Results from X-ray Photon Correlation Spectroscopy

In this chapter, we will complement the results obtained from the ultra-small angle X-ray scattering (USAXS) analysis of sample structure with an X-ray photon correlation spectroscopy (XPCS) analysis to access the sample dynamics. The underlying data are the same as used in the USAXS analysis, but instead of integrated intensities, the starting points are two-time correlation functions (TTCs) as calculated with Eq. (2.33).

We aim to disentangle the dose and dose rate effects on the dynamics. To achieve this, we start with long measurements at low dose rates on different egg white gel networks in Sec. 6.1. In the next step (Sec. 6.2), the nature of the dose rate effect is investigated via measurements with alternating dose rates on a single sample spot. Section 6.3 shows the effects of dose and dose rate on the whole set of egg white gel networks from which we can derive thresholds for the fluence/dose rate (Sec. 6.4) and the dose (Sec. 6.5). In Sec. 6.6, we will see how the sample's reaction to different dose rates changes as the time that has passed since the cooking increases to judge how significant the impact of these aging effects on the other measurements is. Finally, in Sec. 6.7, we will compare the results from three different eggs to gain insights into the reproducibility of the effects on these heterogeneous samples. This chapter is based on Ref. [261].

6.1 Dose Effects

In this section, we will extract the effect of the X-ray dose on the dynamics of egg white gels from single TTCs. The advantage of TTCs is that we can track changes in the degree of correlation of intensities related to the sample dynamics as a function of the waiting time. In conventional

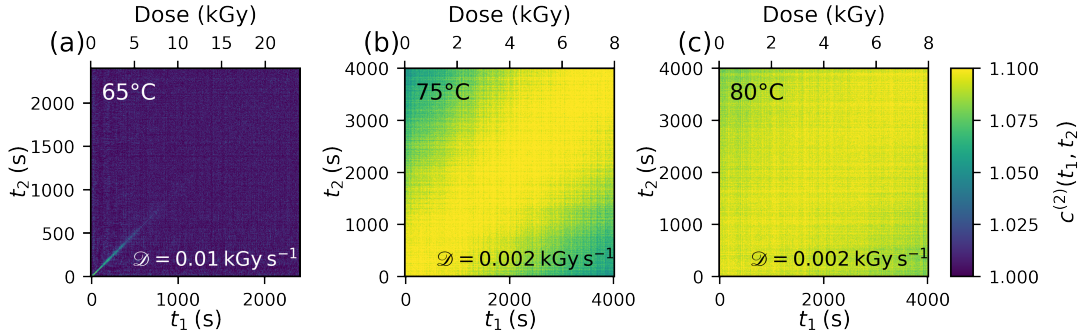

Figure 6.1: TTCs from long measurements with low dose rates on a single spot. (a) Egg white prepared at 65 °C and irradiated with $\mathscr{D} = 0.01\,\mathrm{kGy\,s^{-1}}$. The TTC is calculated at $q = 0.006\,\mathrm{nm^{-1}}$ (b) Egg white prepared at 75 °C and irradiated with $\mathscr{D} = 0.002\,\mathrm{kGy\,s^{-1}}$. The TTC is calculated at $q = 0.02\,\mathrm{nm^{-1}}$ (c) Egg white prepared at 80 °C and irradiated with $\mathscr{D} = 0.002\,\mathrm{kGy\,s^{-1}}$.The TTC is calculated at $q = 0.03\,\mathrm{nm^{-1}}$

measurements with X-rays, increasing time is associated with an increasing accumulated dose, as more energy is deposited in the sample. Thus, under a constant dose rate, we can track dose effects via the temporal changes in the TTC close to the $t_1 = t_2$ diagonal.

Figure 6.1 shows TTC from long measurements with low dose rates $\mathscr{D} \leq 0.01\,\mathrm{kGy\,s^{-1}}$ for egg white samples prepared at 65 °C, 75 °C, and 80 °C. It can be seen that the width of the TTC around the diagonal increases with increasing preparation temperature. This means that the dynamics of the sample become slower after cooking at a higher temperature due to the higher amount of denaturated proteins that add more crosslinks to the gel network.

In the sample prepared at 65 °C (Fig. 6.1(a)), we observe an acceleration of the dynamics at doses of 3 kGy to 5 kGy. In the 75 °C-sample (Fig. 6.1(b)) and the 80 °C-sample (Fig. 6.1(c)), this acceleration is absent although doses up to 8 kGy are covered. Therefore, the dynamics of the samples prepared at lower temperatures are not only faster but also more sensitive to dose effects. The last observation is in line with the conclusions from the USAXS analysis in Sec. 5.2.

In the next step, we want to extend the investigations on dose effects to higher doses on the order of 100 kGy. As shown from the axis labels in Fig. 6.1(b,c), these measurements took longer than an hour. As it is not feasible to spend half a day of beam time at a synchrotron on measuring a single TTC with a low dose rate, we will increase the dose rate significantly to investigate higher doses, keeping in mind that the effects of the dose rate might interfere with the dose effects.

The TTCs measured with the higher dose rates are shown in Fig. 6.2. The TTC of the 65 °C-sample displays a dose-induced slow-down of the dynamics, which is the opposite of the behavior observed at low doses in Fig. 6.1(a). So, there seem to be two opposing mechanisms through

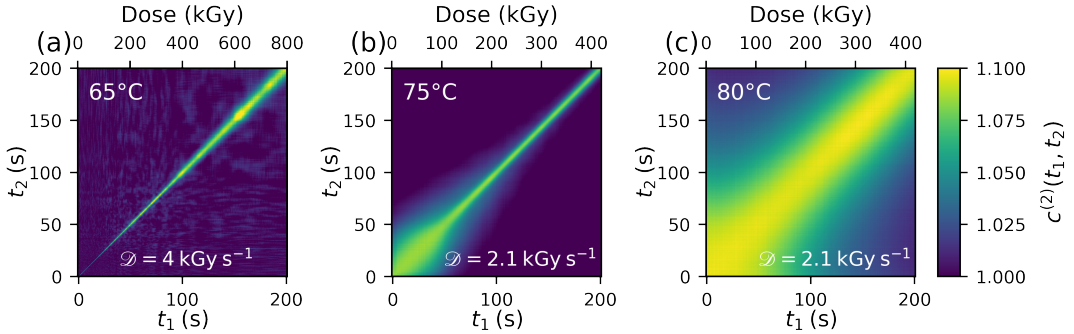

Figure 6.2: TTCs from measurements with high dose rates on a single spot. (a) Egg white prepared at 65 °C and irradiated with $\mathscr{D} = 4\,\mathrm{kGy\,s^{-1}}$. The TTC is calculated at $q = 0.006\,\mathrm{nm^{-1}}$ (b) Egg white prepared at 75 °C and irradiated with $\mathscr{D} = 2.1\,\mathrm{kGy\,s^{-1}}$. The TTC is calculated at $q = 0.02\,\mathrm{nm^{-1}}$ (c) Egg white prepared at 80 °C and irradiated with $\mathscr{D} = 2.1\,\mathrm{kGy\,s^{-1}}$.The TTC is calculated at $q = 0.02\,\mathrm{nm^{-1}}$

which the dose affects the sample dynamics: one that speeds up the sample dynamics and one that leads to a slow-down. We will investigate this further in Sec. 6.3, where the whole set of dose rates is presented.

At these high doses, the slower samples prepared at 75 °C and 80 °C show dose-induced changes in the dynamics as well. In both samples, we find an acceleration in the dynamics seen by a thinning of the TTC around the diagonal at doses around 100 kGy. These values are comparable to the thresholds we found in the USAXS analysis (Fig. 5.8). We notice that the initial width of the TTCs at low doses is already smaller than those observed in the measurements with lower dose rates 6.1(b,c). This points towards a dose-rate-induced speed-up in the sample dynamics, at least in the strong gel networks prepared at high temperatures.

We conclude that the effects of the dose on the dynamics are complex and can lead to both an acceleration and a slow-down of dynamics. In the USAXS analysis, we found that samples prepared at temperatures above 70 °C are also more stable against dose effects, probably due to the contribution of the denaturated ovalbumin. The same is true for the dynamics as dose-induced accelerations/slow-downs set in at higher doses for these strong gel networks. The dose threshold values that we derived from the TTCs are comparable to those in the USAXS analysis. There are hints for an instantaneous dose-rate-induced speed-up in the dynamics, which we will investigate further in the next section.

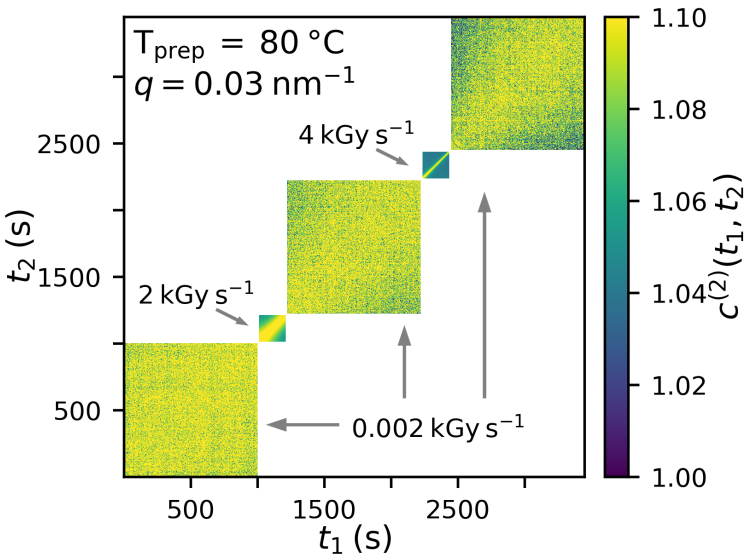

Figure 6.3: TTCs from the illumination of a single spot on an egg white sample prepared at 80 °C with changing dose rate. The corresponding values of the dose rates are indicated in the figure. The time between two TTCs is ≈ 11 s.

6.2 Dose Rate Effects

In this section, we will further investigate the nature of the dose-rate-induced acceleration of the dynamics. For this, we employ the measurement scheme described in Sec. 3.5.3 to illuminate a single sample spot with alternating X-ray fluences and, thereby, dose rates. Figure 6.3 shows the TTCs from a series where irradiations with high dose rates ($2\,\mathrm{kGy\,s^{-1}}$ to $4\,\mathrm{kGy\,s^{-1}}$) are enclosed by irradiations with a low dose rate of $0.002\,\mathrm{kGy\,s^{-1}}$. The TTC in the lower left corner displays the almost frozen-in dynamics we already encountered in Fig. 6.1(c). After switching to the higher dose rate of $2\,\mathrm{kGy\,s^{-1}}$, the dynamics are immediately accelerated, comparable to the behavior in Fig. 6.2c). However, as soon as the dose rate is reduced again, the dynamics are switching back to the almost frozen-in state from the beginning. Upon increasing to the even higher dose rate of $4\,\mathrm{kGy\,s^{-1}}$, the acceleration is even more pronounced but keeps being reversible.

This measurement was inspired by experiments on oxide glasses [56–59] where a similar acceleration of the dynamics under different fluences was observed, but at dose rates that are orders of magnitude higher. Recently, this acceleration of the dynamics was also observed in protein systems close to a glass transition [60, 295]. In all these systems, the acceleration is a linear function of the applied fluence/dose rate. To evaluate if this also holds for the egg white gels, we need to include the whole set of fluences/dose rates and quantify the acceleration by extracting

the decay rate Γ from the TTCs, which will be done in the next section.

6.3 Quantification of Dose and Dose Rate Effects

The TTCs in Sec. 6.1 and 6.2 revealed that the dose can both accelerate and slow down the sample dynamics and that the dynamics also become faster with increasing dose rate. In this section, we will further specify these findings by extracting $g^{(2)}$ cuts from the TTCs and fitting them with the Kohlrausch-Williams-Watts (KWW) type function from Eq. (2.32). A comparison of the decay rate Γ and the KWW exponent k for all dose rates and preparation temperatures will yield further insights into the pathways of radiation effects in egg white gels.

The measurements that are analyzed in this section are described in Sec. 3.5.1. To each sample in the preparation temperature range 50 °C to 85 °C we apply up to ten different dose rates between $0.002\,\mathrm{kGy\,s^{-1}}$ and $4\,\mathrm{kGy\,s^{-1}}$. From Fig. 5.1 we know that the scattered intensity increases significantly around 60 °C when the gel network forms. For the samples prepared at lower temperatures, the dynamics are also faster (Fig. 6.1), which is why XPCS measurements at low preparation temperatures with low dose rates are not feasible. This is because the exposure time needs to be short to resolve the fast dynamics and the scattered intensity is not sufficient for the required signal-to-noise ratio (SNR), at least for a single series. We will focus our investigations on the samples prepared above 60 °C as the scattering contrast is high enough to gain insights already at low dose rates.

From every TTC we extract $g^{(2)}$ functions using horizontal cuts as shown in Fig. 2.8. More details on the $g^{(2)}$ extraction are given in Sec. 4.4. Each of these $g^{(2)}$ functions is fitted with a KWW type exponential decay (Eq. (2.32)), which has three free fit parameters: the contrast β, the decay rate Γ that is the inverse of the decay time, and the KWW exponent k from which we can deduce the type of motion.

In Fig. 6.4, Γ and k are shown as a function of dose $\mathcal{D}$ and dose rate $\dot{\mathcal{D}}$ for the sample prepared at 63 °C. This sample belongs to the class of radiation-sensitive soft gel networks. At low dose rates ($\dot{\mathcal{D}} \leq 0.03\,\mathrm{kGy\,s^{-1}}$, blue points in Fig. 6.7), both fit parameters show almost no dose dependence and the points are almost overlapping at $\Gamma \approx 10^{-2}\,\mathrm{s^{-1}}$ and $k \approx 1.5$. Converting the decorrelation rate into a decorrelation time $\tau = 1/\Gamma$, we obtain $\tau = 100\,\mathrm{s}$. In the analysis of dynamics, decay times of 100 s and longer are associated with arrested states like gels and glasses [115]. At the same time, KWW exponents of 1.5 are a signature of stress-relaxation dynamics and were observed in gel and glass systems earlier [228]. At low doses and dose rates, the dynamics match the typical dynamics of a gel, as expected.

With increasing dose rate, the $\Gamma(\mathcal{D})$ curves shift towards larger values. Thus, the dose rate-induced acceleration that was observed in the strong 80 °C gel network (Fig. 6.3) is also present

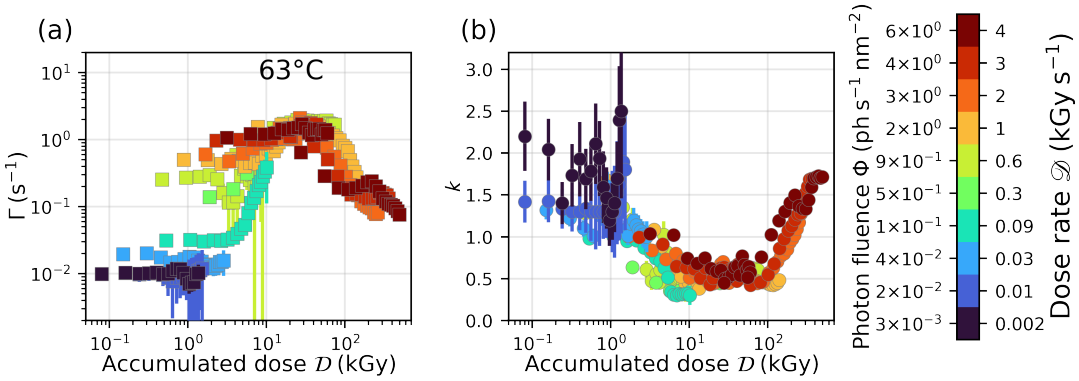

Figure 6.4: Effects of dose and dose rate effects on the decorrelation rates Γ and the KWW exponent k of egg white gel samples prepared at temperatures 63 °C. (a) Decay rates Γ as a function of the accumulated dose $\mathcal{D}$ for ten different photon fluences/dose rates indicated by different colors. (b) The corresponding values of the KWW exponent. The q-ROI was centered around $q = 0.006\,\mathrm{nm}^{-1}$.

in the soft gel networks. Besides the dose rate induced acceleration, there is also a dose-induced acceleration that can be best observed in the $\Gamma(\mathcal{D})$ curve measured with $\dot{\mathcal{D}} = 0.09\,\mathrm{kGy\,s^{-1}}$, where it sets in around 3 kGy This acceleration is also observed for the other dose rates, at least when the accumulated dose exceeds 3 kGy. But, the dose-induced acceleration sets in later for higher dose rates where the sample is already faster.

All these dose-induced accelerations in the $\Gamma(\mathcal{D})$ curves seem to fall on a single master curve with a hat-like shape that peaks around $\Gamma = 3\,\mathrm{s^{-1}}$. The combination of faster sample dynamics and a less pronounced dose-induced acceleration carries the risk of underestimating radiation effects, for example, if one tries to evaluate radiation effects based only on the $\Gamma(\mathcal{D})$ curve from the measurement with $\dot{\mathcal{D}} = 4\,\mathrm{kGy\,s^{-1}}$ (dark red points in Fig. 6.4(a)) which is almost flat up to doses of 100 kGy. We will discuss the consequences for measurements in more detail in Sec. 7.5.

While Γ increases from $0.01\,\mathrm{s^{-1}}$ to $3\,\mathrm{s^{-1}}$, the KWW exponent k drops from 1.5 to 0.5-1 (Fig. 6.4(b)). At the same time the behavior of $\Gamma(q)$ changes from a linear relation $\Gamma \propto q$ to $\Gamma \propto q^2$ (Fig. 6.5(a,b)).This indicates a transition from stress-relaxation motion towards diffusive motion. In the same dose range, we see an increase in the USAXS intensity at very small q (Fig. 5.4), which was interpreted as the formation of large structures. Together with the finding in the XPCS analysis, we can conclude that due to the accumulated dose and the thus formed radicals, the weak gel network formed by mainly the ovotransferrin is broken up into larger gel fragments that diffuse through the surrounding water-protein suspension.

At doses beyond 50 kGy, the decay rate Γ decreases as the dynamics become slower. This decrease sets in at lower doses for higher dose rates and is accompanied by an increase of the

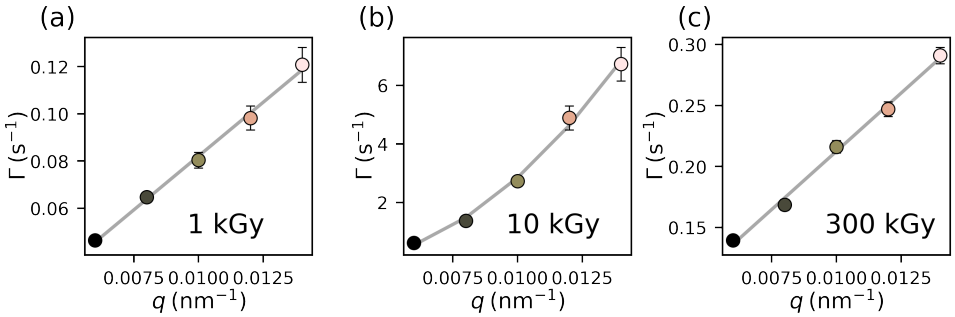

Figure 6.5: Decay rate Γ as a function of the momentum transfer q in the sample prepared at 63 °C. (a) $g^{(2)}$ cuts with an initial dose of 1 kGy, measured with $\mathscr{D} = 0.09\,\mathrm{kGy\,s^{-1}}$ and fitted with a first order polynomial. (b) $g^{(2)}$ cuts with an initial dose of 10 kGy, measured with $\mathscr{D} = 1\,\mathrm{kGy\,s^{-1}}$ and fitted with a second order polynomial. (c) $g^{(2)}$ cuts with an initial dose of 300 kGy, measured with $\mathscr{D} = 3\,\mathrm{kGy\,s^{-1}}$ and fitted with a first order polynomial.

KWW exponent towards $k = 1.5 - 2$. At the same time Γ changes from a quadratic back to a linear dependency on q (Fig. 6.5(b,c)). The sample system seems to be in a gel-like state with a ballistic type of motion as the gel fragments reconnect, slowing down the dynamics. The small aggregates formed by the non-denaturated but radiation-damaged proteins might participate in this process. At the same time, the USAXS intensity decreases at low q (Fig. 5.4). Thus, the scattering contrast of this novel gel structure is less than that of the heat-induced gel, and the capability of expelling the water from the network structure is reduced.

We repeat this analysis on a sample with a strong gel network prepared above 70 °C, which turned out to be less radiation-sensitive. Figure 6.6 shows Γ and k as a function of dose $\mathcal{D}$ and dose rate $\mathscr{D}$ for an egg white gel prepared at 73 °C. At low doses and dose rates (blue curves), we find $\Gamma = 0.01\,\mathrm{s^{-1}}$ and $k = 1.5 - 2$ which is comparable to the values of the soft gel network prepared at 63 °C. In the strong 73 °C gel network, the range of doses in which the $\Gamma(\mathcal{D})$ curves overlap is extended to dose rates as high as $0.6\,\mathrm{kGy\,s^{-1}}$. So, not only the dose threshold but also the threshold for the applicable dose rate seems to be higher compared to the soft gel network. For dose rates $\geq 1\,\mathrm{kGy\,s^{-1}}$ the decay rate Γ is systematically shifted towards faster dynamics, while the KWW exponent k stays between 1.5 and 2 throughout the whole set of doses and dose rates.

In contrast to the soft 63 °C gel network, the strong 73 °C gel network seems to stay in the gel state. In a gel system, where the motion is governed by stress relaxation events, an acceleration of the dynamics equals an increase in the rate of stress relaxation events. In our case, these additional stress relaxation events are induced by the radicals generated in the sample's water content. We will estimate radical densities that are necessary for an acceleration of the sample

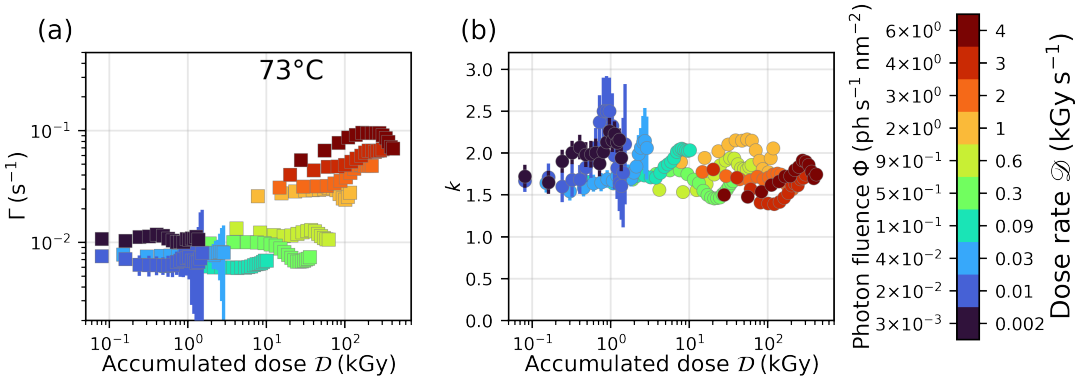

Figure 6.6: Effects of dose and dose rate effects on the decorrelation rates Γ and the KWW exponent k of the egg white gel samples prepared at temperatures 73 °C. (a) Decay rates Γ as a function of the accumulated dose $\mathcal{D}$ for ten different photon fluences/dose rates indicated by different colors. (b) The corresponding values of the KWW exponent. The q-ROI was centered around $q = 0.006\,\mathrm{nm}^{-1}$.

dynamics later in Sec. 7.2.

In the next step, we extend our analysis of the fit parameter Γ to all samples with preparation temperatures above 60 °C to see if the behavior of the 63 °C sample and the 73 °C sample are reproduced by the other soft and strong gel networks. Figure 6.7 shows the decay rate Γ as a function of dose and dose rate for the other preparation temperatures. The scattering contrast of the 60 °C sample needs to be higher to resolve the behavior at low dose rates. But for high doses and dose rates $\Gamma(\mathcal{D})$ decreases similar to the soft 63 °C gel network (Figure 6.7(a)).

All the soft gel networks with $T_{\mathrm{prep}} \in [63\,^{\circ}\mathrm{C}, 70\,^{\circ}\mathrm{C}]$ reproduce the behavior of the soft 63 °C gel network with a dose-dependent acceleration after a few kGy and a slow-down above 50 kGy to 100 kGy. This changes significantly as the sample preparation temperature changes from 70 °C to 73 °C. This is where a significant amount of the ovalbumin protein is denaturated and participates in the formation of the gel network [184]. The dynamics of these strong gel networks are also becoming slower the more ovalbumin is denaturated. To catch the decay of the $g^{(2)}$ functions better, we increased the momentum transfer q from $0.006\,\mathrm{nm}^{-1}$ to $0.02\,\mathrm{nm}^{-1}$ where the dynamics are faster as $\Gamma \propto q$. For the sample prepared at 73 °C we show the $\Gamma(\mathcal{D})$ curves for both q (Fig. 6.6(a) and Fig.6.7(f)) to demonstrate that the change in shape between 70 °C and 73 °C is not caused by the increase of q.

If the dynamics are slow, the $g^{(2)}$ function might not decay fully in the time frame covered by the measurement, especially if the $g^{(2)}$ cuts start at longer waiting times and are, therefore, shorter. This causes an increase in the error of Γ as in Fig. 6.7(g)-(i). More details on the fitting of $g^{(2)}$ functions that are not entirely decaying can be found in Sec. 4.4 and Fig. 4.6.

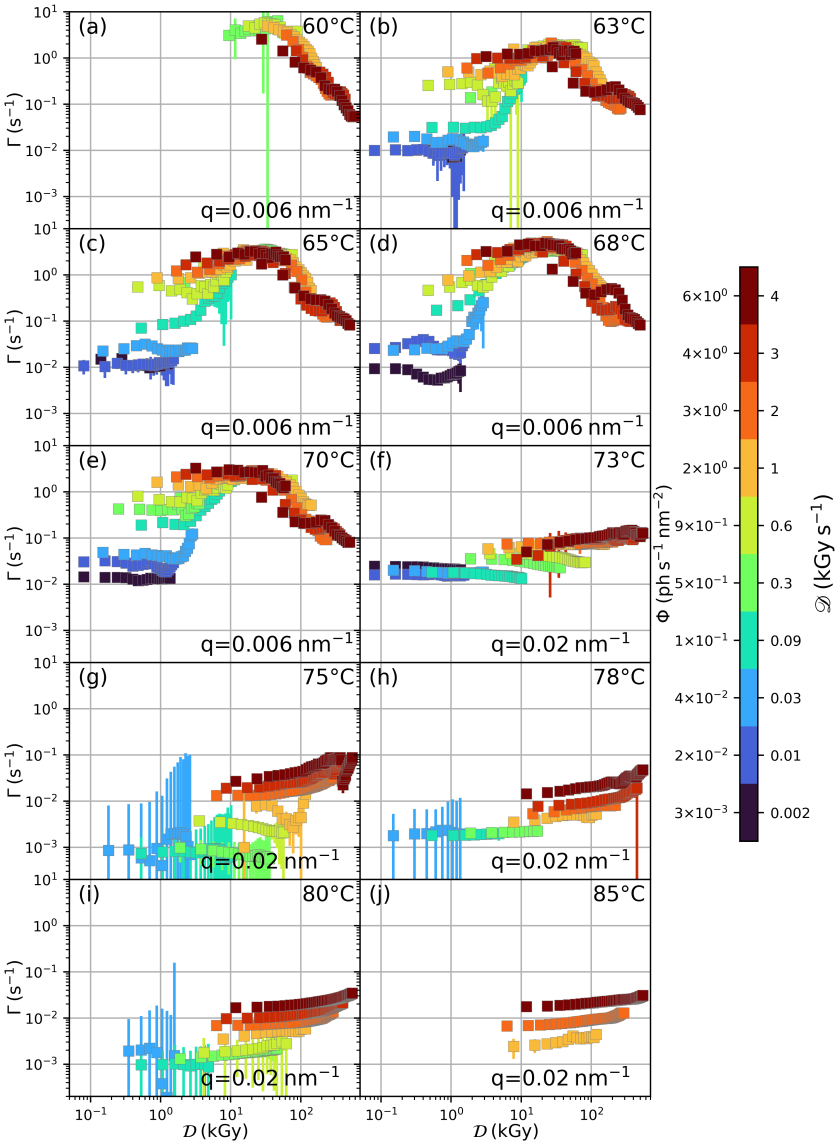

Figure 6.7: Decay rates Γ as a function of the accumulated dose for ten different fluences/dose rates indicated by color. The respective sample preparation temperature T_{prep} and the momentum transfer value q are given in the subpanels.

We conclude from this section that accumulated doses of a few kGy are sufficient to break up the soft ovalbumin network into fragments that display diffusive motion. At higher doses $\geq 50\,\mathrm{kGy}$, these fragments are reassembled into a more open gel-like structure with less scattering contrast. The stronger gel networks prepared above 70 °C, where the ovalbumin protein is also included in the gel formation, cannot be broken up by the doses and dose rates applied in this study. However, the radicals induce additional stress relaxation events that accelerate the sample dynamics of the gel network. This dose-rate-induced acceleration of the dynamics is also present in the soft gel networks. In the next section, we want to verify if the relation between sample dynamics and fluence/dose rate is linear, as it was observed in other works on oxide glasses and proteins close to a glass transition [56–60, 295].

6.4 Threshold Dose Rates for Acceleration

In this section, we want to quantify the effects of the dose rate and obtain the functional form of the connection between sample dynamics and fluence/dose rate. From Sec. 6.2 we know that an increase in the fluence/dose rate causes an instantaneous but reversible acceleration of the sample dynamics. This dose-rate induced acceleration is present in all our egg white gel networks (Fig. 6.7), and it is increasing with fluence/dose rate.

To disentangle the effect of the dose rate from the effects of the dose, we will focus on the $g^{(2)}$ cuts starting at a dose of 1 kGy. For lower doses, we might face effects of shutter opening in the data, especially at the highest dose rates where these doses are reached within the first few frames. We need to remember that a horizontal $g^{(2)}$ cut covers a specific time frame along the t_2 axis during which the accumulated dose also increases. This will be addressed in the next Sec. 6.5. For a valid comparison of the sample dynamics, we do not only need to eliminate the effect of the dose but also the effect of the different values of the momentum transfer q that we employed in the analysis of $\Gamma(\mathcal{D})$ (Fig. 6.7). Here, we can make use of the ballistic type of motion of the stress relaxations in the gel network where $\Gamma \propto q$ (Fig. 6.5(a)). The slope of $\Gamma(q)$ has units of a velocity such that we define the sample's velocity of ballistic motion v via:

$$\Gamma(q, T_{\mathrm{prep}}, \Phi) = v(T_{\mathrm{prep}}, \Phi) \cdot q. \tag{6.1}$$

This velocity of ballistic motion v depends on the preparation temperature T_{prep} and the X-ray fluence Φ and can be compared for all applied fluences and all preparation temperatures higher than 63 °C, which is shown in Fig. 6.8(a). We decided to display the curves as a function of the fluence Φ instead of the dose rate $\mathscr{D}$ to facilitate a comparison to other sample systems where fluences are not converted into dose rates.

A simple phenomenological model for the relation of sample velocity to fluence is [60]

$$v(\Phi) = v_0 + \alpha\Phi, \tag{6.2}$$

where v_0 represents the equilibrium sample velocity and α describes the strength of the X-ray-matter interaction that causes the acceleration of the dynamics. The fits with Eq. (6.2) are represented by solid lines in Fig. 6.8. The results for the fit parameters α and v_0 are shown in panes (b) and (c) of Fig. 6.8. There is a clear difference in the values of α between soft (blue markers) and strong (red markers) gel networks. For the soft gel network, the acceleration of the dynamics is stronger, and α is 100 $\mathrm{nm^3\,ph^{-1}}$. For the strong gel networks, α is three orders of magnitude smaller ($\alpha = 0.1\,\mathrm{nm^3\,ph^{-1}}$) with a decreasing trend as a function of preparation temperature.

On a double logarithmic scale as in panel (a), fits with Eq. (6.2) and a positive y-intercept v_0 display a plateau at small fluences Φ. The extent of this plateau is related to the value α such that the plateau is clearly visible for the strong gel network. For the soft gel networks, it is shifted to fluences smaller than those covered in this study. This absence of the plateau in the data for the soft gel network causes the large errorbars on the values for v_0 for the samples prepared at 63 °C and 68 °C in Fig. 6.8(c). The equilibrium velocity v_0 is approximately $1\,\mathrm{nm\,s^{-1}}$ for the soft gel networks and below $0.1\,\mathrm{nm\,s^{-1}}$ for the strong gel networks. Regarding this v_0 parameter, the sample prepared at 73 °C acts more like a soft gel network.

From the extent of the plateau, we can derive threshold values for the fluence. We define the threshold fluence Φ^* as the fluence where the radiation-induced contribution to the velocity ($\alpha\Phi^*$) exceeds the equilibrium velocity v_0, such that

$$\Phi^*(v_0, \alpha) = \frac{v_0}{\alpha}. \tag{6.3}$$

The average of Φ^* for the four soft gel networks is $\Phi^* = (0.003 \pm 0.002)\,\mathrm{ph\,s^{-1}\,nm^{-2}}$ which corresponds to a dose rate of $\mathscr{D} = (0.002 \pm 0.0013)\,\mathrm{kGy\,s^{-1}}$. In the calculation for the strong gel networks, we exclude the 73 °C sample due to the higher value of v_0 that indicates that a preparation temperature of 73 °C marks a transition from soft to strong gel network. The threshold fluence for the strong gel networks is $\Phi^* = (0.9 \pm 0.3)\,\mathrm{ph\,s^{-1}\,nm^{-2}}$ which corresponds to $\mathscr{D} = (0.6 \pm 0.2)\,\mathrm{kGy\,s^{-1}}$. These threshold fluences are indicated by vertical lines in Fig. 6.8(a).

The linear relation between sample dynamics and photon fluence that we found for the egg white samples has so far been observed in oxide, network, and protein glasses as well [56–60]. In all these systems, the type of motion is stress relaxation motion and the dependency on the photon fluence implies that the latter induces additional stress relaxation events with a rate γ that is proportional to the applied fluence via $\gamma = \alpha \cdot \Phi/\delta$.

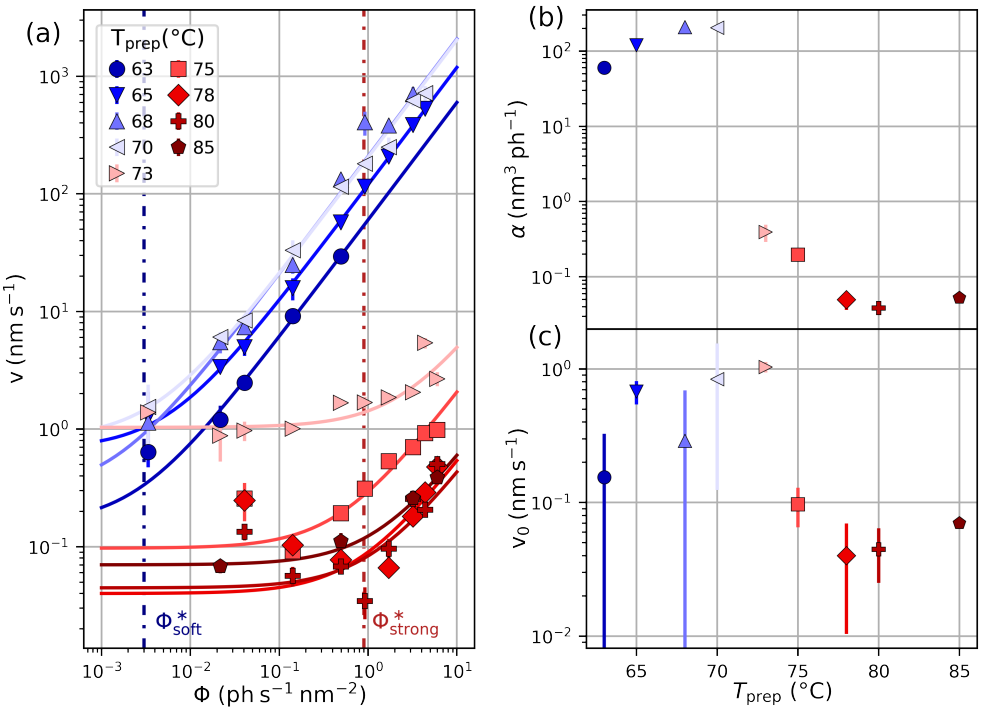

Figure 6.8: effect of fluence/dose rate on egg white samples prepared at different temperatures. (a) velocity v, as obtained from the slope of $\Gamma(q)$, as a function of the photon fluence Φ. Solid lines are fits with Eq. (6.2). Dashed vertical lines mark the fluences above which the induced velocity exceeds the intrinsic velocity. Blue dashed line: soft gel networks $T_{\mathrm{prep}} < 73\,^{\circ}\mathrm{C}$. Red dashed line: strong gel networks $T_{\mathrm{prep}} \geq 73\,^{\circ}\mathrm{C}$. (b) Fit results for the strength of the X-ray-matter interaction, which accelerates the sample dynamics a as a function of sample preparation temperature. (c) Fit results for the intrinsic velocity v_0 as a function of sample preparation temperature.

In this section, we converted the decay rates into a length scale-independent velocity v and found that it depends linearly on the applied photon fluence/dose rate. On a double logarithmic scale, this linear function displays a plateau, opening the opportunity for XPCS measurements where the measured velocity v is close to the equilibrium velocity v_0. For the strong gel network this window of opportunity extends to dose rates of $\dot{\mathscr{D}} = (0.6 \pm 0.2)\,\mathrm{kGy\,s^{-1}}$ while for the more radiation susceptible soft gel networks, it is limited to $\dot{\mathscr{D}} = (0.002 \pm 0.0013)\,\mathrm{kGy\,s^{-1}}$.

6.5 Threshold Doses for Acceleration

So far, we obtained the $g^{(2)}$ functions from horizontal cuts through the TTC and labeled them with the dose equivalent of the waiting time t_{wait} at which the cut started. The values of the data points of $g^{(2)}(\tau)$ stem from correlations of detector frames at t_{wait} and $t_1 = t_{\mathrm{wait}} + \tau$. The dose the sample has accumulated at t_1 is higher than the dose that has been accumulated up to t_{wait}. We want to consider this by looking at the doses accumulated until the time t_1 at which the $g^{(2)}$ function decays.

The starting point is Fig. 6.8, where the sample velocities are plotted as a function of the photon fluence Φ. We convert the velocities into decay times using

$$t_{\mathrm{D}} = \frac{1}{\Gamma} = \frac{1}{v \times q}. \tag{6.4}$$

We choose the momentum transfer q such that it is consistent with the analysis of the decay rates Γ in Sec. 6.3, which is $q = 0.006\,\mathrm{nm^{-1}}$ for the soft gel networks and $q = 0.02\,\mathrm{nm^{-1}}$ for the strong gel networks. Multiplication of the decay time t_{D} with the respective dose rate $\dot{\mathscr{D}}$ yields a measure for the dose $\mathcal{D}_{\mathrm{D}}$ that needs to be accumulated starting from 1 kGy such that the $g^{(2)}$ function decays to $g^{(2)}(t_{\mathrm{D}}) = 1 + \beta \exp(-2)$. The values for $\mathcal{D}_{\mathrm{D}}$ are shown in Fig. 6.9.

For the soft gel networks (Fig. 6.9(a)) the decay dose $\mathcal{D}_{\mathrm{D}}$ approaches a constant value for $\Phi \geq 2\,\mathrm{ph\,s^{-1}\,nm^{-2}}$. This means that beyond these fluences, the $g^{(2)}$ decays always at the same dose that we will label as $\mathcal{D}_{\mathrm{max}}$. Adding the 1 kGy from where the $g^{(2)}$ cuts start, we find $\mathcal{D}_{\mathrm{max}} \approx 1.5 - 3\,\mathrm{kGy}$. These values are thresholds for the dose beyond which time of the decorrelation of the $g^{(2)}$ function is given by the time where the sample reaches the dose threshold $\mathcal{D}_{\mathrm{max}}$. Moreover, this time depends on the applied dose rate, such that for high dose rates, the dose threshold $\mathcal{D}_{\mathrm{max}}$ is reached at earlier times t_{D}, so the $g^{(2)}$ function decays at earlier times and the sample is faster. As a consequence, the dose rate-induced acceleration can be translated into a dose effect.

This becomes even clearer if we compare TTCs from different dose rates cropped to the same dose range. Figure 6.10 shows TTCs from the sample prepared at 63 °C that were recorded with $0.03\,\mathrm{kGy\,s^{-1}}$, $0.3\,\mathrm{kGy\,s^{-1}}$, and $1.1\,\mathrm{kGy\,s^{-1}}$. All of them are cropped to the same range in terms

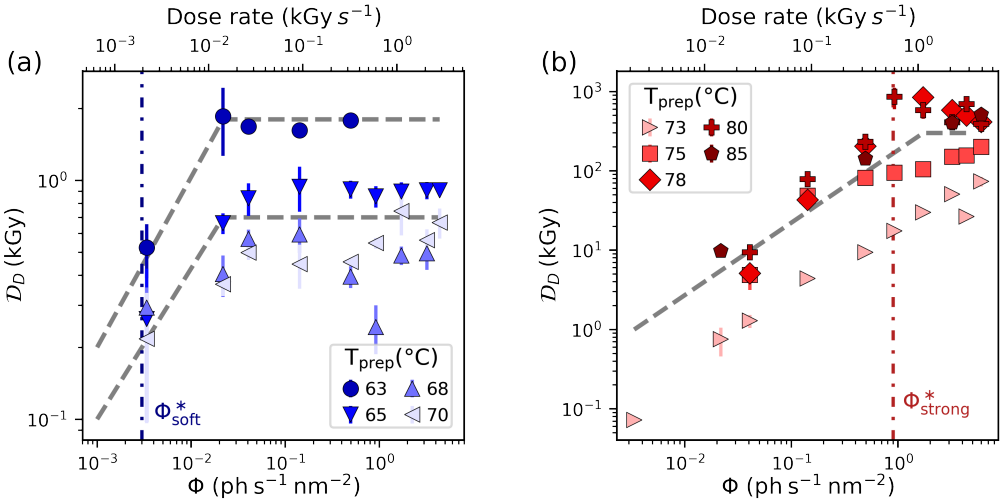

Figure 6.9: Dose equivalents $\mathcal{D}_\mathrm{D}$ of the time at which the 1 kGy-$g^{(2)}$ cuts decay to a value of $g^{(2)}(t_\mathrm{D}) = 1 + \beta \exp(-2)$. . Dashed vertical lines mark the fluences thresholds from Fig. 6.8. Gray dashed lines are guides to the eye. (a) Soft gel networks prepared below 73 °C. We assume here $q = 0.006\,\mathrm{nm}^{-1}$. (b) Strong gel networks prepared at 73 °C and above where we assume $q = 0.02\,\mathrm{nm}^{-1}$.

of accumulated dose, which is 0 kGy to 5 kGy. Although the time axes are completely different from each other, the width and the thinning of the TTC at the end are the same for all three. So, if we exceed certain thresholds, the dose determines the shape of the TTC, but what we measure as a function of time depends on the dose rate.

The equilibrium dynamics of the sample can be obtained as long as the $g^{(2)}$ function decays before t_D. The time frame of opportunity t_D depends on the one hand on the maximum tolerable dose $\mathcal{D}_\mathrm{max}$ which depends on the sample and on the other hand on the applied dose rate $\dot{\mathcal{D}}$. In Fig. 6.9, the fluence/dose rate thresholds from Fig. 6.8 are given, where the induced dynamics are as large as the intrinsic dynamics. The positions of these fluence/dose rate thresholds are well before the onset of the plateau, which confirms our definition of Φ^* above.

If the time scale of the intrinsic dynamics $1/\Gamma$ of a sample is known roughly, for example, from other measurement techniques or theoretical considerations, the dose rate threshold can be estimated without taking long measurement series with different dose rates and subsequent fitting of Eq. (6.2). $\mathcal{D}_\mathrm{max}$ can be obtained from a few measurements with high dose rates where radiation effects definitely induce the decorrelation. Together with the decay rate Γ, the threshold for the dose rate can be estimated via $\dot{\mathcal{D}}^* = \Gamma \times \mathcal{D}_\mathrm{max}$ which can be converted into fluences via Eq. (2.55).

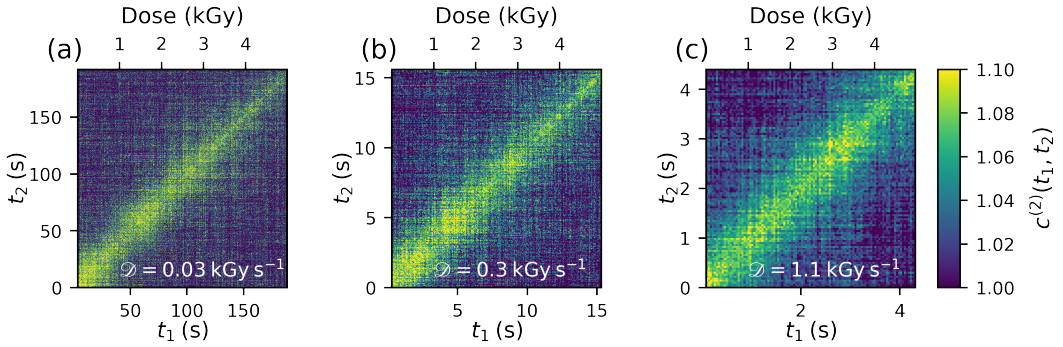

Figure 6.10: TTCs from measurements on a sample prepared at 63 °C with dose rates of (a) 0.03 kGy s^{-1}, (b) 0.3 kGy s^{-1},(c) 1.1 kGy s^{-1}. The TTCs are cropped such that the displayed time range equals an exposition to a dose of 5 kGy. For all TTCs the momentum transfer q is 0.006 nm^{-1}.

For our soft gel networks (Fig. 6.9(a)), the maximum tolerable doses $\mathcal{D}_{\max}$ are between 1.5 kGy and 3 kGy. This is slightly below the dose thresholds that we defined in the analysis of structural changes via a deviation of 1 % in the mean USAXS intensity in Fig. 5.8. The strong gel networks (Fig. 6.9(b)) require doses that are two orders of magnitude higher ($\mathcal{D}$ = 70 kGy to 300 kGy) to be fully decorrelated by radiation effects. Here, the analysis of structural changes resulted in thresholds as low as 20 kGy (at dose rates of 0.3 kGy s^{-1}). In addition, we observe a dose rate dependence of the dose thresholds found in the analysis of the structural changes, where the thresholds are higher ($\approx$ 100 kGy) for the highest dose rates $\geq$ 2 kGy s^{-1}. From this, we can conclude that in the fluence regime where beam effects entirely decorrelate the $g^{(2)}$ functions, the dose threshold values obtained from the analysis of the structural changes match those from the analysis of the dose rate-dependent dynamics. For dose rates below this regime of driven dynamics, the structural changes seem to set in at lower doses. These discussions on the mutual effects of radiation-induced changes in structure and dynamics will be continued in Sec. 7.4.

6.6 Aging Effects

Gels and glasses are arrested states far from equilibrium and display very slow relaxations towards equilibrium [215, 222, 296]. Thus, we need to investigate the time scale of these aging phenomena in cooked egg white to judge how these effects might interfere with changes in the dynamics that are observed due to changes of the X-ray fluence. The measurement procedure is described in Sec. 3.5.4, where we compare repetitions of measurements with varying fluences on the time scale of minutes to several hours.

The TTCs from these measurements on a soft egg white gel network prepared at 70 °C are shown in Fig. 6.11. The eggs are the ones from data set one and are prepared with 50 mM NaCl. Details on the effect of sodium chloride on the dynamics of gelled egg white can be found in the work of Begam et al. [55]. The TTCs in Fig. 6.11 display a similar behavior as the egg white gels from data set three presented in Sec. 6.3: The dynamics become faster with increasing dose rate, small doses like those accumulated during the scans with $\leq 0.3\,\mathrm{kGy}$ accelerate the dynamics while large doses slow them down. These effects of the dose and the dose rate are also preserved in the repetitions after 3.7 h and 5.9 h, but the equilibrium dynamics become slightly faster, and the dose-induced slow-down is less pronounced in the 5.9 h scan. Comparing the first scans to those after 3 min and 6 min, there are almost no differences.

The TTCs recorded on a strong egg white gel network (Fig. 6.12) also look similar on a time scale of minutes, except for the very first TTC that is recorded. There the dynamics are much faster in the beginning and relax during the 140 s of the measurement towards the level of dynamics that is also observed in the second and third repetition. This fast relaxation process in the very first measurement on a strong gel network has been observed several times during other measurements on egg white, and the origin of this behavior has not been discovered so far. Maybe the very first radicals that are created under X-ray illumination trigger more global stress relaxations in the sample.

Comparing the TTCs in the left columns to those recorded after 2.8 h and 5.3 h, we see that the TTCs at $\mathscr{D} \leq 0.3\,\mathrm{kGy\,s^{-1}}$ show almost frozen-in dynamics. So, the aging of the gel plays a role on the time scale of hours. The initial faster dynamics are also present in the TTCs recorded with $\mathscr{D} = 0.03\,\mathrm{kGy\,s^{-1}}$.

From these measurements, we can conclude that the egg white gels look almost homogeneous under the $100\,\mu\mathrm{m} \times 100\,\mu\mathrm{m}$ beam as TTCs from neighboring spots display very similar dynamics. In addition, aging effects are negligible on the time scale of several minutes, which is the typical duration of a standard measurement with varying fluences. However, the strong gel networks age with time, and the dynamics are significantly slower after several hours.

6.7 Reproducibility

We measured fluence-dependent dynamics on egg white samples prepared from three different eggs and at three different beam times, all in the same USAXS geometry. The data sets are listed in table 3.2 and differ in the cooking setup (Linkam stage or water bath) and concentration of sodium chloride (50 mM or 0 mM). The egg white samples from data sets two and three were prepared similarly (0 mM NaCl, water bath cooking), so we would expect similar behavior under varying fluences.

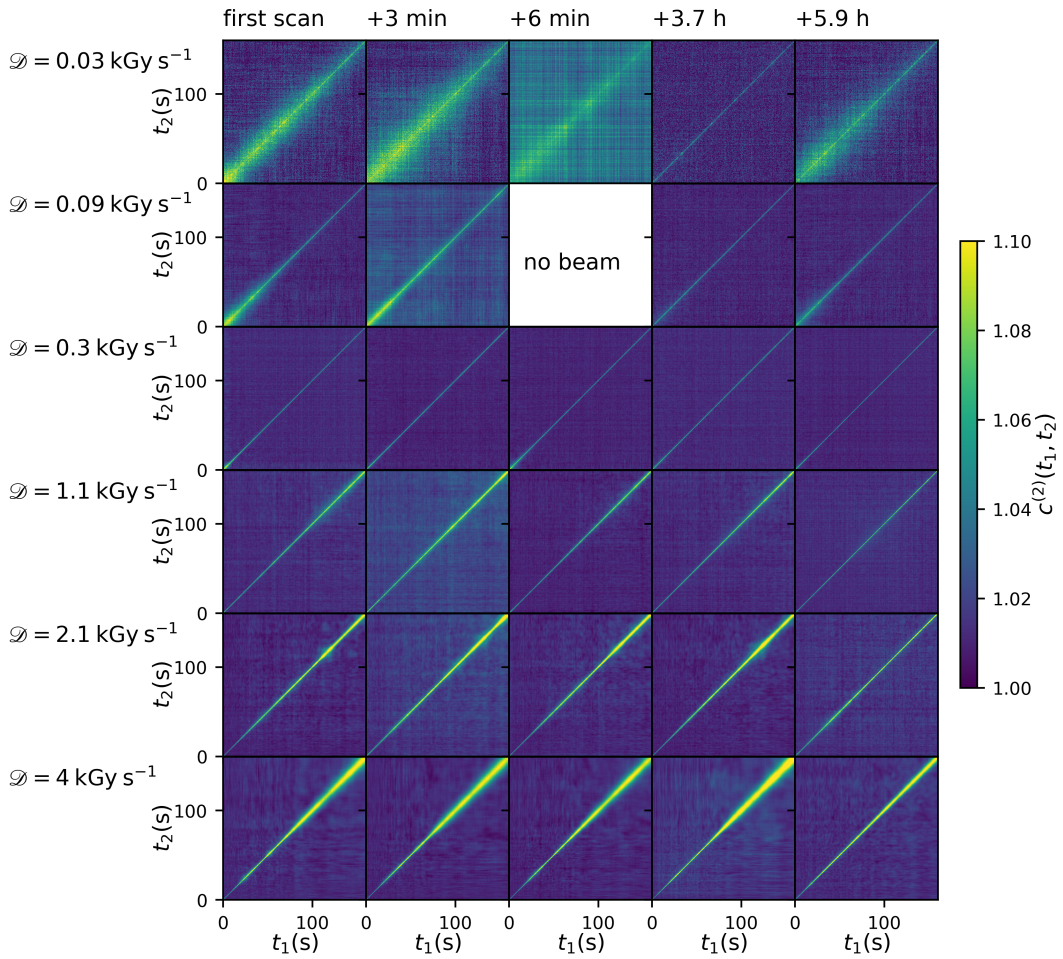

Figure 6.11: Aging effects in an egg white sample prepared at 70 °C. The first scan was performed 12 min after the end of the cooking. The spots on the sample for the first three scans were 200 nm apart. The capillary was reinserted into the Linkam stage for measurements four and five. The egg belongs to data set one.

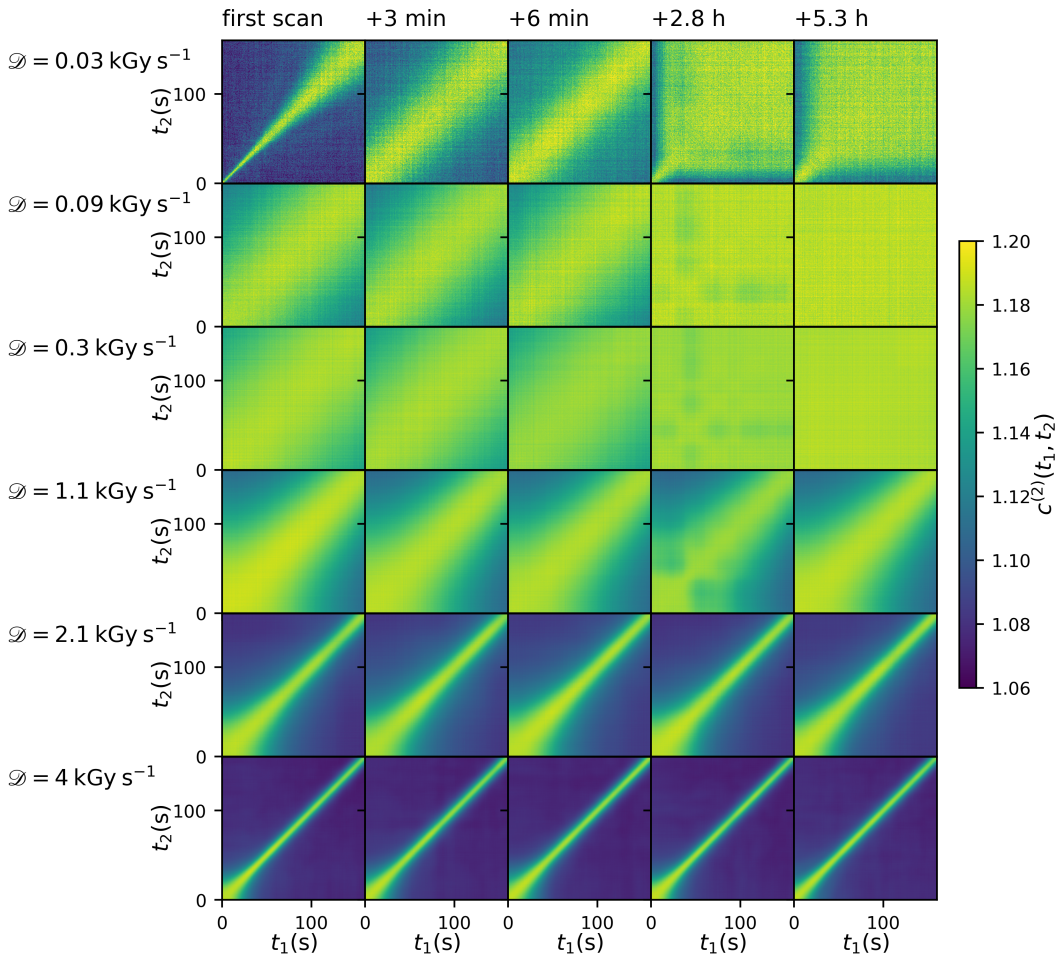

Figure 6.12: Aging effects in an egg white sample prepared at 80 °C. The first scan was performed 12 min after the end of the cooking. The spots on the sample for the first three scans were 200 nm apart.The capillary was reinserted into the Linkam stage for measurements four and five. The egg belongs to data set one.

We compare plots of the decay rate as a function of dose and dose rate $\Gamma(\mathcal{D}, \dot{\mathcal{D}})$ and the sample velocity as a function of the fluence $v(\Phi)$ for the three different eggs, once prepared at 70 °C (Fig. 6.13) once prepared at 75 °C (Fig. 6.14)

The sample from data set three (egg three) is the one known from the analysis in Sec. 6.3, where the dynamics are accelerated at low doses and slowed down at high doses. Although egg one has been cooked in the Linkam stage instead of the water bath and has 50 mM of sodium chloride, the shape of $\Gamma(\mathcal{D}, \dot{\mathcal{D}})$ is very similar with overlapping rising and falling edges. Egg two has been prepared in the same way as egg three, but the shape of $\Gamma(\mathcal{D}, \dot{\mathcal{D}})$ differs significantly from the other two samples: It does not display the typical hat-shaped master curve of $\Gamma(\mathcal{D})$ and the dose rate dependence of Γ is less pronounced, and is closer to the one of a typical strong gel network.

This can also be seen from the $v(\Phi)$ curves in Fig. 6.13(b). The data points are fitted with $v = v_0 + \alpha\Phi$ (Eq. (6.2)), and the result for the results for the fit parameters α and v_0 are shown in the inset figure. Again, the data points of eggs one and three are close together, but for egg one, we are missing the measurements with the lowest fluences, which reduces the precision of the equilibrium velocity v_0. The equilibrium velocities of eggs two and three match very well ($v_0 \approx 1\,\mathrm{nm\,s^{-1}}$), while α is almost two orders of magnitude smaller, indicating that the sample prepared from egg two is less susceptible to the dose-rate induced acceleration.

Samples from the same three eggs were prepared at 75 °C as well, with the results shown in Fig. 6.14. Although the shapes of the $\Gamma(\mathcal{D}, \dot{\mathcal{D}})$ curves are very similar with a plateau up to doses of tens of kGy, the absolute values differ by up to two orders of magnitude. The sample from egg one prepared in the Linkam stage is fastest with $\Gamma \approx 0.1\,\mathrm{s^{-1}}$. This sample was measured $\approx 10\,\mathrm{min}$ after the end of the cooking procedure. For egg two and three about 45 min passed between cooking and measurement of $\Gamma(\mathcal{D}, \dot{\mathcal{D}})$. In the last Sec. 6.6, we found that strong gels are aging, i.e., the dynamics become slower with time. This might be the source of the huge differences in dynamics between egg one and the other two samples. The dynamics of strong gel networks are also affected by the age of the egg itself. Upon storing, the ovalbumin content in the egg white transforms into the more heat-stable S-ovalbumin [149, 154, 155]. Thus, in an old egg, we expect the dynamics to be faster due to the lower fraction of heat-denaturated (S-)ovalbumin.

The $v(\Phi)$ curves in Fig. 6.14(b) can be well described by $v = v_0 + \alpha\Phi$ (solid lines) and the resulting values of α are of the same order of magnitude. For the sample prepared from egg one, the relation between fluence Φ and sample velocity v is not apparent, as we are missing a rising edge for the linear fit. Maybe the sample is more radiation-stable as the sample from egg two prepared at 70 °C above such that the dose-rate induced acceleration is shifted to even higher fluences.

We conclude from this section that there are differences in the dynamics of samples prepared from different eggs that different protein compositions in the egg might cause. This can also shift

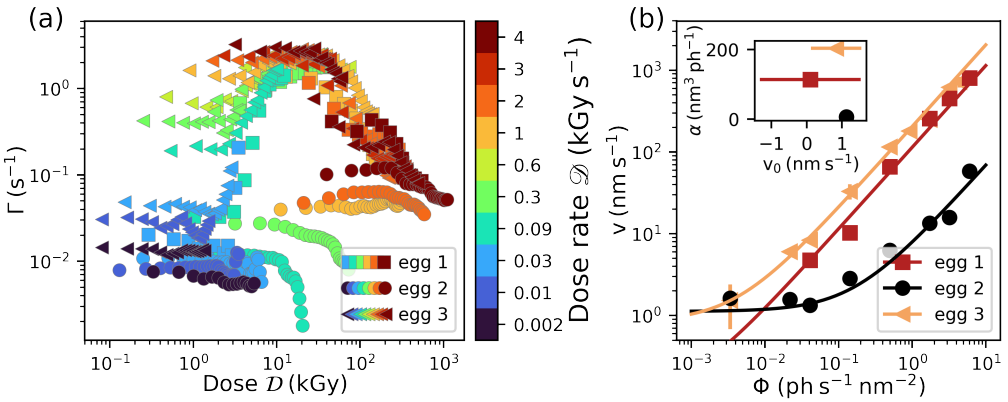

Figure 6.13: Reproducibility of results of egg white prepared at 70 °C. (a) Decay rate Γ as a function of accumulated dose for different dose rates indicated by color. The shape of the marker distinguishes the different eggs. All data were analyzed at $q = 0.006\,\mathrm{nm}^{-1}$. (b) Velocity obtained from the TTC cut at 1 kGy for different fluences on the three eggs. Solid lines are fits with Eq. (6.2). The results for the fit parameters α and v_0 are plotted in the inset figure.

the temperature where the radiation response of the egg white gel network changes from soft network-like to strong network-like as in egg two, the 70 °C sample behaves already like a strong gel network, which was observed at higher temperatures in the other two eggs. To clarify this, more measurements in the temperature range 67 °C to 73 °C on different eggs, in the best case with known time, since the laying of the egg, are necessary.

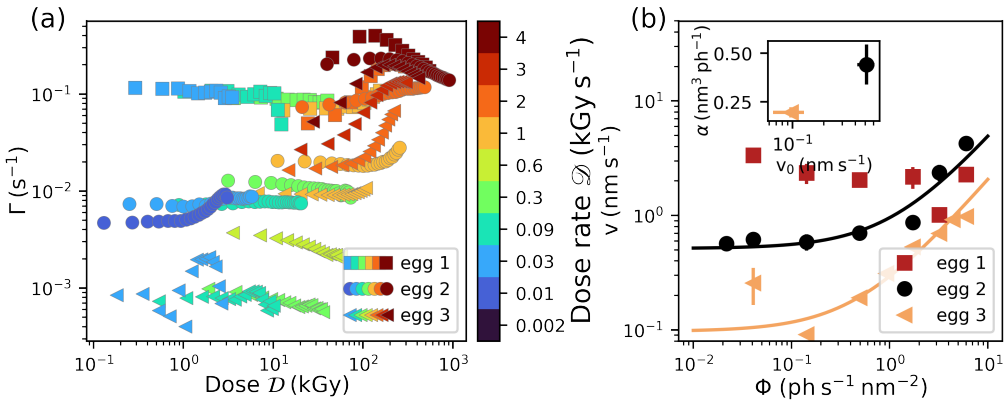

Figure 6.14: Reproducibility of results of egg white prepared at 75 °C. (a) Decay rate Γ as a function of accumulated dose for different dose rates indicated by color. The shape of the marker distinguishes the different eggs. All data were analyzed at $q = 0.02\,\mathrm{nm}^{-1}$. (b) Velocity obtained from the TTC cut at 1 kGy for different fluences on the three eggs. Solid lines are fits with Eq. (6.2). The results for the fit parameters α and v_0 are plotted in the inset figure. The data from e

Chapter 7

Discussion

This chapter discusses the results in the context of existing theoretical and experimental works. In Sec. 7.1, we recall the random walk model for gel dynamics and derive rates for the microscopic stress relaxation events. Section 7.2 presents calculations to estimate radical densities required to drive the dynamics of cooked egg white with X-ray radiation. The radiation-induced acceleration observed in our system will be compared to those observed in other gel/glass systems in Sec. 7.3. In Sec. 7.4, we compare our results from ultra-small angle X-ray scattering (USAXS) and X-ray photon correlation spectroscopy (XPCS) before we derive recommendations for future XPCS experiments in Sec. 7.5.

7.1 Dose Rate-induced Stress Relaxations

The results on radiation-induced dynamics can be interpreted in light of the stress relaxation dynamics model introduced in section 2.2.4.2. The model describes a series of consecutive relaxation events that occur with a rate γ and cause displacements with an average step size δ [65, 228]. We fitted the correlation functions from this model with a Kohlrausch-Williams-Watts (KWW) expression (Eq. (2.32)). The parameter Γ fitted to these modeled correlation functions displays the same ballistic behavior that is observed in the egg white gels $\Gamma \propto q$, and the result for the KWW exponent k matches our observations of compressed $g^{(2)}$ functions with $k > 1$.

In section 2.2.4.2, the $g^{(2)}$ functions are modeled as a function of the product of momentum transfer q and step size δ (Fig. 2.9). The value that matches our observation of $k \approx 1.5 - 2$ best is $q\delta \approx 10^{-2} - 10^{-1}$. At small values of $q\delta$, the relation

$$\Gamma \approx \gamma q \delta \tag{7.1}$$

holds. From our modeling in Fig. 2.9(c) we derive that $q\delta \approx 10^{-2} - 10^{-1}$ is sufficiently small to use Eq. (7.1). With that, we can connect the macroscopic decorrelation rate Γ to the microscopic relaxation rate γ. Inserting $q\delta \approx 10^{-2}$–10^{-1} into Eq. (7.1) yields that the microscopic relaxation rate γ is one to two orders of magnitude larger than the decorrelation rate of the $g^{(2)}$ function Γ. In the analysis of the dynamics of egg white gels we typically encounter values of $\Gamma \approx 0.1\,\mathrm{s}^{-1}$ at a momentum transfer $q = 0.006\,\mathrm{nm}^{-1}$ (e.g. 63 °C sample in Fig. 6.4). To reach $q\delta \approx 10^{-2}$–10^{-1}, average step sizes of $\delta \approx 1\,\mathrm{nm}$ to 15 nm are necessary, which is small compared to the size of the micro-aggregates that is about 200 nm. The rate of these micro-relaxations is $\gamma = \Gamma/q\delta$, which is $1\,\mathrm{s}^{-1}$ to $10\,\mathrm{s}^{-1}$ in a state close to equilibrium with minimum radiation effects.

In Sec. 6.4 we found that the sample velocity $v = \Gamma/q$ is a linear function of the fluence Φ:

$$v = \frac{\Gamma}{q} = v_0 + \alpha\Phi. \tag{7.2}$$

From Eq. (7.1), we know that this velocity v can be interpreted within the stress relaxation model as the product of the rate of microscopic relaxations γ and the average step size δ. Using this together with Eq. (7.2), the rate of induced microscopic relaxation events $\gamma\prime$ becomes:

$$\gamma\prime = \frac{\alpha\Phi}{\delta}. \tag{7.3}$$

Again, we specify this for a typical soft gel network with $\alpha = 100\,\mathrm{nm}^3\,\mathrm{ph}^{-1}$ using $\delta \approx 10\,\mathrm{nm}$, which is in the range derived above. The fluences that we applied in the experiments are in the range 10^{-3}–$10^{1}\,\mathrm{ph\,s^{-1}\,nm^{-2}}$. Using Eq. (7.3), we find that the rate of radiation-induced microscopic events $\gamma\prime$ increases from $10^{-2}\,\mathrm{s}^{-1}$ to $10^{2}\,\mathrm{s}^{-1}$.

We assume that these additional stress relaxation events are triggered by radicals generated in the sample. In the next section, we will estimate radical generation rates.

7.2 Estimations of Radical Rates

If ionizing radiation impinges, e.g., on water, highly reactive chemical species are generated, the so-called radicals (sec. 2.3.4). An energy 100 eV deposited in water by X-ray photons typically causes the formation of two to three radicals [49, 246, 247] on time scales below microseconds. Using this value, we will estimate radical formation rates as a function of the fluence Φ with particular emphasis on the radical formation rate at the fluence threshold Φ^*.

In the first step we calculate the energy absorption rate R_E in our sample volume $V = A_{\mathrm{beam}} \cdot z$ where A_{beam} is the irradiated area given by the beam size ($A_{\mathrm{beam}} = 100\,\mu\mathrm{m} \times 100\,\mu\mathrm{m}$) and z is the sample thickness given by the diameter of the quartz capillaries ($z = 1.5\,\mathrm{mm}$). The attenuation of 1.5 mm of water is $(1-T) = 72.2\,\%$. Combining these values with the energy of a single photon

$E_{\mathrm{ph}} = 8.54\,\mathrm{keV}$ we find:

$$R_E(\Phi) = \Phi \cdot (1-T) \cdot A \cdot E_{\mathrm{ph}} \tag{7.4}$$

$$\Leftrightarrow R_E(\Phi)\left[\frac{\mathrm{eV}}{\mathrm{s}}\right] = 6.1 \times 10^{13} \frac{\mathrm{nm^2\,eV}}{\mathrm{ph}} \cdot \Phi\left[\frac{\mathrm{ph}}{\mathrm{s\,nm^2}}\right]. \tag{7.5}$$

We assume that absorption of 100 eV triggers, on average, the generation of three radicals such that the radical formation rate R_{r} becomes

$$R_{\mathrm{r}}\left[\frac{\mathrm{radicals}}{\mathrm{s}}\right] = R_E(\Phi)\left[\frac{\mathrm{eV}}{\mathrm{s}}\right] \cdot \frac{3\,\mathrm{radicals}}{100\,\mathrm{eV}} \tag{7.6}$$

$$= 1.8 \times 10^{12} \frac{\mathrm{nm^2\,radicals}}{\mathrm{ph}} \cdot \Phi\left[\frac{\mathrm{ph}}{\mathrm{s\,nm^2}}\right]. \tag{7.7}$$

Normalization to the irradiated volume V yields the radical formation rate density

$$r_{\mathrm{r}}\left[\frac{\mathrm{radicals}}{\mathrm{s\,nm^3}}\right] = \frac{1}{V} \cdot R_{\mathrm{r}}\left[\frac{\mathrm{radicals}}{\mathrm{s}}\right] \tag{7.8}$$

$$= 1.2 \times 10^{-4} \frac{\mathrm{radicals}}{\mathrm{ph\,nm}} \cdot \Phi\left[\frac{\mathrm{ph}}{\mathrm{s\,nm^2}}\right]. \tag{7.9}$$

We can evaluate this radical formation rate at different fluences and integrate it over varying accumulation times to get an idea of the radical densities that are necessary to trigger certain radiation effects in the egg white gel networks. The fluences applied in this study are in the range 10^{-3}–$10^{1}\,\mathrm{ph\,s^{-1}\,nm^{-2}}$ which can be translated into radical formation rates of 1.2×10^{-7}–$1.2 \times 10^{-3}\,\mathrm{radicals\,s^{-1}\,nm^{-3}}$ using Eq. (7.8).

In the following, we calculate the radical density at the threshold fluences Φ^* found in Sec. 6.4. These thresholds where the acceleration of the dynamics by radiation effects is 100 % are $\Phi^*_{\mathrm{soft}} = (0.003 \pm 0.002)\,\mathrm{ph\,s^{-1}\,nm^{-2}}$ for a typical soft gel network and $\Phi^*_{\mathrm{strong}} = (0.9 \pm 0.3)\,\mathrm{ph\,s^{-1}\,nm^{-2}}$ for a typical strong gel network. These values correspond to radical formation rates of $r_{\mathrm{r,soft}} = (4 \pm 2) \times 10^{-7}\mathrm{radicals\,s^{-1}\,nm^{-3}}$ and $r_{\mathrm{r,strong}} = (11 \pm 4) \times 10^{-5}\mathrm{radicals\,s^{-1}\,nm^{-3}}$. In section 6.2, we found that switching the fluence affects the dynamics instantaneously on the time scales that we can resolve in the XPCS experiments. Suppose we integrate the radical formation rates over these minimum resolution times. In that case, we get an estimation for the radical density that is necessary to drive the sample dynamics in a soft and strong egg-white gel network. We consider here the time resolution of the measurements that were performed closest to the fluence Φ^*. In the case of the soft gel networks, these were the measurements with abs. 24 with an exposure time of 0.5 s per frame. But due to the low fluence, we need to average $g^{(2)}$ cuts that span $\approx 50\,\mathrm{s}$ in the t_2 direction (more details on $g^{(2)}$ processing in section 4.4). If we integrate the radical

formation rate $r_{\mathrm{r,soft}}$ over the time resolution of 50 s, we find a density of one radical per cube with an edge length of 40 nm. This is an upper limit for the radical density given by the time resolution of dynamics in the experiment. The actual radical density that is sufficient to drive the dynamics in a soft gel network might be even lower.

In a strong gel network, a measurement with abs. 6 matches the fluence at the threshold Φ^*. Due to the higher fluence and the larger scattering contrast of the strong gel networks, the time resolution improves to $\approx 2\,\mathrm{s}$. After 2 s of measurement with Φ^*, the strong gel network has accumulated on average one radical per cube of 20 nm edge length. The length scales of the radical densities match those of the spatial extension of the decorrelation events in egg-white [54].

7.3 Other Systems Accelerated by Fluence

Linear relations between X-ray fluence and sample dynamics have already been observed in XPCS results from other sample systems. We describe their data with our model $v = v_0 + \alpha\Phi$ and compare the interaction parameter α values across the different sample systems. Remarkably, all sample systems are either glasses, close to a glass transition or behave glass-like. Thus, the ballistic stress relaxation type of motion seems necessary to observe the acceleration by beam-induced stress relaxation events. Because of the glassy behavior, we will also use the relation $\Gamma = 1/\tau = vq$ for all samples to convert the given decay rates and decay times into velocities.

Chushkin et al. [60] found fluence-dependent dynamics in protein glasses, as they investigated highly crowded solutions of α-crystalline close to a glass transition at dose rates between $0.3\,\mathrm{kGy\,s^{-1}}$ to $350\,\mathrm{kGy\,s^{-1}}$. We extract the data from Fig. 2(a,c) in the respective work and assume water-like absorption and a beam size of $25 \times 25\mu\mathrm{m}^2$ for translating dose rate into fluence. As the precise length scale of the analysis is not given, we assume further that it has been conducted at the structure factor peak $q = 0.45\,\mathrm{nm^{-1}}$. With that we find $\alpha \approx 0.05\,\mathrm{nm^3\,ph^{-1}}$ for the system close to the glass transition and $\alpha \approx 0.14\,\mathrm{nm^3\,ph^{-1}}$ for the system at the glass transition.

Akhundzadeh [295] investigated radiation effects in the dynamics of a phase-separated solution of Immunoglobulin G (IgG) with polyethylene glycol (PEG) in the same experimental setup as the egg white measurements. The system was cooled to 5 °C where IgG-PEG is known to approach a glass transition [29]. The response of the dynamics to changing fluences can be described by $\alpha = 0.15\,\mathrm{nm^3\,ph^{-1}}$. We group these data with those of Chushkin et al. under the label 'proteins near glass transition' in the comparison of α in Fig. 7.1.

Bin et al. [297] used the fluence-dependent dynamics to investigate the dynamics of hydrated lysozyme at cryogenic temperatures where the sample takes a glass-like state. The applied fluences range from $0.1\,\mathrm{ph\,s^{-1}\,nm^{-2}}$ to $1.4\,\mathrm{ph\,s^{-1}\,nm^{-2}}$. The data from Fig. 1(b) in their work were

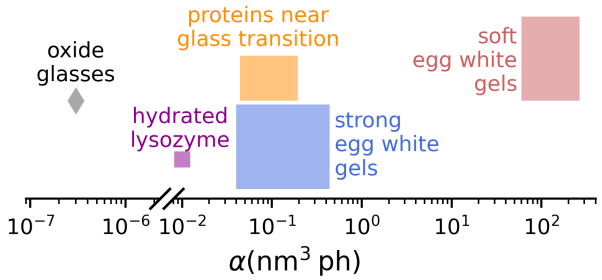

Figure 7.1: Comparison of the parameter α that describes the X-ray-induced acceleration of the dynamics for different sample systems (see equation (6.2)). The plot includes data from Chushkin et al. [60] and Akhundzadeh [295] on protein glasses (yellow), Ruta et al. [56] on oxide glasses (grey) and Bin et al. [297] who investigated hydrated lysozyme (pink).

analyzed at $q = 0.08\,\mathrm{nm}^{-1}$ and can be described by $\alpha = 0.01\,\mathrm{nm}^3\,\mathrm{ph}^{-1}$. The data point is marked by a pink square in Fig. 7.1.

Most of the results on fluence/dose rate effects have been reported on oxide and network glasses so far [56–59, 61]. The dynamics of these samples display no dose effects up to doses of GGy and can be driven by dose rates on the order of MGy. For our comparison, we use the data from the Fig. 2(d) in the work of Ruta et al. [56] where the decay times of three different oxide glasses show the same trend as a function of the flux. After normalization of the flux to the beam size of $8\,\mu\mathrm{m}\times10\,\mu\mathrm{m}$ we obtain an interaction parameter $\alpha \approx 3 \times 10^{-7}\,\mathrm{nm}^3\,\mathrm{ph}^{-1}$.

The values for α from the different systems are summarized in Fig. 7.1, where also the soft and strong egg white gels are included. Together, the values cover nine orders of magnitude, with the oxide glasses being most resistant to the effects of X-ray fluence and the soft egg white gels being extraordinarily sensitive. A possible explanation for these differences is a connection between α and the viscoelastic properties of the samples. Earlier, we found that α is proportional to the spatial extension of the decorrelation events δ. In soft materials that are less packed, we expect an increase in δ and, thereby, in α. Recently, Bonilla and Clausen [184] performed rheology measurements on egg white that was cooked at different temperatures. They found an abrupt increase in the yield stress when the cooking temperature exceeds $72\,^\circ\mathrm{C}$. This increase in yield stress matches our transition from a soft to a strong gel network in terms of radiation susceptibility. However, for a deeper understanding of the mechanisms of radiation susceptibility, the analyses need to cover more different sample systems complemented by simulations and theory.

7.4 Combination of Statics and Dynamics

In this section, we will continue with the discussion on the dose rate dependency of the structure in light of the XPCS results. For the dose rate dependency of the structure, we plotted the relative deviation of the mean intensity I/I_0 as a function of dose $\mathcal{D}$ and dose rate $\dot{\mathcal{D}}$ (Fig. 5.8). In the soft gel networks, we found an increase in intensity with a maximum that shifts towards higher doses with increasing dose rate. If we accept relative deviations in intensity up to 1 %, we get thresholds of a few kGy for the soft gel networks and several ten to one hundred kGy for the strong gel networks. Here, we noticed that the threshold in the strong gel networks displays a dose rate dependency such that higher dose rates lead to higher thresholds. From the analysis of the XPCS results (sec. 6.3), we learned that in this dose rate regime, the dynamics are primarily determined by radiation-induced stress relaxations, so we cannot make use of these higher dose thresholds in structure if we want the dynamics of the sample to be close to equilibrium.

We incorporate the insights from the XPCS analysis into Fig. 5.8 by plotting the relative changes in intensity not as a function of dose $\mathcal{D}$ but of the product of exposure time t and decorrelation rate Γ, as shown in Fig. 7.2. The effect of dose and dose rate is now indirect via the dependency on dose and dose rate of Γ that has been taken from Fig. 6.7. The factor $t \cdot \Gamma(\mathcal{D}, \dot{\mathcal{D}})$ is a measure for the degree of decorrelation during the exposure time t.

With the updated x-axis, the $I/I_0(\Gamma t)$ curves fall almost onto a single master, especially for the soft gel networks. This indicates that the damage thresholds for changes in structure are connected to those for changes in sample dynamics. Again, we set the tolerable deviation to 1 % and find thresholds of $t \cdot \Gamma(\mathcal{D}, \dot{\mathcal{D}}) \approx 1$ for the soft gel networks and $t \cdot \Gamma(\mathcal{D}, \Phi) \approx 0.1$ for the strong gel networks. The sample prepared at 73 °C behaves like a soft gel network in this respect, which was already observed in the analysis of the dose-rate dependent dynamics earlier.

From section 7.1 we know that within the stress relaxation model, one relaxation of the $g^{(2)}$ function is caused by 10–100 micro relaxation events that occur with a rate γ. With this, we can now derive the number of microscopic relaxations that are necessary to change the structure (on the length scale of the gel network) by 1 %: In the soft gels, the changes to the structure lead to a deviation $\geq 1\,\%$ after $t \cdot \gamma =$ 10–100 microscopic relaxations. In the strong gels, 1–10 micro relaxations are sufficient to reach this threshold. This can be understood as the accumulated dose between the events is higher due to the slower dynamics of the strong gel networks.

7.5 Recommendations for Other Experiments

A broad spectrum of experiments can potentially profit from the results on the effects of X-ray radiation in egg whites. Here, we will derive recommendations from our research for designing other XPCS experiments that aim to minimize radiation effects on both the structure and

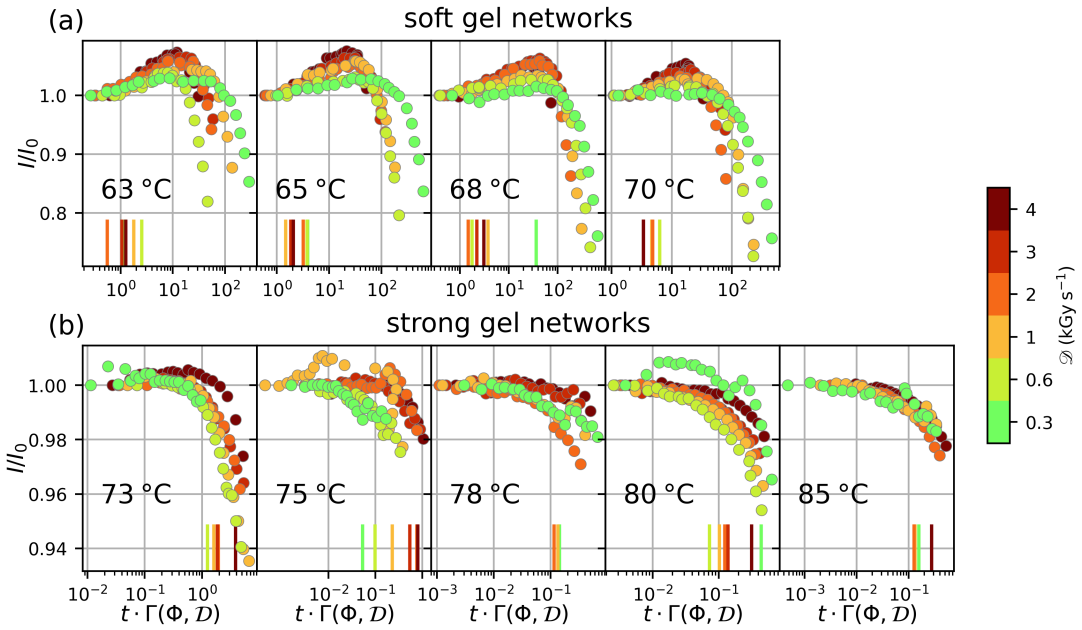

Figure 7.2: Relative changes in the mean scattered intensity as displayed in Fig. 5.8 but as a function of the product of measurement time t and decay rate Γ. The intensity is averaged in $q \in [0.006, 0.03]\mathrm{nm}^{-1}$ and normalized to the intensity at the beginning of the measurement I_0. The corresponding values for Γ have been taken from Fig. 6.7. (a) soft gel network prepared at T_{prep}=70 °C and below. (b) strong gel network prepared at T_{prep}=73 °C and above. The color indicates the X-ray fluence/dose rate. The vertical lines mark the point where the intensity deviation exceeds the 1 %-threshold.

dynamics of their samples.

In our egg white samples that consist of 88 % of water, most of the radiation damage does not arise from direct excitation of the proteins but is mediated by the highly reactive radicals. Effective ways to reduce are, therefore, to reduce radical generation and movement either by replacing water by more radiation-stable solvents or by introducing radical scavenger molecules that interrupt the chain reactions in the generation of free radicals [298–300]. Another way is to reduce the diffusion of the radicals by cooling to cryogenic temperatures which is extensively used in protein crystallography [42–46] but not applicable to most XPCS experiments where the temperatures at which the dynamics are studied is fixed.

Considerations for the experimental setup for dose-limited XPCS measurements at 3rd and 4th generation synchrotrons were already made by Möller et al. [19]. They assumed a lysozyme sample with a maximum tolerable dose of 1 kGy. Using the flux and coherence properties of the (proposed) XPCS beam lines, they vary the photon energy, the beam size, and the sample-to-detector distance such that the signal-to-noise ratio (SNR) is maximized. Their findings are that large beam sizes are favorable as long as they are consistent with the transverse coherence length of the X-ray beam. Otherwise, the scattering contrast and, thereby, the SNR are reduced. The advantage of large beam profiles is that the flux is distributed over a larger volume, which decreases the dose rate and, thereby, the dose that is accumulated at equal times. The disadvantage is that the speckle size S decreases with increasing beam size a according to $S \propto L/a$, which reduces the SNR as soon as the speckle size falls below the size of the detector pixels. This can be compensated by an increase in sample-to-detector distance L to the cost of a decreased scattering contrast due to the limited longitudinal coherence of the X-rays [19].

Performing an X-ray experiment below a sample's dose threshold requires the determination of this threshold. In this study, we demonstrate two different methods to determine dose thresholds: the first one returns the dose where the scattered intensity, which is connected to the structure of the sample, deviates by 1 % from the initial scattering. The choice of 1 % turned out to be a good guess as it returns dose thresholds on the same order of magnitude as the second approach that is based on the sample dynamics. There, we calculated the doses where the first $g^{(2)}$ cuts decay for different dose rates/fluences and found that at high dose rates/fluences, this dose reaches a constant level that matches the dose thresholds derived from the scattering curves.

In addition to the dose effects that can both accelerate and decelerate, the sample dynamics we observed a linear acceleration of the sample dynamics with dose rate/fluence as it was already found in other systems with stress relaxation motion (Sec. 7.3). This acceleration by dose rate can mask the effects of the dose as, for example, in Fig. 6.4(a) where the dependency of the decorrelation rate becomes less dose dependent upon increasing fluences/dose rates. Determining the fluence threshold (that can be converted into a dose rate threshold) requires a series of measurements with different fluences.

We made use of the ballistic behavior of $\Gamma \propto q$ to eliminate length scale dependencies and use the slope v for comparison. The same type of analysis can be conducted using the decorrelation rate Γ instead. From a linear fit of the type $v = v_0 + \alpha\Phi$, one can determine the fluence at which the beam-induced dynamics $\alpha\Phi$ outperform the intrinsic dynamics v_0. As these fluence effects can easily accelerate the dynamics by several orders of magnitude, we also require measurements with low fluences to resolve the value of v_0. We expect this kind of fluence effect with its almost instantaneous nature, mainly in gel and glassy systems where, due to the interconnected structure and dense packing, already single relaxation events have a large impact on the dynamics in contrast to diffusive systems where no additional stress relaxations can be induced.

The dose on the sample can be reduced by reducing the photon flux using absorbers and by replacing continuous illumination with discontinuous patterns. This requires fast X-ray shutters that block the direct beam. At the P10 coherence applications beamline it is currently possible to introduce delay times of 0.1 s and longer to reduce the dose. This option is useful for samples with slow dynamics on time scales ≥ 1 s where we do not need the high resolution of fast exposure times and the scattering contrast allows for shorter exposures. If the shutter is used, the question arises of how to calculate the effective dose rate: Is the behavior of the sample that of a sample that is illuminated continuously with a higher dose rate and just the total dose is reduced or is the behavior different?

We try to predict the results for a sample that displays relaxation dynamics, knowing that additional relaxations are triggered as soon as the sample is irradiated with X-rays (sec. 7.1). In this theoretical scenario, two detector frames are recorded. The time between these two frames is kept constant, but the length of the X-ray irradiation is varied in three different ways, which is illustrated in Fig. 7.3. A black vertical line highlights the start of every frame and we divide the time between them in three bins of equal length, represented as rectangles with a dashed border. We regard three different illumination schemes: (a) the sample is not illuminated with X-rays, (b) the sample is illuminated only 1/3 of the time with X-rays. The X-ray shutter is closed and blocks the beam for the rest of the time. (c) continuous illumination with X-rays as it was done in the data taking for this study. In the next step, we assign (arbitrary) numbers of relaxations triggered in the sample to the scenarios *shutter open* and *shutter close*. We say that in our hypothetical gel or glass sample, ten relaxations occur within one of the time bins if the shutter is closed (dark green rectangles in Fig. 7.3). This is the equilibrium dynamics of the sample. If the shutter is open (light green rectangles in Fig. 7.3) the X-rays trigger additional relaxations. In this case, we choose the numbers such that there are five additional relaxations within one *shutter open* bin. Together with the ten intrinsic relaxations, there are 15 relaxation events in every light green bin.

In the final step, we can compare the number of relaxation events between the starts of the two frames as these are connected to the degree of decorrelation in the XPCS results. For the

equilibrium sample in Fig. 7.3(a), we obtain $3 \times 10 = 30$ relaxations between the two frames. Under continuous illumination (Fig. 7.3(c)), $3 \times (10 + 5) = 45$ relaxation events occur, which reduces to $2 \times 10 + 15 = 35$ events if the shutter is closed for two thirds of the time (Fig. 7.3(b)). From the investigation of the dose rate effects, we know that the number of additional relaxations is directly proportional to the applied X-ray fluence/dose rates. Thus we can conclude that the dynamics obtained in scenario (b) (five additional relaxations) are the same as those from a continuous illumination with one third of the fluence ($3 \cdot 5/3 = 5$ additional relaxations). Consequently, in theory, the effective dose rate needs to be determined from the X-ray fluence averaged over the whole time between two frames. The use of X-ray shutters does not only reduce the dose on the sample but also the effective dose rate. This needs to be tested with systematic measurements on gel samples using different opening times and X-ray fluences. In summary, the theoretical considerations above suggest calculating effective dose rates for the whole period between two frames in an XPCS measurement when comparing radiation effects.

The considerations above rely on our conclusion that X-rays induce additional stress relaxation events and that these effects are restricted to the time when the sample is exposed to the X-rays. This has so far only been observed in gel and glass systems where the dynamics are governed by stress relaxation motion. Therefore, the effective dose rate in diffusive systems is probably different. Deviations from the above also occur if the exposure times approach the time scales of radical diffusion, which can be achieved at modern X-ray free electron lasers [26].

Due to the effective reduction of dose and effective dose rate, there is a great need for X-ray shutters that operate at frequencies faster than 10 Hz and that also allow for non-linear spacing between two frames because, usually, the $g^{(2)}$ function as a result of the XPCS experiment is regarded on a logarithmic time scale. With non-linear exposure schemes, the number of frames and, thereby, the total dose could be reduced while covering the whole time frame of interest. Another approach was proposed by Möller et al. [19] where the $g^{(2)}$ function is stitched together from single data points that originate from exposures with only two frames per spot. Another intelligent exposure scheme is the one used in X-ray speckle visibility where the speckle contrast as a function of exposure time gives access to the sample dynamics [274, 301].

For X-ray studies of the structure of biological samples, a common approach is to use flow cells where the sample is continuously moved through the X-ray beam, which reduces the accumulation of dose in the sample volume [47, 302, 303]. If this is applied in XPCS studies, the measured dynamics are accelerated and the flow rate needs to be adapted to the sample dynamics to resolve these intrinsic dynamics [304–306].

In conclusion, we found in our study that it is not sufficient to evaluate radiation effects in XPCS experiments only on the static scattering patterns or the results on dynamics as effects might be more pronounced in one of them, although the threshold values found from both are comparable. It is always required to measure with varying fluences and compare the evolutions of

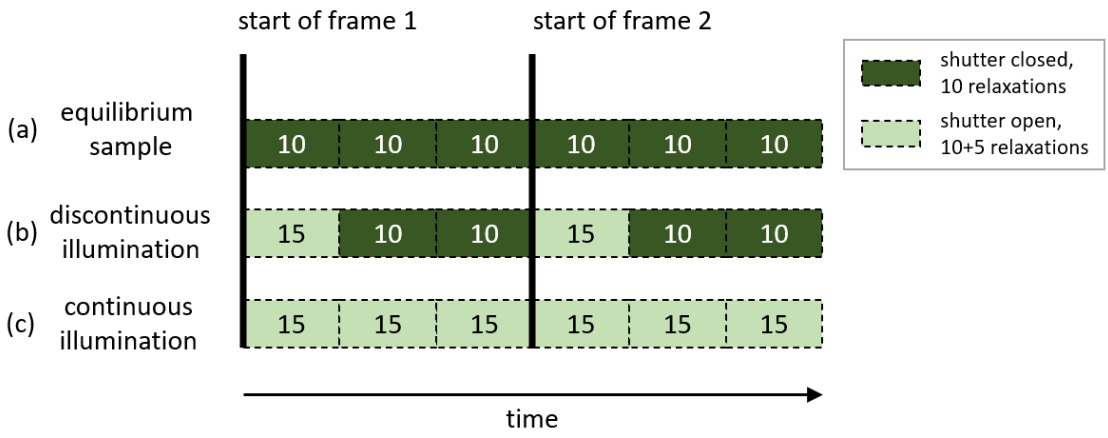

Figure 7.3: Illustration how an X-ray shutter is able to reduce the effective dose rate on the sample. Dark green rectangles are periods where the shutter is closed, and the only relaxations are those from the sample's equilibrium dynamics. For demonstration, we assume ten relaxations within such a period. The X-ray shutter is open during the light green rectangles, and the X-rays induce additional stress relaxation events. We assume that five additional stress relaxation events are induced during every light green rectangle. In this illustration, we record two sample illuminations or frames. (a) Sample in equilibrium without X-ray illuminations. (b) Discontinuous sample illumination. The X-ray Shutter is closed for 2/3 of the time. (c) Continuous illumination where the X-ray shutter is always open.

scattering patterns and two-time correlation functions (TTCs) to assess how close the measured properties are to the equilibrium properties.

Chapter 8

Conclusion and Outlook

The effects of X-ray radiation on the structure and the dynamics of cooked hen egg white are studied employing X-ray photon correlation spectroscopy (XPCS) with fluences ranging from 0.003 to 6 ph s^{-1} nm^{-2}, aiming in particular for a disentanglement of the effects of the X-ray dose and the X-ray dose rate. The experiments are conducted at the P10 Coherence applications beamline at the Deutsches Elektronen-Synchrotron (DESY) where an ultra-small angle X-ray scattering (USAXS) geometry is used to track the behavior on the length scale of the gel network that forms in the egg white samples under heating. The hen egg whites are cooked to temperatures in the range of 50 °C to 85 °C to cover the denaturation temperatures of the hen egg proteins ovalbumin ($T_{\mathrm{prep}} \geq 70\,^{\circ}\mathrm{C}$), ovotransferrin ($T_{\mathrm{prep}} \geq 57\,^{\circ}\mathrm{C}$), and lysozyme ($T_{\mathrm{prep}} \geq 65\,^{\circ}\mathrm{C}$).

An analysis of the gel structure via the static scattering profiles confirms that at temperatures above 60 °C, the egg whites form gel networks that have fractal properties down to the size of the constituting protein microaggregates. An upper limit for the size of these microaggregates can be determined from the static scattering profiles which gives a diameter of 200 nm to 300 nm in agreement with recent microscopy studies [184]. A comparison the X-ray dose where the changes of the static scattering profiles exceed 1 % reveals that we are dealing with two classes of gel networks: a radiation-soft gel network that is formed at temperatures of 60 °C to 70 °C and that is stable up to doses of a few kGy; and a radiation-strong gel network that is formed at higher temperatures with a structure that can resist more than 15 kGy. We attribute the differences to the onset of the denaturation of the ovalbumin protein, which seems to have a stabilizing effect due to its free sulfhydryl groups.

The dose-resolved dynamics of the samples are accessed via horizontal $g^{(2)}$ cuts from two-time correlation functions and fitted with a Kohlrausch-Williams-Watts (KWW)-type exponential decay. The fit parameter Γ, which is the decorrelation rate, shows that the dynamics are on typical time scales for a gel at low doses and dose rates ($1/\Gamma > 100\,\mathrm{s}$). Furthermore, there are typical

markers of ballistic motion in the dynamics, like the decorrelation rate being proportional to the wave vector transfer ($\Gamma \propto q$) and the KWW exponent being close to 3/2. In the soft gel networks, a significant acceleration of the dynamics is observed together with a transition from ballistic to diffusive motion at doses of 2 kGy to 8 kGy, which points towards a dose-induced fluidization of these gels. At even higher doses, these diffusing gel fragments reassemble, probably with a contribution of non-denaturated protein radicals, into a gel-like structure again. The strong gel networks do not display this fluidization and resist doses of 10 kGy and higher.

The dynamics as a function of the dose rate are evaluated via the fluence-dependent velocity of ballistic motion. We find a linear dependency of this velocity on the applied X-ray fluence, as it was observed in other ballistic systems before [56–60, 295]. But in comparison to these systems, the acceleration in the soft egg white gels is three orders of magnitude higher, which we explain in terms of the differences in viscoelasticity. We employ the model of local stress relaxations to describe this acceleration as additional relaxation events triggered by radicals and estimated that we are facing radical production density rates of 1.2×10^{-7}–1.2×10^{-3} radicals s^{-1} nm^{-3} in our study. We found that surprisingly low radical densities are sufficient to induce additional relaxations on the order of magnitude of the intrinsic amount of stress relaxations: in a soft gel network one radical per $(40\,\mathrm{nm})^3$ of sample volume is sufficient, while in a strong egg white gel network this is decreased to one radical per $(20\,\mathrm{nm})^3$. In the end we find that beam-induced changes to structure and dynamics of egg white are closely related as the dose thresholds derived from both are similar. The key is the rate of (beam-induced) microscopic relaxations in the sample that alter the structure and accelerate the dynamics. In a soft gel network 10–100 microscopic relaxations change the USAXS intensity by 1 %, while in the strong gel network only 1–10 relaxations are necessary as the rigidity of the network is higher and the displacement induced by each of the events is larger.

Combining insights from the analyses of structure and dynamics, we could identify a window of opportunity for the egg white gels where measurements of the intrinsic properties on the length scale of the gel network are feasible. For the soft egg white gels, these measurements need to be carried out with doses below 1.5 kGy and dose rates below $0.002\,\mathrm{kGy\,s^{-1}}$ ($\Phi \leq 0.003\mathrm{ph\,s^{-1}\,nm^{-2}}$). In case of the strong gel networks which are prepared above 70 °C, these thresholds are increased to 15 kGy and $0.6\,\mathrm{kGy\,s^{-1}}$ ($\Phi \leq 0.9\mathrm{ph\,s^{-1}\,nm^{-2}}$). The findings in this thesis strongly recommend investigating changes of structure and dynamics of radiation-sensitive samples always both, as a function of dose and dose rate, to identify the window of opportunity for XPCS experiments with minimum radiation effects. Although we found that changes in structure and dynamics are closely related, the effects can compensate for each other in some representations, and it is advisable to investigate both.

Once we know the accelerating effects of X-ray radiation in ballistic systems, they can also be used to access dynamics of systems that would be too slow otherwise. This was already

demonstrated for glassy systems [61, 297].Understanding the effects of X-radiation on radiation sensitive samples also helps with the development of new adapted measurement schemes which will enable the scientific community to utilize the increased coherent flux at the next generation of X-ray sources.

Possible follow-up projects would be to investigate the dynamics of the strong egg white gels at low fluences with longer measurements to see if the linear relation between the velocity of ballistic motion and the fluence holds there as expected. It would also be interesting to perform systematic measurements on radiation effects on a diffusive protein system and compare the results to those presented in this thesis.

Acronyms

BW bandwidth

CRL compound refractive lenses

DAPHNE4NFDI **da**ta from **ph**oton and **ne**utron experiments for NFDI

DESY Deutsches Elektronen-Synchrotron

EIGER **e**xtremely h**ig**h rate det**e**cto**r**

EH experimental hutch

ESRF European synchrotron radiation facility

ExPaNDS European open science cloud photon and neutron data service

FAIR findable, accessible, interoperable, and reusable

HDF5 hierarchical data format 5

HHM high heat load monochromator

IgG Immunoglobulin G

KWW Kohlrausch-Williams-Watts

LET linear energy transfer

NeXus Neutron X-ray μ (muon) science

NFDI Nationale Forschungsdateninfrastruktur

OH optical hutch

PaNOSC photon and neutron open science cloud

PDF probability distribution function

PEG polyethylene glycol

PETRA Positron-Elektron-Tandem-Ring-Anlage

pyFAI python fast azimuthal integration

ROI region of interest

SALR short-range attraction, long-range repulsion

SAXS small-angle X-ray scattering

SNR signal-to-noise ratio

TTC two-time correlation function

USAXS ultra-small angle X-ray scattering

Xana X-ray analysis software for XPCS data

XPCS X-ray photon correlation spectroscopy

XSVS X-ray speckle visibility spectroscopy

Measurement Details

Table 8.1: Typical combinations of absorbers n, exposure times t_{exp} and number of frames N_{fr} used in a standard measurement (Sec. 3.5.1).

n	t_{exp} (s)	N_{fr}
24	0.5	2000
18	0.2	1000
16	0.2	1000
12	0.1	2000
8	0.005	4000
8	0.04	5000
6	0.005	4000
6	0.04	5000
4	0.005	4000
4	0.04	5000
2	0.005	4000
2	0.04	5000
1	0.005	4000
1	0.04	5000
0	0.005	4000
0	0.04	5000

Table 8.2: Typical combinations of absorbers n, exposure times t_{exp} and number of frames N_{fr} used in a measurement investigating dose rate effects (Sec. 3.5.3).

n	t_{exp} (s)	N_{fr}
24	0.5	2000
16	0.2	2000
24	0.5	2000
8	0.05	4000
24	0.5	2000
4	0.2	1000
24	0.5	2000
0	0.2	1000
24	0.5	2000

Bibliography

[1] W. Widłak. "Protein Structure and Function". In: *Molecular Biology*. Ed. by D. Hutchison et al. Vol. 8248. Berlin, Heidelberg: Springer Berlin Heidelberg, 2013, pp. 15–29.

[2] J. Jumper et al. "Highly Accurate Protein Structure Prediction with AlphaFold". In: *Nature* 596.7873 (Aug. 2021), pp. 583–589.

[3] G. Zaccai. "How Soft Is a Protein? A Protein Dynamics Force Constant Measured by Neutron Scattering". In: *Science* 288.5471 (June 2000), pp. 1604–1607.

[4] K. A. Henzler-Wildman et al. "A Hierarchy of Timescales in Protein Dynamics Is Linked to Enzyme Catalysis". In: *Nature* 450.7171 (Dec. 2007), pp. 913–916.

[5] H. Frauenfelder et al. "A Unified Model of Protein Dynamics". In: *Proceedings of the National Academy of Sciences* 106.13 (Mar. 2009), pp. 5129–5134.

[6] D. Richter. "Future Perspectives: Moving to Longer Length and Time Scales, from Polymers to Biological Macromolecules". In: *Dynamics of Soft Matter*. Ed. by V. García Sakai, C. Alba-Simionesco, and S.-H. Chen. New York, NY: Springer US, 2012, pp. 145–186.

[7] L.-Q. Yang et al. "Protein Dynamics and Motions in Relation to Their Functions: Several Case Studies and the Underlying Mechanisms". In: *Journal of Biomolecular Structure and Dynamics* 32.3 (Mar. 2014), pp. 372–393.

[8] L. Hong et al. "Determination of Functional Collective Motions in a Protein at Atomic Resolution Using Coherent Neutron Scattering". In: *Science Advances* 2.10 (Oct. 2016), e1600886.

[9] E. Campbell et al. "The Role of Protein Dynamics in the Evolution of New Enzyme Function". In: *Nature Chemical Biology* 12.11 (Nov. 2016), pp. 944–950.

[10] G. Grübel and F. Zontone. "Correlation Spectroscopy with Coherent X-rays". In: *Journal of Alloys and Compounds* 362.1-2 (Jan. 2004), pp. 3–11.

[11] S. Amin, C. A. Rega, and H. Jankevics. "Detection of Viscoelasticity in Aggregating Dilute Protein Solutions through Dynamic Light Scattering-Based Optical Microrheology". In: *Rheologica Acta* 51.4 (Apr. 2012), pp. 329–342.

[12] M. J. Bergman et al. "Experimental Evidence for a Cluster Glass Transition in Concentrated Lysozyme Solutions". In: *The Journal of Physical Chemistry B* 123.10 (Mar. 2019), pp. 2432–2438.

[13] M. Levin, G. Bel, and Y. Roichman. "Measurements and Characterization of the Dynamics of Tracer Particles in an Actin Network". In: *The Journal of Chemical Physics* 154.14 (Apr. 2021), p. 144901.

[14] M. Grimaldo et al. "Protein Short-Time Diffusion in a Naturally Crowded Environment". In: *The Journal of Physical Chemistry Letters* 10.8 (Apr. 2019), pp. 1709–1715.

[15] F. Roosen-Runge et al. "Protein Self-Diffusion in Crowded Solutions". In: *Proceedings of the National Academy of Sciences* 108.29 (July 2011), pp. 11815–11820.

[16] M. Sutton et al. "Using Coherence to Measure Two-Time Correlation Functions". In: *Optics Express* 11.19 (Sept. 2003), p. 2268.

[17] F. Zhang et al. "Development of Ultra-Small-Angle X-ray Scattering–X-ray Photon Correlation Spectroscopy". In: *Journal of Applied Crystallography* 44.1 (Feb. 2011), pp. 200–212.

[18] A. Madsen, A. Fluerasu, and B. Ruta. "Structural Dynamics of Materials Probed by X-Ray Photon Correlation Spectroscopy". In: *Synchrotron Light Sources and Free-Electron Lasers*. Ed. by E. J. Jaeschke et al. Cham: Springer International Publishing, 2016, pp. 1617–1641.

[19] J. Möller et al. "X-Ray Photon Correlation Spectroscopy of Protein Dynamics at Nearly Diffraction-Limited Storage Rings". In: *IUCrJ* 6.5 (Sept. 2019), pp. 794–803.

[20] F. Perakis and C. Gutt. "Towards Molecular Movies with X-ray Photon Correlation Spectroscopy". In: *Physical Chemistry Chemical Physics* 22.35 (2020), pp. 19443–19453.

[21] W. Jo et al. "Nanosecond X-ray Photon Correlation Spectroscopy Using Pulse Time Structure of a Storage-Ring Source". In: *IUCrJ* 8.1 (Jan. 2021), pp. 124–130.

[22] F. Lehmkühler, W. Roseker, and G. Grübel. "From Femtoseconds to Hours—Measuring Dynamics over 18 Orders of Magnitude with Coherent X-rays". In: *Applied Sciences* 11.13 (July 2021), p. 6179.

[23] S. Berkowicz et al. "Nanofocused X-Ray Photon Correlation Spectroscopy". In: *Physical Review Research* 4.3 (July 2022), p. L032012.

[24] A. Pal et al. "Anisotropic Collective Dynamics: Anomalous Dynamics of Magnetic Anisotropic Colloids Studied by XPCS (Small 46/2018)". In: *Small* 14.46 (Nov. 2018), p. 1870219.

[25] J. Li et al. "Observation of Collective Molecular Dynamics in a Chalcogenide Glass: Results from X-ray Photon Correlation Spectroscopy". In: *The Journal of Physical Chemistry B* 126.28 (July 2022), pp. 5320–5325.

[26] M. Reiser et al. "Resolving Molecular Diffusion and Aggregation of Antibody Proteins with Megahertz X-ray Free-Electron Laser Pulses". In: *Nature Communications* 13.1 (Sept. 2022), p. 5528.

[27] N. D. Anthuparambil et al. "Exploring Non-Equilibrium Processes and Spatio-Temporal Scaling Laws in Heated Egg Yolk Using Coherent X-rays". In: *Nature Communications* 14.1 (Sept. 2023), p. 5580.

[28] H. Rahmann. "Realization of Low Dose XPCS Experiments for the Investigation of Protein Dynamics". PhD thesis. Universität Siegen, 2020.

[29] A. Girelli et al. "Microscopic Dynamics of Liquid-Liquid Phase Separation and Domain Coarsening in a Protein Solution Revealed by X-Ray Photon Correlation Spectroscopy". In: *Physical Review Letters* 126.13 (Apr. 2021), p. 138004.

[30] W. P. Burmeister. "Structural Changes in a Cryo-Cooled Protein Crystal Owing to Radiation Damage". In: *Acta Crystallographica Section D Biological Crystallography* 56.3 (Mar. 2000), pp. 328–341.

[31] K. L. Shelley and E. F. Garman. "Quantifying and Comparing Radiation Damage in the Protein Data Bank". In: *Nature Communications* 13.1 (Mar. 2022), p. 1314.

[32] R. B. Ravelli and S. M. McSweeney. "The 'Fingerprint' That X-rays Can Leave on Structures". In: *Structure* 8.3 (Mar. 2000), pp. 315–328.

[33] M. Weik et al. "Specific Chemical and Structural Damage to Proteins Produced by Synchrotron Radiation". In: *Proceedings of the National Academy of Sciences* 97.2 (Jan. 2000), pp. 623–628.

[34] E. F. Garman and R. L. Owen. "Cryocooling and Radiation Damage in Macromolecular Crystallography". In: *Acta Crystallographica Section D Biological Crystallography* 62.1 (Jan. 2006), pp. 32–47.

[35] R. L. Owen, E. Rudiño-Piñera, and E. F. Garman. "Experimental Determination of the Radiation Dose Limit for Cryocooled Protein Crystals". In: *Proceedings of the National Academy of Sciences* 103.13 (Mar. 2006), pp. 4912–4917.

[36] H. Taberman. "Radiation Damage in Macromolecular Crystallography—An Experimentalist's View". In: *Crystals* 8.4 (Apr. 2018), p. 157.

[37] K. Nass. "Radiation Damage in Protein Crystallography at X-ray Free-Electron Lasers". In: *Acta Crystallographica Section D Structural Biology* 75.2 (Feb. 2019), pp. 211–218.

[38] E. F. Garman. "Radiation Damage in Macromolecular Crystallography: What Is It and Why Should We Care?" In: *Acta Crystallographica Section D Biological Crystallography* 66.4 (Apr. 2010), pp. 339–351.

[39] E. de la Mora et al. "Radiation Damage and Dose Limits in Serial Synchrotron Crystallography at Cryo- and Room Temperatures". In: *Proceedings of the National Academy of Sciences* 117.8 (Feb. 2020), pp. 4142–4151.

[40] B. Alberts et al. "Analyzing Protein Structure and Function". In: *Biology of the Cell*. 4th ed. New York: Garland Science, 2002.

[41] J. Drenth. *Principles of Protein X-Ray Crystallography*. New York, NY: Springer New York, 2007.

[42] D. J. Haas. "X-Ray Studies on Lysozyme Crystals at –50°C". In: *Acta Crystallographica Section B Structural Crystallography and Crystal Chemistry* 24.4 (Apr. 1968), pp. 604–604.

[43] H. Hope. "Cryocrystallography of Biological Macromolecules: A Generally Applicable Method". In: *Acta Crystallographica Section B Structural Science* 44.1 (Feb. 1988), pp. 22–26.

[44] E. F. Garman. "Developments in X-ray Crystallographic Structure Determination of Biological Macromolecules". In: *Science* 343.6175 (Mar. 2014), pp. 1102–1108.

[45] J. W. Pflugrath. "Practical Macromolecular Cryocrystallography". In: *Acta Crystallographica Section F Structural Biology Communications* 71.6 (June 2015), pp. 622–642.

[46] D. J. Haas. "The Early History of Cryo-Cooling for Macromolecular Crystallography". In: *IUCrJ* 7.2 (Mar. 2020), pp. 148–157.

[47] C. M. Jeffries et al. "Limiting Radiation Damage for High-Brilliance Biological Solution Scattering: Practical Experience at the EMBL P12 Beamline PETRAIII". In: *Journal of Synchrotron Radiation* 22.2 (Mar. 2015), pp. 273–279.

[48] W. H. Hamill. "Model for the Radiolysis of Water". In: *The Journal of Physical Chemistry* 73.5 (May 1969), pp. 1341–1347.

[49] H. A. Schwarz. "Free Radicals Generated by Radiolysis of Aqueous Solutions". In: *Journal of Chemical Education* 58.2 (Feb. 1981), p. 101.

[50] V. Svoboda et al. "Real-Time Observation of Water Radiolysis and Hydrated Electron Formation Induced by Extreme-Ultraviolet Pulses". In: *Science Advances* 6.3 (Jan. 2020), eaaz0385.

[51] Z.-H. Loh et al. "Observation of the Fastest Chemical Processes in the Radiolysis of Water". In: *Science* 367.6474 (Jan. 2020), pp. 179–182.

[52] A. Jain et al. “Three-Step Colloidal Gelation Revealed by Time-Resolved x-Ray Photon Correlation Spectroscopy”. In: *The Journal of Chemical Physics* 157.18 (Nov. 2022), p. 184901.

[53] A. Ragulskaya et al. “Interplay between Kinetics and Dynamics of Liquid–Liquid Phase Separation in a Protein Solution Revealed by Coherent X-ray Spectroscopy”. In: *The Journal of Physical Chemistry Letters* 12.30 (Aug. 2021), pp. 7085–7090.

[54] N. Begam et al. “Kinetics of Network Formation and Heterogeneous Dynamics of an Egg White Gel Revealed by Coherent X-Ray Scattering”. In: *Physical Review Letters* 126.9 (Mar. 2021), p. 098001.

[55] N. Begam et al. “Effects of Temperature and Ionic Strength on the Microscopic Structure and Dynamics of Egg White Gels”. In: *The Journal of Chemical Physics* 158.7 (Feb. 2023), p. 074903.

[56] B. Ruta et al. “Hard X-rays as Pump and Probe of Atomic Motion in Oxide Glasses”. In: *Scientific Reports* 7.1 (Dec. 2017), p. 3962.

[57] G. Pintori et al. “Relaxation Dynamics Induced in Glasses by Absorption of Hard X-Ray Photons”. In: *Physical Review B* 99.22 (June 2019), p. 224206.

[58] G. Pintori et al. “X-Ray Induced Dynamics in Borate Glasses with Different Network Connectivity”. In: *Physical Review B* 105.10 (Mar. 2022), p. 104207.

[59] K. Holzweber et al. “Beam-Induced Atomic Motion in Alkali Borate Glasses”. In: *Physical Review B* 100.21 (Dec. 2019), p. 214305.

[60] Y. Chushkin et al. “Probing Cage Relaxation in Concentrated Protein Solutions by X-Ray Photon Correlation Spectroscopy”. In: *Physical Review Letters* 129.23 (Nov. 2022), p. 238001.

[61] F. Dallari et al. “Stochastic Atomic Acceleration during the X-ray-induced Fluidization of a Silica Glass”. In: *Proceedings of the National Academy of Sciences* 120.2 (Jan. 2023), e2213182120.

[62] Y. Mine. “Recent Advances in the Understanding of Egg White Protein Functionality”. In: *Trends in Food Science & Technology* 6.7 (July 1995), pp. 225–232.

[63] M. Rumbo et al. “Analysis of Structural Properties and Immunochemical Reactivity of Heat-Treated Ovalbumin”. In: *Journal of Agricultural and Food Chemistry* 44.12 (Jan. 1996), pp. 3793–3798.

[64] I. Van der Plancken, A. Van Loey, and M. E. Hendrickx. “Effect of Heat-Treatment on the Physico-Chemical Properties of Egg White Proteins: A Kinetic Study”. In: *Journal of Food Engineering* 75.3 (Aug. 2006), pp. 316–326.

[65] A. Duri and L. Cipelletti. “Length Scale Dependence of Dynamical Heterogeneity in a Colloidal Fractal Gel”. In: *Europhysics Letters (EPL)* 76.5 (Dec. 2006), pp. 972–978.

[66] E. Weckert. “The Potential of Future Light Sources to Explore the Structure and Function of Matter”. In: *IUCrJ* 2.2 (Mar. 2015), pp. 230–245.

[67] C. G. Schroer et al. “PETRA IV: The Ultralow-Emittance Source Project at DESY”. In: *Journal of Synchrotron Radiation* 25.5 (Sept. 2018), pp. 1277–1290.

[68] J. K. G. Dhont. *An Introduction to Dynamics of Colloids*. Amsterdam, Netherlands: Elsevier, 1996.

[69] H. Tanaka, Y. Nishikawa, and T. Koyama. “Network-Forming Phase Separation of Colloidal Suspensions”. In: *Journal of Physics: Condensed Matter* 17.15 (Apr. 2005), pp. L143–L153.

[70] P. Debye and E. Hückel. “Zur Theorie Der Elektrolyte. I. Gefrierpunktserniedrigung Und Verwandte Erscheinungen”. In: *Physikal. Zeitschr.* 24 (1923), p. 185.

[71] S. Levine. “Problems of Stability in Hydrophobic Colloidal Solutions II. On the Interaction of Two Colloidal Metallic Particles: m Athem Atical Theory”. In: *Proceedings of the Royal Society of London. Series A. Mathematical and Physical Sciences* 170.941 (Mar. 1939), pp. 165–182.

[72] S. Levine and G. P. Dube. “Interaction between Two Hydrophobic Colloidal Particles, Using the Approximate Debye-Hückel Theory. I. General Properties”. In: *Trans. Faraday Soc.* 35.0 (1939), pp. 1125–1140.

[73] E. J. W. Verwey. “Theory of the Stability of Lyophobic Colloids.” In: *The Journal of Physical and Colloid Chemistry* 51.3 (Mar. 1947), pp. 631–636.

[74] B. Derjaguin and L. Landau. “Theory of the Stability of Strongly Charged Lyophobic Sols and of the Adhesion of Strongly Charged Particles in Solutions of Electrolytes”. In: *Progress in Surface Science* 43.1-4 (May 1993), pp. 30–59.

[75] S. Asakura and F. Oosawa. “On Interaction between Two Bodies Immersed in a Solution of Macromolecules”. In: *The Journal of Chemical Physics* 22.7 (July 1954), pp. 1255–1256.

[76] J. Bergenholtz, W. C. K. Poon, and M. Fuchs. “Gelation in Model Colloid-Polymer Mixtures”. In: *Langmuir* 19.10 (May 2003), pp. 4493–4503.

[77] P. J. Lu et al. “Gelation of Particles with Short-Range Attraction”. In: *Nature* 453.7194 (May 2008), pp. 499–503.

[78] J. Hendricks et al. “Different Mechanisms for Dynamical Arrest in Largely Asymmetric Binary Mixtures”. In: *Physical Review E* 91.3 (Mar. 2015), p. 032308.

[79] Y. Kantor and I. Webman. "Elastic Properties of Random Percolating Systems". In: *Physical Review Letters* 52.21 (May 1984), pp. 1891–1894.

[80] A. H. Krall and D. A. Weitz. "Internal Dynamics and Elasticity of Fractal Colloidal Gels". In: *Physical Review Letters* 80.4 (Jan. 1998), pp. 778–781.

[81] H. J. Walls et al. "Yield Stress and Wall Slip Phenomena in Colloidal Silica Gels". In: *Journal of Rheology* 47.4 (July 2003), pp. 847–868.

[82] J. S. Weston, J. H. Harwell, and B. P. Grady. "Rheological Characterization of Yield Stress Gels Formed via Electrostatic Heteroaggregation of Metal Oxide Nanoparticles". In: *Soft Matter* 13.38 (2017), pp. 6743–6755.

[83] P. Pusey, A. Pirie, and W. Poon. "Dynamics of Colloid-Polymer Mixtures". In: *Physica A: Statistical Mechanics and its Applications* 201.1-3 (Dec. 1993), pp. 322–331.

[84] W. Poon and M. Haw. "Mesoscopic Structure Formation in Colloidal Aggregation and Gelation". In: *Advances in Colloid and Interface Science* 73 (Oct. 1997), pp. 71–126.

[85] P. Charbonneau and D. R. Reichman. "Systematic Characterization of Thermodynamic and Dynamical Phase Behavior in Systems with Short-Ranged Attraction". In: *Physical Review E* 75.1 (Jan. 2007), p. 011507.

[86] P. N. Pusey and W. van Megen. "Phase Behaviour of Concentrated Suspensions of Nearly Hard Colloidal Spheres". In: *Nature* 320.6060 (Mar. 1986), pp. 340–342.

[87] P. N. Pusey and W. van Megen. "Observation of a Glass Transition in Suspensions of Spherical Colloidal Particles". In: *Physical Review Letters* 59.18 (Nov. 1987), pp. 2083–2086.

[88] W. van Megen and S. M. Underwood. "Glass Transition in Colloidal Hard Spheres: Measurement and Mode-Coupling-Theory Analysis of the Coherent Intermediate Scattering Function". In: *Physical Review E* 49.5 (May 1994), pp. 4206–4220.

[89] E. Zaccarelli and W. C. K. Poon. "Colloidal Glasses and Gels: The Interplay of Bonding and Caging". In: *Proceedings of the National Academy of Sciences* 106.36 (Sept. 2009), pp. 15203–15208.

[90] L. M. C. Janssen. "Mode-Coupling Theory of the Glass Transition: A Primer". In: *Frontiers in Physics* 6 (Oct. 2018), p. 97.

[91] J. M. Brader, M. E. Cates, and M. Fuchs. "First-Principles Constitutive Equation for Suspension Rheology". In: *Physical Review Letters* 101.13 (Sept. 2008), p. 138301.

[92] P. J. Flory. "Molecular Size Distribution in Three Dimensional Polymers. I. Gelation [1]". In: *Journal of the American Chemical Society* 63.11 (Nov. 1941), pp. 3083–3090.

[93] W. H. Stockmayer. "Theory of Molecular Size Distribution and Gel Formation in Branched-Chain Polymers". In: *The Journal of Chemical Physics* 11.2 (Feb. 1943), pp. 45–55.

[94] W. H. Stockmayer. "Theory of Molecular Size Distribution and Gel Formation in Branched Polymers II. General Cross Linking". In: *The Journal of Chemical Physics* 12.4 (Apr. 1944), pp. 125–131.

[95] D. Stauffer. *Introduction to Percolation Theory*. London ; Philadelphia: Taylor & Francis, 1985.

[96] D. Stauffer, A. Coniglio, and M. Adam. "Gelation and Critical Phenomena". In: *Polymer Networks*. Ed. by K. Dušek. Vol. 44. Berlin, Heidelberg: Springer Berlin Heidelberg, 1982, pp. 103–158.

[97] M. E. Fisher and J. W. Essam. "Some Cluster Size and Percolation Problems". In: *Journal of Mathematical Physics* 2.4 (July 1961), pp. 609–619.

[98] J. W. Essam. "Percolation Theory". In: *Reports on Progress in Physics* 43.7 (July 1980), pp. 833–912.

[99] K. Christensen. "Percolation Theory". In: *Imperial College London* 1 (2002).

[100] M. Fixman. "Radius of Gyration of Polymer Chains". In: *The Journal of Chemical Physics* 36.2 (Jan. 1962), pp. 306–310.

[101] B. B. Mandelbrot. *The Fractal Geometry of Nature*. San Francisco: W.H. Freeman, 1982.

[102] N. Jan and D. Stauffer. "Random Site Percolation in Three Dimensions". In: *International Journal of Modern Physics C* 09.02 (Mar. 1998), pp. 341–347.

[103] H. G. Ballesteros et al. "Scaling Corrections: Site Percolation and Ising Model in Three Dimensions". In: *Journal of Physics A: Mathematical and General* 32.1 (Jan. 1999), pp. 1–13.

[104] Y. Deng and H. W. J. Blöte. "Monte Carlo Study of the Site-Percolation Model in Two and Three Dimensions". In: *Physical Review E* 72.1 (July 2005), p. 016126.

[105] C. D. Lorenz and R. M. Ziff. "Precise Determination of the Bond Percolation Thresholds and Finite-Size Scaling Corrections for the Sc, Fcc, and Bcc Lattices". In: *Physical Review E* 57.1 (Jan. 1998), pp. 230–236.

[106] D. Tiggemann. "SIMULATION OF PERCOLATION ON MASSIVELY-PARALLEL COMPUTERS". In: *International Journal of Modern Physics C* 12.06 (July 2001), pp. 871–878.

[107] S. W. Haan and R. Zwanzig. "Series Expansions in a Continuum Percolation Problem". In: *Journal of Physics A: Mathematical and General* 10.9 (Sept. 1977), pp. 1547–1555.

[108] T. Vicsek and J. Kertesz. “Monte Carlo Renormalisation-Group Approach to Percolation on a Continuum: Test of Universality”. In: *Journal of Physics A: Mathematical and General* 14.2 (Feb. 1981), pp. L31–L37.

[109] W. Burchard et al. “Rayleigh Scattering from Solutions of Critically Branched Polycondensates”. In: *Macromolecules* 6.4 (July 1973), pp. 642–649.

[110] M. Gordon et al. “Dilute Solution Properties of Critically Branched Systems”. In: *Die Makromolekulare Chemie* 176.8 (Aug. 1975), pp. 2413–2435.

[111] R. S. Whitney and W. Burchard. “Molecular Size and Gel Formation in Branched Poly(Methyl Methacrylate) Copolymers”. In: *Die Makromolekulare Chemie* 181.4 (Apr. 1980), pp. 869–890.

[112] M. Adam et al. “Mechanical Properties near Gelation Threshold, Comparison with Classical and 3d Percolation Theories”. In: *Pure and Applied Chemistry* 53.8 (Jan. 1981), pp. 1489–1494.

[113] B. Gauthier-Manuel and E. Guyon. “Critical, Elasticity of Polyacrylamide above Its Gel Point”. In: *Journal de Physique Lettres* 41.21 (1980), pp. 503–505.

[114] P. de Gennes. *Scaling Concepts in Polymer Physics*. Cornell University Press, 1979.

[115] E. Zaccarelli. “Colloidal Gels: Equilibrium and Non-Equilibrium Routes”. In: *Journal of Physics: Condensed Matter* 19.32 (Aug. 2007), p. 323101.

[116] R. Mezzenga et al. “Understanding Foods as Soft Materials”. In: *Nature Materials* 4.10 (Oct. 2005), pp. 729–740.

[117] T. A. Vilgis. “Soft Matter Food Physics—the Physics of Food and Cooking”. In: *Reports on Progress in Physics* 78.12 (Dec. 2015), p. 124602.

[118] S. Banerjee and S. Bhattacharya. “Food Gels: Gelling Process and New Applications”. In: *Critical Reviews in Food Science and Nutrition* 52.4 (Apr. 2012), pp. 334–346.

[119] J. M. Berg et al. “Zusammensetzung und Struktur der Proteine”. In: *Stryer Biochemie*. Berlin, Heidelberg: Springer Berlin Heidelberg, 2018, pp. 31–77.

[120] L. Pauling, R. B. Corey, and H. R. Branson. “The Structure of Proteins: Two Hydrogen-Bonded Helical Configurations of the Polypeptide Chain”. In: *Proceedings of the National Academy of Sciences* 37.4 (Apr. 1951), pp. 205–211.

[121] X. Zhao, Y. Fu, and C. Song. “Proteins”. In: *Essentials of Food Chemistry*. Ed. by J. Kan and K. Chen. Singapore: Springer Singapore, 2021, pp. 49–121.

[122] E. Sarantidi et al. “Egg White and Yolk Protein Atlas: New Protein Insights of a Global Landmark Food”. In: *Foods* 12.18 (Sept. 2023), p. 3470.

[123] K. F. Kiple. *A Movable Feast: Ten Millennia of Food Globalization*. 1st ed. Cambridge University Press, Apr. 2007.

[124] K. Lomakina and Mikova, Kamila. "A Study of the Factors Affecting the Foaming Properties of Egg White–a Review". In: *Czech Journal of Food Sciences* 24.3 (2006), pp. 110–118.

[125] L. Campbell, V. Raikos, and S. R. Euston. "Modification of Functional Properties of Egg-White Proteins". In: *Nahrung/Food* 47.6 (Dec. 2003), pp. 369–376.

[126] A. Gennadios et al. "Mechanical and Barrier Properties of Egg Albumen Films". In: *Journal of Food Science* 61.3 (May 1996), pp. 585–589.

[127] R. Lee et al. "Influence of Glycerol and Water Activity on the Properties of Compressed Egg White-Based Bioplastics". In: *Journal of Food Engineering* 118.1 (Sept. 2013), pp. 132–140.

[128] M. P. Pranata et al. "Egg White Protein Film Production Through Extrusion and Calendering Processes and Its Suitability for Food Packaging Applications". In: *Food and Bioprocess Technology* 12.4 (Apr. 2019), pp. 714–727.

[129] X. Dong and Y.-Q. Zhang. "An Insight on Egg White: From Most Common Functional Food to Biomaterial Application". In: *Journal of Biomedical Materials Research Part B: Applied Biomaterials* 109.7 (July 2021), pp. 1045–1058.

[130] C. Guérin-Dubiard et al. "Proteomic Analysis of Hen Egg White". In: *Journal of Agricultural and Food Chemistry* 54.11 (May 2006), pp. 3901–3910.

[131] B. Bílková et al. "Domestic Fowl Breed Variation in Egg White Protein Expression: Application of Proteomics and Transcriptomics". In: *Journal of Agricultural and Food Chemistry* 66.44 (Nov. 2018), pp. 11854–11863.

[132] S. Arena, G. Renzone, and A. Scaloni. "A Multi-Approach Peptidomic Analysis of Hen Egg White Reveals Novel Putative Bioactive Molecules". In: *Journal of Proteomics* 215 (Mar. 2020), p. 103646.

[133] C. D'Ambrosio et al. "Exploring the Chicken Egg White Proteome with Combinatorial Peptide Ligand Libraries". In: *Journal of Proteome Research* 7.8 (Aug. 2008), pp. 3461–3474.

[134] K. Mann. "The Chicken Egg White Proteome". In: *PROTEOMICS* 7.19 (Oct. 2007), pp. 3558–3568.

[135] X. Wang et al. "Differential Proteomic Analysis Revealed Crucial Egg White Proteins for Hatchability of Chickens". In: *Poultry Science* 98.12 (Dec. 2019), pp. 7076–7089.

[136] H. Wang et al. "Quantitative Comparative Integrated Proteomic and Phosphoproteomic Analysis of Chicken Egg Yolk Proteins under Diverse Storage Temperatures". In: *Journal of Agricultural and Food Chemistry* 68.4 (Jan. 2020), pp. 1157–1167.

[137] A. D'Alessandro et al. "The Egg White and Yolk Interactomes as Gleaned from Extensive Proteomic Data". In: *Journal of Proteomics* 73.5 (Mar. 2010), pp. 1028–1042.

[138] K. Mann and M. Mann. "In-Depth Analysis of the Chicken Egg White Proteome Using an LTQ Orbitrap Velos". In: *Proteome Science* 9.1 (2011), p. 7.

[139] J. Wang et al. "Proteomics Analysis of Egg White Proteins from Different Egg Varieties". In: *Journal of Agricultural and Food Chemistry* 60.1 (Jan. 2012), pp. 272–282.

[140] C. Sun et al. "Divergent Proteome Patterns of Egg Albumen from Domestic Chicken, Duck, Goose, Turkey, Quail and Pigeon". In: *PROTEOMICS* 17.17-18 (Sept. 2017), p. 1700145.

[141] L. McReynolds et al. "Sequence of Chicken Ovalbumin mRNA". In: *Nature* 273.5665 (June 1978), pp. 723–728.

[142] A. D. Nisbet et al. "The Complete Amino-Acid Sequence of Hen Ovalbumin". In: *European Journal of Biochemistry* 115.2 (Apr. 1981), pp. 335–345.

[143] S. L. C. Woo et al. "Complete Nucleotide Sequence of the Chicken Chromosomal Ovalbumin Gene and Its Biological Significance". In: *Biochemistry* 20.22 (Oct. 1981), pp. 6437–6446.

[144] J. A. Huntington and P. E. Stein. "Structure and Properties of Ovalbumin". In: *Journal of Chromatography B: Biomedical Sciences and Applications* 756.1-2 (May 2001), pp. 189–198.

[145] M. Halwer, G. C. Nutting, and B. A. Brice. "Molecular Weight of Lactoglobulin, Ovalbumin, Lysozyme and Serum Albumin by Light Scattering ²". In: *Journal of the American Chemical Society* 73.6 (June 1951), pp. 2786–2790.

[146] R. Nakamura and M. Ishimaru. "Changes in the Shape and Surface Hydrophobicity of Ovalbumin during Its Transformation to *S* -Ovalbumin". In: *Agricultural and Biological Chemistry* 45.12 (Dec. 1981), pp. 2775–2780.

[147] T. Matsumoto and J. Chiba. "Rheological and Small-Angle X-ray Scattering Investigations on the Shape and Ordered Arrangement of Native Ovalbumin Molecules in Aqueous Colloids". In: *Journal of the Chemical Society, Faraday Transactions* 86.16 (1990), p. 2877.

[148] A. Kato et al. "Protein Flexibility and Functional Properties of Heat-Denatured Ovalbumin and Lysozyme." In: *Agricultural and Biological Chemistry* 50.2 (1986), pp. 417–420.

[149] M. Ferreira, C. Hofer, and A. Raemy. "A Calorimetric Study of Egg White Proteins". In: *Journal of Thermal Analysis* 48.3 (Mar. 1997), pp. 683–690.

[150] T. Strixner and U. Kulozik. "Egg Proteins". In: *Handbook of Food Proteins*. Elsevier, 2011, pp. 150–209.

[151] K. Shimada and J. C. Cheftel. "Sulfhydryl Group/Disulfide Bond Interchange Reactions during Heat-Induced Gelation of Whey Protein Isolate". In: *Journal of Agricultural and Food Chemistry* 37.1 (Jan. 1989), pp. 161–168.

[152] K. Iwashita, A. Handa, and K. Shiraki. "Co-Aggregation of Ovalbumin and Lysozyme". In: *Food Hydrocolloids* 67 (June 2017), pp. 206–215.

[153] K. Broersen et al. "Do Sulfhydryl Groups Affect Aggregation and Gelation Properties of Ovalbumin?" In: *Journal of Agricultural and Food Chemistry* 54.14 (July 2006), pp. 5166–5174.

[154] M. Smith and J. F Back. "Studies on Ovalbumin II. The Formation and Properties of S-Ovalbumin, a More Stable Form of Ovalbumin". In: *Australian Journal of Biological Sciences* 18.2 (1965), p. 365.

[155] J. W. Donovan and C. J. Mapes. "A Differential Scanning Calorimetric Study of Conversion of Ovalbumin toS-ovalbumin in Eggs". In: *Journal of the Science of Food and Agriculture* 27.2 (Feb. 1976), pp. 197–204.

[156] J. Williams et al. "The Primary Structure of Hen Ovotransferrin". In: *European Journal of Biochemistry* 122.2 (Feb. 1982), pp. 297–303.

[157] H. Kurokawa, B. Mikami, and M. Hirose. "Crystal Structure of Diferric Hen Ovotransferrin at 2.4 Å Resolution". In: *Journal of Molecular Biology* 254.2 (Nov. 1995), pp. 196–207.

[158] A. B. Mason et al. "Association of the Two Lobes of Ovotransferrin Is a Prerequisite for Receptor Recognition. Studies with Recombinant Ovotransferrins". In: *Biochemical Journal* 319.2 (Oct. 1996), pp. 361–368.

[159] E. Antonini, N. Orsi, and P. Valenti. "Effetto Delle Transferrine Sulla Patogenicita Delle Enterobacteriaceae". In: *Giornale di malattie infettive e parassitarie* 29 (1977), pp. 481–489.

[160] P. Valenti et al. "Antibacterial Activity of Matrix-Bound Ovotransferrin". In: *Antimicrobial Agents and Chemotherapy* 21.5 (May 1982), pp. 840–841.

[161] P. Valenti et al. "Studies of the Antimicrobial Activity of Ovotransferrin". In: *International Journal of Tissue Reactions* 5.1 (1983), pp. 97–105.

[162] P. Valenti et al. "Antifungal Activity of Ovotransferrin towards Genus Candida". In: *Mycopathologia* 89.3 (Mar. 1985), pp. 169–175.

[163] P. Valenti et al. “Interaction between Lactoferrin and Ovotransferrin and *Candida* Cells”. In: *FEMS Microbiology Letters* 33.2-3 (Feb. 1986), pp. 271–275.

[164] P. Visca et al. “Interaction of Lactoferrin with Escherichia Coli Cells and Correlation with Antibacterial Activity”. In: *Medical Microbiology and Immunology* 179.6 (1990), pp. 323–333.

[165] H. R. Ibrahim et al. “Identification of a Distinct Antibacterial Domain within the N-lobe of Ovotransferrin”. In: *Biochimica et Biophysica Acta (BBA) - Molecular Cell Research* 1401.3 (Mar. 1998), pp. 289–303.

[166] H. R. Ibrahim, Y. Sugimoto, and T. Aoki. “Ovotransferrin Antimicrobial Peptide (OTAP-92) Kills Bacteria through a Membrane Damage Mechanism”. In: *Biochimica et Biophysica Acta (BBA) - General Subjects* 1523.2-3 (Oct. 2000), pp. 196–205.

[167] R. Huopalahti et al., eds. *Bioactive Egg Compounds*. Berlin, Heidelberg: Springer Berlin Heidelberg, 2007.

[168] H. Yamashita et al. “Involvement of Ovotransferrin in the Thermally Induced Gelation of Egg White at around 65.DEG.C..” In: *Bioscience, Biotechnology, and Biochemistry* 62.3 (1998), pp. 593–595.

[169] J. W. Donovan et al. “A Differential Scanning Calorimetric Study of the Stability of Egg White to Heat Denaturation”. In: *Journal of the Science of Food and Agriculture* 26.1 (Jan. 1975), pp. 73–83.

[170] I. Kato et al. “Chicken Ovomucoid: Determination of Its Amino Acid Sequence, Determination of the Trypsin Reactive Site, and Preparation of All Three of Its Domains”. In: *Biochemistry* 26.1 (1987), pp. 193–201.

[171] J. Kovacs-Nolan et al. “Immunochemical and Structural Analysis of Pepsin-Digested Egg White Ovomucoid”. In: *Journal of Agricultural and Food Chemistry* 48.12 (Dec. 2000), pp. 6261–6266.

[172] J. Bernhisel-Broadbent et al. “Allergenicity and Antigenicity of Chicken Egg Ovomucoid (Gal d III) Compared with Ovalbumin (Gal d I) in Children with Egg Allergy and in Mice”. In: *The Journal of Allergy and Clinical Immunology* 93.6 (June 1994), pp. 1047–1059.

[173] A. Urisu et al. “Allergenic Activity of Heated and Ovomucoid-Depleted Egg White”. In: *The Journal of Allergy and Clinical Immunology* 100.2 (Aug. 1997), pp. 171–176.

[174] D. A. Omana, J. Wang, and J. Wu. “Ovomucin – a Glycoprotein with Promising Potential”. In: *Trends in Food Science & Technology* 21.9 (Sept. 2010), pp. 455–463.

[175] A. Eichholz. "The Hydrolysis of Proteids". In: *The Journal of Physiology* 23.3 (July 1898), pp. 163–177.

[176] C. Rabouille et al. "The Supramolecular Organization of Ovomucin. Biophysical and Morphological Studies". In: *Biochemical Journal* 266.3 (Mar. 1990), pp. 697–706.

[177] J. Brooks and H. Hale. "The Mechanical Properties of the Thick White of the Hen's Egg". In: *Biochimica et Biophysica Acta* 32 (Jan. 1959), pp. 237–250.

[178] J. Wang et al. "Ovomucin May Be the Key Protein Involved in the Early Formation of Egg-White Thermal Gel". In: *Food Chemistry* 366 (Jan. 2022), p. 130596.

[179] A. Kato et al. "Changes in Lysozyme during Egg White Thinning". In: *Agricultural and Biological Chemistry* 42.1 (Jan. 1978), pp. 175–176.

[180] A. Kato et al. "Functional and Structural Properties of Ovomucin". In: *Agricultural and Biological Chemistry* 49.12 (Dec. 1985), pp. 3501–3504.

[181] R. Nakamura and Y. Sato. "Studies on the Foaming Property of the Chicken Egg White". In: *Agricultural and Biological Chemistry* 28.8 (1964), pp. 530–534.

[182] A. Fleming. "On a Remarkable Bacteriolytic Element Found in Tissues and Secretions". In: *Proceedings of the Royal Society of London. Series B, Containing Papers of a Biological Character* 93.653 (May 1922), pp. 306–317.

[183] V. A. Proctor, F. E. Cunningham, and D. Y. C. Fung. "The Chemistry of Lysozyme and Its Use as a Food Preservative and a Pharmaceutical". In: *C R C Critical Reviews in Food Science and Nutrition* 26.4 (Jan. 1988), pp. 359–395.

[184] J. C. Bonilla and M. P. Clausen. "Super-Resolution Microscopy to Visualize and Quantify Protein Microstructural Organization in Food Materials and Its Relation to Rheology: Egg White Proteins". In: *Food Hydrocolloids* 124 (Mar. 2022), p. 107281.

[185] J. Als-Nielsen and D. McMorrow. *Elements of Modern X-ray Physics*. 1st ed. Wiley, Mar. 2011.

[186] H. Wiedemann. "Theory of Synchrotron Radiation". In: *Particle Accelerator Physics*. Cham: Springer International Publishing, 2015, pp. 857–894.

[187] A. Liénard. *Champ Électrique et Magnétique Produit Par Une Charge Électrique Concentrée En Un Point et Animée d'un Mouvement Quelconque*. G. Carré et C. Naud, 1898.

[188] E. Wiechert. "Elektrodynamische Elementargesetze". In: *Annalen der Physik* 309.4 (1901), pp. 667–689.

[189] H. Wiedemann. "Synchrotron Radiation Physics". In: *Synchrotron Light Sources and Free-Electron Lasers*. Ed. by E. J. Jaeschke et al. Cham: Springer International Publishing, 2016, pp. 3–49.

[190] K.-J. Kim. “Brightness and Coherence of Synchrotron Radiation and High-Gain Free Electron Lasers”. In: *Nuclear Instruments and Methods in Physics Research Section A: Accelerators, Spectrometers, Detectors and Associated Equipment* 261.1-2 (Nov. 1987), pp. 44–53.

[191] H. Franz et al. “Technical Report: PETRA III: DESY’s New High Brilliance Third Generation Synchrotron Radiation Source”. In: *Synchrotron Radiation News* 19.6 (Dec. 2006), pp. 25–29.

[192] U. Vainio. “Small-Angle X-Ray Scattering”. In: *X-Ray Diffraction: Modern Experimental Techniques*. Ed. by O. H. Seeck and B. M. Murphy. Singapore: Pan stanford publ, 2015, pp. 89–127.

[193] J. Teixeira. “Small-Angle Scattering by Fractal Systems”. In: *Journal of Applied Crystallography* 21.6 (Dec. 1988), pp. 781–785.

[194] E. M. Anitas. “Small-Angle Scattering from Fractals: Differentiating between Various Types of Structures”. In: *Symmetry* 12.1 (Jan. 2020), p. 65.

[195] P. Pfeifer et al. “Nearly Space-Filling Fractal Networks of Carbon Nanopores”. In: *Physical Review Letters* 88.11 (Feb. 2002), p. 115502.

[196] H. D. Bale and P. W. Schmidt. “Small-Angle X-Ray-Scattering Investigation of Submicroscopic Porosity with Fractal Properties”. In: *Physical Review Letters* 53.6 (Aug. 1984), pp. 596–599.

[197] G. Beaucage. “Approximations Leading to a Unified Exponential/Power-Law Approach to Small-Angle Scattering”. In: *Journal of Applied Crystallography* 28.6 (Dec. 1995), pp. 717–728.

[198] G. Beaucage. “Small-Angle Scattering from Polymeric Mass Fractals of Arbitrary Mass-Fractal Dimension”. In: *Journal of Applied Crystallography* 29.2 (Apr. 1996), pp. 134–146.

[199] B. Hammouda. “A New Guinier–Porod Model”. In: *Journal of Applied Crystallography* 43.4 (Aug. 2010), pp. 716–719.

[200] O. Leupold et al. *Status of the Coherence Beamline at PETRA III*. 2007.

[201] I. A. Vartanyants and A. Singer. “Coherence Properties of Third-Generation Synchrotron Sources and Free-Electron Lasers”. In: *Synchrotron Light Sources and Free-Electron Lasers*. Ed. by E. Jaeschke et al. Cham: Springer International Publishing, 2015, pp. 1–38.

[202] K. F. Ludwig. “Comment on "Speckle in the Diffraction Patterns of Hendricks-Teller and Icosahedral Glass Models"”. In: *Physical Review Letters* 61.13 (Sept. 1988), pp. 1526–1526.

[203] J. Rigden and E. Gordon. "Granularity of Scattered Optical Maser Light". In: *Proceedings of the Institute of Radio Engineers* 50.11 (1962), p. 2367.

[204] M. Sutton et al. "Observation of Speckle by Diffraction with Coherent X-rays". In: *Nature* 352.6336 (Aug. 1991), pp. 608–610.

[205] A. Siegert and M. I. o. T. R. Laboratory. *On the Fluctuations in Signals Returned by Many Independently Moving Scatterers*. Report (Massachusetts Institute of Technology. Radiation Laboratory). Radiation Laboratory, Massachusetts Institute of Technology, 1943.

[206] P. Lassègues et al. "Field and Intensity Correlations: The Siegert Relation from Stars to Quantum Emitters". In: *The European Physical Journal D* 76.12 (Dec. 2022), p. 246.

[207] M. Sutton. *Evaluation of Coherence Factor for High Q Data*. 2007.

[208] P. N. Pusey. "Statistical Properties of Scattered Radiation". In: *Photon Correlation Spectroscopy and Velocimetry*. Ed. by H. Z. Cummins and E. R. Pike. Boston, MA: Springer US, 1977, pp. 45–141.

[209] G. Williams and D. C. Watts. "Non-Symmetrical Dielectric Relaxation Behaviour Arising from a Simple Empirical Decay Function". In: *Transactions of the Faraday Society* 66 (1970), p. 80.

[210] M. Sutton et al. "Using Coherence to Measure Two-Time Correlation Functions". In: *Optics Express* 11.19 (Sept. 2003), pp. 2268–2277.

[211] O. Bikondoa. "On the Use of Two-Time Correlation Functions for X-ray Photon Correlation Spectroscopy Data Analysis". In: *Journal of Applied Crystallography* 50.2 (Apr. 2017), pp. 357–368.

[212] D. S. Lemons and A. Gythiel. "Paul Langevin's 1908 Paper "On the Theory of Brownian Motion" ["Sur La Théorie Du Mouvement Brownien," C. R. Acad. Sci. (Paris) **146** , 530–533 (1908)]". In: *American Journal of Physics* 65.11 (Nov. 1997), pp. 1079–1081.

[213] A. Einstein. "Über die von der molekularkinetischen Theorie der Wärme geforderte Bewegung von in ruhenden Flüssigkeiten suspendierten Teilchen". In: *Annalen der Physik* 322.8 (1905), pp. 549–560.

[214] F. Lehmkühler et al. "Emergence of Anomalous Dynamics in Soft Matter Probed at the European XFEL". In: *Proceedings of the National Academy of Sciences* 117.39 (Sept. 2020), pp. 24110–24116.

[215] L. Cipelletti et al. "Universal Aging Features in the Restructuring of Fractal Colloidal Gels". In: *Physical Review Letters* 84.10 (Mar. 2000), pp. 2275–2278.

[216] L. Cipelletti et al. "Universal Non-Diffusive Slow Dynamics in Aging Soft Matter". In: *Faraday Discussions* 123 (Jan. 2003), pp. 237–251.

[217] L. Ramos and L. Cipelletti. "Ultraslow Dynamics and Stress Relaxation in the Aging of a Soft Glassy System". In: *Physical Review Letters* 87.24 (Nov. 2001), p. 245503.

[218] R. Bandyopadhyay et al. "Evolution of Particle-Scale Dynamics in an Aging Clay Suspension". In: *Physical Review Letters* 93.22 (Nov. 2004), p. 228302.

[219] B. Chung et al. "Microscopic Dynamics of Recovery in Sheared Depletion Gels". In: *Physical Review Letters* 96.22 (June 2006), p. 228301.

[220] A. Robert et al. "Glassy Dynamics and Aging in a Dense Ferrofluid". In: *Europhysics Letters (EPL)* 75.5 (Sept. 2006), pp. 764–770.

[221] R. Bandyopadhyay et al. "Slow Dynamics, Aging, and Glassy Rheology in Soft and Living Matter". In: *Solid State Communications* 139.11-12 (Sept. 2006), pp. 589–598.

[222] A. Fluerasu et al. "Slow Dynamics and Aging in Colloidal Gels Studied by X-Ray Photon Correlation Spectroscopy". In: *Physical Review E* 76.1 (July 2007), p. 010401.

[223] V. M. Giordano and B. Ruta. "Unveiling the Structural Arrangements Responsible for the Atomic Dynamics in Metallic Glasses during Physical Aging". In: *Nature Communications* 7.1 (Jan. 2016), p. 10344.

[224] J.-P. Bouchaud and E. Pitard. "Anomalous Dynamical Light Scattering in Soft Glassy Gels". In: *The European Physical Journal E* 6.3 (Nov. 2001), pp. 231–236.

[225] J.-P. Bouchaud and A. Georges. "Anomalous Diffusion in Disordered Media: Statistical Mechanisms, Models and Physical Applications". In: *Physics Reports* 195.4-5 (Nov. 1990), pp. 127–293.

[226] E. W. Montroll and G. H. Weiss. "Random Walks on Lattices. II". In: *Journal of Mathematical Physics* 6.2 (Feb. 1965), pp. 167–181.

[227] R. Metzler and J. Klafter. "The Random Walk's Guide to Anomalous Diffusion: A Fractional Dynamics Approach". In: *Physics Reports* 339.1 (Dec. 2000), pp. 1–77.

[228] C. Caronna et al. "Dynamics of Nanoparticles in a Supercooled Liquid". In: *Physical Review Letters* 100.5 (Feb. 2008), p. 055702.

[229] B. J. Berne and R. Pecora. *Dynamic Light Scattering: With Applications to Chemistry, Biology, and Physics*. New York: Wiley, 1976.

[230] A. Sethi. "X-Rays: Interaction with Matter". In: *Encyclopedia of Medical Devices and Instrumentation*. Ed. by J. G. Webster. Hoboken, NJ, USA: John Wiley & Sons, Inc., Apr. 2006, emd263.

[231] R. Santra and L. Young. "Interaction of Intense X-Ray Beams with Atoms". In: *Synchrotron Light Sources and Free-Electron Lasers*. Ed. by E. J. Jaeschke et al. Cham: Springer International Publishing, 2016, pp. 1233–1260.

[232] J. H. Hubbell. *Photon Cross Sections, Attenuation Coefficients, and Energy Absorption Coefficients from 10 keV to 100 GeV*. Tech. rep. NBS NSRDS 29. Gaithersburg, MD: National Bureau of Standards, 1969, NBS NSRDS 29.

[233] A. H. Compton. "A Quantum Theory of the Scattering of X-rays by Light Elements". In: *Physical Review* 21.5 (May 1923), pp. 483–502.

[234] A. Beer. *Grundriß Des Photometrischen Calcüles.-Braunschweig, Friedrich Vieweg u. Sohn 1854*. Vieweg, 1854.

[235] P. Bouguer. *Essai d'optique Sur La Gradation de La Lumière*. Claude Jombert, 1729.

[236] S. Seltzer. *XCOM-Photon Cross Sections Database, NIST Standard Reference Database 8*. 1987.

[237] S. P. Meisburger et al. "Breaking the Radiation Damage Limit with Cryo-SAXS". In: *Biophysical Journal* 104.1 (Jan. 2013), pp. 227–236.

[238] B. C. Garrett et al. "Role of Water in Electron-Initiated Processes and Radical Chemistry: Issues and Scientific Advances". In: *Chemical Reviews* 105.1 (Jan. 2005), pp. 355–390.

[239] J. L. Magee. "Theory of Radiation Chemistry. I. Some Effects of Variation in Ionization Density [1,2]". In: *Journal of the American Chemical Society* 73.7 (July 1951), pp. 3270–3275.

[240] A. H. Samuel and J. L. Magee. "Theory of Radiation Chemistry. II. Track Effects in Radiolysis of Water". In: *The Journal of Chemical Physics* 21.6 (June 1953), pp. 1080–1087.

[241] A. Mozumder and J. L. Magee. "Theory of Radiation Chemistry. VII. Structure and Reactions in Low LET Tracks". In: *The Journal of Chemical Physics* 45.9 (Nov. 1966), pp. 3332–3341.

[242] A. Mozumder and J. L. Magee. "Model of Tracks of Ionizing Radiations for Radical Reaction Mechanisms". In: *Radiation Research* 28.2 (June 1966), p. 203. JSTOR: 3572190.

[243] H. Bethe. "Zur Theorie des Durchgangs schneller Korpuskularstrahlen durch Materie". In: *Annalen der Physik* 397.3 (1930), pp. 325–400.

[244] F. Bloch. "Zur Bremsung rasch bewegter Teilchen beim Durchgang durch Materie". In: *Annalen der Physik* 408.3 (1933), pp. 285–320.

[245] M. Inokuti. "Inelastic Collisions of Fast Charged Particles with Atoms and Molecules—The Bethe Theory Revisited". In: *Reviews of Modern Physics* 43.3 (July 1971), pp. 297–347.

[246] R. Watanabe and K. Saito. "Monte Carlo Simulation of Water Radiolysis in Oxygenated Condition for Monoenergetic Electrons from 100eV to 1MeV". In: *Radiation Physics and Chemistry* 62.2-3 (Sept. 2001), pp. 217–228.

[247] H. Yamaguchi et al. “Estimation of Yields of OH Radicals in Water Irradiated by Ionizing Radiation”. In: *Journal of Radiation Research* 46.3 (2005), pp. 333–341.

[248] S. Le Caër. “Water Radiolysis: Influence of Oxide Surfaces on H2 Production under Ionizing Radiation”. In: *Water* 3.1 (Feb. 2011), pp. 235–253.

[249] V. Gold, ed. *The IUPAC Compendium of Chemical Terminology: The Gold Book*. 4th ed. Research Triangle Park, NC: International Union of Pure and Applied Chemistry (IUPAC), 2019.

[250] A. O. Allen. “Radiation Chemistry of Aqueous Solutions”. In: *The Journal of Physical and Colloid Chemistry* 52.3 (Mar. 1948), pp. 479–490.

[251] A. O. Allen et al. “Decomposition of Water and Aqueous Solutions under Mixed Fast Neutron and γ-Radiation”. In: *The Journal of Physical Chemistry* 56.5 (May 1952), pp. 575–586.

[252] S. Kuwamoto, S. Akiyama, and T. Fujisawa. “Radiation Damage to a Protein Solution, Detected by Synchrotron X-ray Small-Angle Scattering: Dose-Related Considerations and Suppression by Cryoprotectants”. In: *Journal of Synchrotron Radiation* 11.6 (Nov. 2004), pp. 462–468.

[253] W. M. Garrison. “Reaction Mechanisms in the Radiolysis of Peptides, Polypeptides, and Proteins”. In: *Chemical Reviews* 87.2 (Apr. 1987), pp. 381–398.

[254] K. Radomska and M. Wolszczak. “Spontaneous and Ionizing Radiation-Induced Aggregation of Human Serum Albumin: Dityrosine as a Fluorescent Probe”. In: *International Journal of Molecular Sciences* 23.15 (July 2022), p. 8090.

[255] Y. M. Narode et al. “Gold Nanoparticle as a Lewis Catalyst for Water Elimination of Tyrosine-$^{\bullet}$OH Adducts: A Radiation and Quantum Chemical Study”. In: *The Journal of Physical Chemistry B* 124.17 (Apr. 2020), pp. 3591–3601.

[256] S. Garcia-Castineiras, J. Dillon, and A. Spector. “Detection of Bityrosine in Cataractous Human Lens Protein”. In: *Science* 199.4331 (Feb. 1978), pp. 897–899.

[257] R. F. Fischetti et al. “High-Resolution Wide-Angle X-ray Scattering of Protein Solutions: Effect of Beam Dose on Protein Integrity”. In: *Journal of Synchrotron Radiation* 10.5 (Sept. 2003), pp. 398–404.

[258] *P10 Coherence Beamline User Guide*. June 2016.

[259] K. Balewski et al. “PETRA III: A Low Emittance Synchrotron Radiation Source (Technical Design Report)”. In: 2004.

[260] M. Osterhoff et al. "STXM Analysis: Preparing to Go Live @ 750 Hz". In: *PROCEEDINGS OF THE 13TH INTERNATIONAL CONFERENCE ON SYNCHROTRON RADIATION INSTRUMENTATION – SRI2018*. Taipei, Taiwan, 2019, p. 060075.

[261] S. Timmermann et al. "X-Ray Driven and Intrinsic Dynamics in Protein Gels". In: *Scientific Reports* 13.1 (July 2023), p. 11048.

[262] A. F. Craievich. "Small-Angle X-ray Scattering by Nanostructured Materials". In: *Handbook of Sol-Gel Science and Technology*. Ed. by L. Klein, M. Aparicio, and A. Jitianu. Cham: Springer International Publishing, 2016, pp. 1–46.

[263] G. Weber. *X-Ray Attenuation & Absorption Calculator*.

[264] M. Hammershøj et al. "Storage of Shell Eggs Influences the Albumen Gelling Properties". In: *LWT - Food Science and Technology* 35.1 (Feb. 2002), pp. 62–69.

[265] X. Liu et al. "Underlying Mechanism for the Differences in Heat-Induced Gel Properties between Thick Egg Whites and Thin Egg Whites: Gel Properties, Structure and Quantitative Proteome Analysis". In: *Food Hydrocolloids* 106 (Sept. 2020), p. 105873.

[266] M. Weijers et al. "Heat-Induced Denaturation and Aggregation of Ovalbumin at Neutral pH Described by Irreversible First-Order Kinetics". In: *Protein Science* 12.12 (Dec. 2003), pp. 2693–2703.

[267] P. Falus, L. B. Lurio, and S. G. J. Mochrie. "Optimizing the Signal-to-Noise Ratio for X-ray Photon Correlation Spectroscopy". In: *Journal of Synchrotron Radiation* 13.3 (Apr. 2006), pp. 253–259.

[268] D. Ltd. *EIGER X 4M Technical Specifications*. 2019.

[269] A. Jain et al. "Anisotropic and Heterogeneous Dynamics in an Aging Colloidal Gel". In: *Soft Matter* 16.11 (2020), pp. 2864–2872.

[270] K. Suman and N. J. Wagner. "Anomalous Rheological Aging of a Model Thermoreversible Colloidal Gel Following a Thermal Quench". In: *The Journal of Chemical Physics* 157.2 (July 2022), p. 024901.

[271] M. D. Wilkinson et al. "The FAIR Guiding Principles for Scientific Data Management and Stewardship". In: *Scientific Data* 3.1 (Mar. 2016), p. 160018.

[272] T. Zinn et al. "Ultra-Small-Angle X-ray Photon Correlation Spectroscopy Using the Eiger Detector". In: *Journal of Synchrotron Radiation* 25.6 (Nov. 2018), pp. 1753–1759.

[273] M. Reiser and R. Rosca. *Xana - Analysis Software for X-ray Photon Correlation Spectroscopy Data*. Apr. 2022.

[274] J. Verwohlt et al. “Low Dose X-Ray Speckle Visibility Spectroscopy Reveals Nanoscale Dynamics in Radiation Sensitive Ionic Liquids”. In: *Physical Review Letters* 120.16 (Apr. 2018), p. 168001.

[275] G. Ashiotis et al. “The Fast Azimuthal Integration Python Library: *pyFAI*”. In: *Journal of Applied Crystallography* 48.2 (Apr. 2015), pp. 510–519.

[276] S. O. Hruszkewycz et al. “High Contrast X-ray Speckle from Atomic-Scale Order in Liquids and Glasses”. In: *Physical Review Letters* 109.18 (Nov. 2012), p. 185502.

[277] M. Bée. *Quasielastic Neutron Scattering: Principles and Applications in Solid State Chemistry, Biology, and Materials Science*. Bristol, England ; Philadelphia: Adam Hilger, 1988.

[278] M. Reiser. “A Nanorheology Study on the Viscoelastic Properties of Photorheological Liquids by X-Ray Photon Correlation Spectroscopy”. PhD thesis. Universität Siegen, 2020.

[279] M. Könnecke et al. “The NeXus Data Format”. In: *Journal of Applied Crystallography* 48.1 (Feb. 2015), pp. 301–305.

[280] P. Klosowski et al. “NeXus: A Common Format for the Exchange of Neutron and Synchroton Data”. In: *Physica B: Condensed Matter* 241–243 (Dec. 1997), pp. 151–153.

[281] M. Könnecke. “The State of the NeXus Data Format”. In: *Physica B: Condensed Matter* 385–386 (Nov. 2006), pp. 1343–1345.

[282] The HDF Group. *Hierarchical Data Format, Version 5*. 1997.

[283] N. Carboni. “PaNOSC – Making FAIR Open Data a Reality for Photon and Neutron Science”. In: *The Project Repository Journal* 15.1 (Nov. 2022), pp. 62–65.

[284] D. Johansen, J. Trewhella, and D. P. Goldenberg. “Fractal Dimension of an Intrinsically Disordered Protein: Small-angle X-ray Scattering and Computational Study of the Bacteriophage λ N Protein”. In: *Protein Science* 20.12 (Dec. 2011), pp. 1955–1970.

[285] T. G. Dewey. *Fractals in Molecular Biophysics*. Topics in Physical Chemistry. Oxford ; New York: Oxford University Press, 1997.

[286] L. G. B. Bremer, T. Van Vliet, and P. Walstra. “Theoretical and Experimental Study of the Fractal Nature of the Structure of Casein Gels”. In: *Journal of the Chemical Society, Faraday Transactions 1: Physical Chemistry in Condensed Phases* 85.10 (1989), p. 3359.

[287] L. G. Bremer et al. “On the Fractal Nature of the Structure of Acid Casein Gels”. In: *Colloids and Surfaces* 51 (Jan. 1990), pp. 159–170.

[288] T. Hagiwara, H. Kumagai, and K. Nakamura. “Fractal Analysis of Aggregates in Heat-Induced BSA Gels”. In: *Food Hydrocolloids* 12.1 (Jan. 1998), pp. 29–36.

[289] T. Hagiwara, H. Kumagai, and T. Matsunaga. “Fractal Analysis of the Elasticity of BSA and β-Lactoglobulin Gels”. In: *Journal of Agricultural and Food Chemistry* 45.10 (Oct. 1997), pp. 3807–3812.

[290] S. Ikeda, E. A. Foegeding, and T. Hagiwara. “Rheological Study on the Fractal Nature of the Protein Gel Structure”. In: *Langmuir* 15.25 (Dec. 1999), pp. 8584–8589.

[291] A. Marangoni. “On the Structure of Particulate Gels—the Case of Salt-Induced Cold Gelation of Heat-Denatured Whey Protein Isolate”. In: *Food Hydrocolloids* 14.1 (Jan. 2000), pp. 61–74.

[292] R. Vreeker et al. “Fractal Aggregation of Whey Proteins”. In: *Food Hydrocolloids* 6.5 (Nov. 1992), pp. 423–435.

[293] M. Verheul et al. “Power Law Behavior of Structural Properties of Protein Gels”. In: *Langmuir* 14.9 (Apr. 1998), pp. 2263–2268.

[294] J. R. Hörandel. “On the Knee in the Energy Spectrum of Cosmic Rays”. In: *Astroparticle Physics* 19.2 (May 2003), pp. 193–220.

[295] M. S. Akhundzadeh. “X-Ray Photon Correlation Spectroscopy Experiments of Protein Dynamics at Molecular Length Scales - Potentials and Limitations.” PhD thesis. Siegen: Universität Siegen, 2023.

[296] A. Girelli. “Dynamics of Antibodies in Solution: From Individual Proteins to Phase Separation Domains”. In: (Sept. 2024).

[297] M. Bin et al. “Coherent X-ray Scattering Reveals Nanoscale Fluctuations in Hydrated Proteins”. In: *The Journal of Physical Chemistry B* 127.21 (June 2023), pp. 4922–4930.

[298] A. Grishaev. “Sample Preparation, Data Collection, and Preliminary Data Analysis in Biomolecular Solution X-Ray Scattering”. In: *Current Protocols in Protein Science* 70.1 (Nov. 2012).

[299] D. A. Jacques and J. Trewhella. “Small-Angle Scattering for Structural Biology-Expanding the Frontier While Avoiding the Pitfalls: Small-Angle Scattering for Structural Biology”. In: *Protein Science* 19.4 (Apr. 2010), pp. 642–657.

[300] M. Ueno, I. Nakanishi, and K.-i. Matsumoto. “Method for Assessing X-ray-induced Hydroxyl Radical-Scavenging Activity of Biological Compounds/Materials”. In: *Journal of Clinical Biochemistry and Nutrition* (2013), pp. 95–100.

[301] J. Möller et al. “Using Low Dose X-Ray Speckle Visibility Spectroscopy to Study Dynamics of Soft Matter Samples”. In: *New Journal of Physics* 23.9 (Sept. 2021), p. 093041.

[302] N. Kirby et al. “Improved Radiation Dose Efficiency in Solution SAXS Using a Sheath Flow Sample Environment”. In: *Acta Crystallographica Section D Structural Biology* 72.12 (Dec. 2016), pp. 1254–1266.

[303] G. Ueno et al. “Low-Dose X-ray Structure Analysis of Cytochrome *c* Oxidase Utilizing High-Energy X-rays”. In: *Journal of Synchrotron Radiation* 26.4 (July 2019), pp. 912–921.

[304] A. Fluerasu et al. “X-Ray Photon Correlation Spectroscopy under Flow”. In: *Journal of Synchrotron Radiation* 15.4 (July 2008), pp. 378–384.

[305] F. Westermeier et al. “Structure and Short-Time Dynamics in Concentrated Suspensions of Charged Colloids”. In: *The Journal of Chemical Physics* 137.11 (Sept. 2012), p. 114504.

[306] L. B. Lurio et al. “Use of Continuous Sample Translation to Reduce Radiation Damage for XPCS Studies of Protein Diffusion”. In: *Journal of Synchrotron Radiation* 28.2 (Mar. 2021), pp. 490–498.

List of Own Publications

- **Automated matching of two-time X-ray photon correlation maps from phase-separating proteins with Cahn–Hilliard-type simulations using auto-encoder networks**
  S. Timmermann, V. Starostin, A. Girelli, A. Ragulskaya, H. Rahmann, M. Reiser, N. Begam, L. Randolph, M. Sprung, F. Westermeier, F. Zhang, F. Schreiber and C. Gutt
  Journal of Applied Crystallography, **55**, 751-757 (2022)

- **Resolving molecular diffusion and aggregation of antibody proteins with mega-hertz X-ray free-electron laser pulses**
  M. Reiser, A. Girelli, A. Ragulskaya, S. Das, S. Berkowicz, M. Bin, M. Ladd Parada, M. Filianina, H. Poggemann, N. Begam, M. S. Akhundzadeh, S. Timmermann, L. Randolph, Y. Chushkin, T. Seydel, U. Bösenberg, J. Hallmann, J. Möller, A. Rodriguez-Fernandez, R. Rosca, R. Schaffer, M. Scholz, R. Shayduk, A. Zozulya, A. Madsen, F. Schreiber, F. Zhang, F. Perakis and C. Gutt
  Nature Communications, **13**, 5528 (2022)

- **Effects of temperature and ionic strength on the microscopic structure and dynamics of egg white gels**
  N. Begam, S. Timmermann, A. Ragulskaya, A. Girelli, M. D. Senft, S. Retzbach, N. D. Anthuparambil, M. S. Akhundzadeh, M. Kowalski, F. Westermeier, M. Sprung, F. Zhang, C. Gutt and F. Schreiber
  The Journal of Chemical Physics, **158**, 074903 (2023)

- **X-ray driven and intrinsic dynamics in protein gels**
  S. Timmermann, N. D. Anthuparambil, A. Girelli, N. Begam, M. Kowalski,, S. Retzbach, M. D. Senft, M. S. Akhundzadeh, H. Poggemann, M. Moron, A. Hiremath, D. Gutmüller, M. Dargasz, Ö. Öztürk, M. Paulus, F. Westermeier, M. Sprung, A. Ragulskaya F. Zhang, F. Schreiber and C. Gutt
  Scientific Reports, **13**, 11048 (2023)

- **Coherent X-ray Scattering Reveals Nanoscale Fluctuations in Hydrated Proteins**
  M. Bin, M. Reiser, M.Filianina, S. Berkowicz, S. Das, S. Timmermann, W. Roseker, R. Bauer, J. Öström, A. Karina, K. Amann-Winkel, M. Ladd-Parada, F. Westermeier, M.Sprung, J. Möller, F. Lehmkühler, C. Gutt and F. Perakis
  The Journal of Physical Chemistry B, **127**, 4922-4930 (2023)

- **Nanocrystallites Modulate Intermolecular Interactions in Cryoprotected Protein Solutions**
  M. Filianina, M. Bin, S. Berkowicz, M. Reiser, H. Li, S. Timmermann, M. Blankenburg, K. Amann-Winkel, C. Gutt and F. Perakis
  The Journal of Physical Chemistry B, **127**, 6197-6204 (2023)

- **Exploring non-equilibrium processes and spatio-temporal scaling laws in heated egg yolk using coherent X-rays**
  N. D. Anthuparambil, A. Girelli, S. Timmermann, M. Kowalski, M. S. Akhundzadeh, S. Retzbach, M. D. Senft, M. Dargasz, D. Gutmüller, A. Hiremath, M. Moron, Ö. Özgül, H. Poggemann, A. Ragulskaya, N. Begam, A. Tosson, M. Paulus, F. Westermeier, F. Zhang, M. Sprung, F. Schreiber and C. Gutt
  Nature Communications, **14**, 5580 (2023)

Acknowledgments

First of all, I want to thank my supervisor **Prof. Dr. Christian Gutt**:

Thank you for allowing me to participate in this exciting research. Thank you for being so supportive during the time we have been figuring out together where this thesis is going. You made all these trips to beamtimes possible, which will remain wonderful memories. The last four years under your supervision made me more confident, not only about my research but also about myself.

Second, I want to thank my second reviewer **Prof. Dr. Foivos Perakis**:

Thank you for taking the time to read and evaluate this thesis. Thank you for inviting me to your beamtimes and giving me the opportunity to meet new people when everything else was shut down.

This project would not have been successful without **Dr. Nimmi Das Anthuparambil**:

Thank you for patiently explaining everything in the preparation lab to me. You were the best company on the path to making the XPCS code work.

Furthermore, I want to thank **Prof. Dr. Dr. hc Frank Schreiber, PD Dr. Fajun Zhang, Dr. Anastasia Ragulskaya** and **Dr. Nafisa Begam**:

Thank you for giving me the opportunity to present my research to a larger audience for the first time and for all the discussions on the data analysis and interpretation.

Special thanks to all the people who supported me during the beam times at P10:

You made those weeks the most enjoyable of my PhD time. Without you, it wouldn't have been that productive and that much fun at the same time. Especially the Rüdigers **Max Senft, Marvin Kowalski, Sebastian Retzbach** and **Michelle Dargasz**: Thank you for the best script names and our unique night shift pizza creation.

To the XPCS group at Stockholm University:

Thank you for the opportunity to join your beamtimes and the wonderful research stay in Stockholm. Special thanks to **Dr. Anita Girelli**, whose enthusiasm for science is infectious, to **Dr. Mariia Filianina**, who showed me the beauty of night shifts, and to **Maddalena Bin**, who helped me to solve every problem in Python (including side quests).

I have to thank **Dr. Marc Moron** and **Dr. Mario Reiser** for their support with the XPCS analysis code.

Thanks to **Dr. Michael Sprung** and the team of the P10 coherence applications beamline: Special thanks to **Dr. Fabian Westermeier** for the detailed explanations on the beamline operation, the careful reading of the manuscripts, and your kindness, even when we had to call you in the middle of the night.

Danke an meine beiden ehemaligen Bürokollegen:

Besonderen Dank an **Dr. Lisa Randolph**, dafür dass du mich in die Arbeitsgruppe geholt hast und vor allem für die aufbauenden Nachrichten, besondern im letzten halben Jahr. Ohne **Dr. Hendrik Rahmann** hätte ich wohl öfter zu viel Zeit am Schreibtisch und zu wenig Zeit mit Sport verbracht.

An meine Studienkollegen und Freunde **Dina Wilks**, **Clémentine Lovato** und **Florian Sledz**: Danke für die Kaffeepausen, Spaziergänge, Dopppelkopfrunden und Diskussionen abseits der Forschung ohne die die Zeit in Siegen nicht halb so viel Spaß gemacht hätte.

An **Max**:

Danke, dass ich an deinem Schreibtisch den Großteil dieser Arbeit schreiben durfte und dass du mich danach abends wieder aufgebaut hast. Danke für deine ganze Unterstützung. Des bedarfs!

Der größte Dank geht an meine Familie:

An **meine Eltern**: Danke, dass ihr mich bei jedem meiner Vorhaben unterstützt und ich immer mit allem zu euch kommen kann. Danke an **Eric** und **Lisa**, die oft auf mich verzichten mussten, wenn ich mal wieder in Hamburg war. Danke an meinen größten Fan, **Opa Heinrich**. Bald ist es soweit, dann kannst du allen erzählen, dass deine Enkelin jetzt Doktor ist.